

**HELICAL FLOW OF POLYMER MELTS IN EXTRUDERS:
MODEL DEVELOPMENT AND VALIDATION WITH EXPERIMENTS**

by

FARSHID SANJABI

B.Sc., Amirkabir University, Tehran, Iran 1994

M.A.Sc., Amirkabir University, Tehran, Iran 1996

M.A.Sc., Ryerson University, Toronto, Ontario, Canada 2004

A Dissertation
presented to Ryerson University
in partial fulfillment of the
requirements for the degree of

DOCTOR OF PHILOSOPHY

**in the Program of
CHEMICAL ENGINEERING**

Toronto, Ontario, Canada, 2010

© (Farshid Sanjabi) 2010

Author's Declaration

I hereby declare that I am the sole author of this dissertation.

I authorize Ryerson University to lend this thesis to other institutions or individuals for the purpose of scholarly research.

Farshid Sanjabi

I further authorize Ryerson University to reproduce this thesis by photocopying or by other means, in total or in part, at the request of other institutions or individuals for the purpose of scholarly research.

Farshid Sanjabi

Abstract

Operating and processing conditions as well as the selection of the screw design in injection molding industry are largely based on trial-and-error exercise, which is expensive and time consuming. A better approach is to develop mathematical models for prediction of the final process performance where the conditions and parameters of a process can be used as inputs in those models. However, most of the models developed and used so far contain unrealistic geometrical and mathematical simplifications. The objective of this work is to develop a steady-state three dimensional mathematical model to describe the flow of an incompressible polymer melt inside a helical geometry, which represents the polymer's true motion in extrusion and injection molding processes. In order to develop the model in helical geometry, where at least two axes are not perpendicular, the mathematical model is first developed in a natural system (i.e. cylindrical) and using transformation tools are then changed to the physical helical one. In this initiative, we develop an iterative computational algorithm based on shooting Newton-Raphson method in order to simulate the process. The transformation matrices to adapt the equations of change from a natural system (i.e. orthogonal cylindrical systems) to a physical system (i.e. helical coordinates) are also developed for velocity and derivative profiles. Subsequently the solution approach to solve the indirectly coupled equations of change is explained and the simulation results are compared with experimental data. The simulation results are validated against data obtained from ten different experiments with an industrial injection molding machine, processing two different polymers — high density polyethylene (HDPE) and poly ethylene terephthalate

(PET). It is observed that the simulation results are in good agreement with experimental data. This outcome demonstrates the utility of the developed mathematical model and simulation approach. Important features of this work are the consideration of the linear backward motion of the screw leading to calculation of proper process shot size and the incorporation of the tapering screw designs with upward and downward sections in the direction of the flow into the model. Another important feature in the development of the mathematical model is that the rheological and physical properties of plastic resins are not constant and change as the melt temperature changes during the process. From the standpoint of industrial practice, the direct benefit of this work is the ability to effectively calculate adequate shot size, recovery rate, and various state variables throughout the extent of the machine.

Acknowledgments

I am grateful to several people at the Department of Chemical Engineering who gave me guidance and inspiration and support. I wish to express sincere appreciation to Professors Dr. Simant R. Upreti, Dr. Ali Lohi, and Dr. Farhad Ein-Mozaffari for their compassionate supervision and guidance throughout the completion of this thesis and the preparation of this manuscript.

In addition, special thanks are due to Dr. Simant Upreti, my supervisor, mentor, and role model for his sound advice, inspiration, and continuous support in all matters throughout my graduate studies. I have learned from him far beyond the textbooks. He provided me unflinching encouragement and support in various ways. I am indebted to him more than he knows.

I am thankful to Husky Injection Molding Systems Inc. for their invaluable financial and technical support throughout the program.

Table of Content

Abstract.....	iii
Acknowledgments	v
List of Tables	x
List of Figures.....	xi
List of Appendices.....	xv
<i>Chapter 1</i>	1
INTRODUCTION	1
1.1 Injection Molding Process.....	3
1.2 Development of Helical Coordinates.....	8
1.2.1 Application of Helical Geometry	10
1.2.2 Transformer for velocity profiles.....	13
1.2.3 Transformer for derivatives	14
1.3 Geometries used in extrusion models	14
1.4 Literature Survey.....	14
<i>Chapter 2</i>	17
EXPERIMENTAL SETUP	17
2.1 Drying of PET Resin.....	19
2.2 Extruder Instrumentation.....	22
2.3 Design of Experiment.....	24
<i>Chapter 3</i>	27
MATHEMATICAL MODELING AND SIMULATION	27
3.1 Momentum Balance- θ Direction; Helical	28

3.2 Momentum Balance-Z Direction-Helical	30
3.3 Momentum Balance-radial Direction-Helical.....	31
3.4 Equation of Continuity	33
3.5 Assumptions	34
3.6 Shear Rates	35
3.7 Shear Stress	36
3.7.1 Shear stress components in cylindrical coordinates:	37
3.7.2 Shear stress components in helical coordinates:.....	38
3.8 Viscosity Models.....	38
3.9 Flow Rate	44
3.10 Energy Balance-Helical.....	45
3.11 Initial and Boundary Conditions	59
3.12 Solution Approach.....	60
3.12.1 Derivation of $\frac{\partial V_{\theta}}{\partial p}$:	63
3.12.2 Derivation of $\frac{\partial V_z}{\partial p}$:	64
3.13 Simulation Details	64
3.13.1 Grid Sizes	64
3.13.2 Calculation of Proper Shot Size.....	65
3.13.3 'Screw Details':	66
3.14 Input Data Required for the Simulation.....	69
3.14.1 Pressure and Temperature.....	69
Chapter 4	71
RESULTS.....	71
4.1 Melt Temperature at the Screw Tip	71
4.1.1 Runs 1 to 4: HDPE Melt Simulation with General Purpose Screw.....	72

4.1.2	<i>Runs 5 to 8: HDPE Melt Simulation with Barrier Screw</i>	75
4.1.3	<i>Runs 9 to 10: PET Melt Simulation with PET Screw</i>	79
4.2	Melt Pressure During Recovery	81
4.2.1	<i>Runs 1 to 4: HDPE Melt Pressure Simulation with GP Screw</i>	82
4.2.2	<i>Runs 5 to 8: HDPE Melt Pressure Simulation with Barrier Screw</i>	84
4.2.3	<i>Runs 9 to 10: PET Melt Pressure Simulation with PET Screw</i>	87
4.3	Recovery Rate	88
4.4	The Screw “L/D”	89
4.5	Viscosity	90
4.6	Torque	98
4.7	Power	101
4.8	Sensitivity Analysis: Grid size change in the helical coordinate	102
<i>Chapter 5</i>		111
DISCUSSION		111
5.1	Sensitivity Analysis: Changes in thermo-physical properties	111
5.1.1	<i>Variations of Thermal Conductivity</i>	112
5.1.2	<i>Changes in the heat capacity</i>	117
5.2	A Case Study for Validation of Torque and Power	122
5.3	Simulation Results	127
5.4	Viscosity Models	133
5.5	Dependency of Viscosity on Zero Shear Rate	134
5.6	Total Shear Rate	135
<i>Chapter 6</i>		136
CONCLUSIONS		136
<i>Chapter 7</i>		138

FUTURE WORK	138
NOMENCLATURE	140
REFERENCES	142
Appendix A	148
Appendix B	152

List of Tables

Table 1: A comparison between the helical based simulation tool developed in this work and non-helical based simulation packages. Results are compared with experimental data	8
Table 2: Comparison of selected transformers developed by various researchers.....	16
Table 3: Physical and Rheological properties of solid HDPE and PET grades provided by the resin suppliers and used in the experiments	18
Table 4: Benefit of using Design of Experiment	25
Table 5: Design of Experiment prepared for the validation of screw prediction tool results..	26
Table 6: Required screw processing parameters for the experimental tests.....	70
Table 7: Simulated versus measured melt temperature for Runs 1 to 10 (see Table 5 for reference) at the screw tip	72
Table 8: Simulated versus measured melt pressure (see Table 5) during recovery for Runs 1 to 10.....	82
Table 9: Simulated versus measured recovery rate (see Table 5) for Runs 1 to 10.....	88
Table 10: Simulated L/D for Runs 1 to 10	89
Table 11: Simulated viscosity values for Runs 1 to 10. The resin in Runs 1-8 is HDPE, while in Runs 9-10 PET resin has been used	90
Table 12: Viscosity data for PET resin used in Runs 9 and 10. Shear rates are measured using Gottfert Rheograph 2003 Capillary Rheometer based on ASTM D3835.....	98
Table 13: Simulated versus measured screw torque for Runs 1 to 10.....	100
Table 14: Simulated screw power consumption for Runs 1 to 10.....	101
Table 15: Number of grid points used in the sensitivity analysis	104
Table 16: Processing parameters for the screw torque and power experimental tests	123
Table 17: Design of Experiment for validation of screw torque and power results	123
Table 18: Screw torque and power simulation versus experimental results	124

List of Figures

Figure 1: A schematic of a single screw Husky IMS injection machine	3
Figure 2: A schematic of the region around two flights of a screw	5
Figure 3: A schematic of a single extruder screw.....	7
Figure 4: Helical geometry inside a single screw extruder	10
Figure 5: Helical access coordinates: Normal (e_r), Tangential (e_θ), and Helical (e_z).....	11
Figure 6: Transformer matrix for velocity profiles.....	12
Figure 7: Schematic of the 400 ton injection molding system used for validation of the simulation results. Different components of the system are shown on the unit.....	19
Figure 8: IV drop in the melt phase with respect to resin moisture content after drying process.....	20
Figure 9: The Piovan resin dryer (3500 Liter DP628L) utilized for the validation test.....	21
Figure 10: Location of melt pressure and temperature sensors at the injection unit.....	22
Figure 11: Shear thinning behavior of polymer melts.....	35
Figure 12: Velocity and shear rate profiles for flow in a tube	36
Figure 13: Schematic diagram of shear rate and shear stress surfaces.....	37
Figure 14: Influence of temperature on viscosity of polypropylene (Source: BP Solvay).....	40
Figure 15: The physical model of the heating process.....	46
Figure 16: Solution algorithm flow chart	61
Figure 17: Linear motion of the screw. The simulation tool allows for a detailed investigation of melt bulk temperature at different points during melting process	66
Figure 18: Characterization of the screw geometry inside the simulation input database (numerical units in mm).....	68

Figure 19: Simulated melt temperature along the length of the extruder for Runs 1-4.....	74
Figure 20: Cross section of a Barrier screw. The solid bed is kept separate from the melt in the melting section	76
Figure 21: Simulated melt temperature along the length of the extruder for Run 5-8	77
Figure 22: A small section of the Barrier screw utilized in the validation is shown in this figure. The various changes in geometry is done to control the temperature and homogeneity of the final melt.....	78
Figure 23: Simulated melt temperature along the length of the extruder for Run 9-10	80
Figure 24: Simulated melt pressure during recovery along the length of the extruder for Run 1-4.....	83
Figure 25: Simulated melt pressure during recovery along the length of the extruder for Run 5-8.....	86
Figure 26: Simulated melt pressure during recovery along the length of the extruder for Runs 9 and 10.....	87
Figure 27: Simulated melt viscosity gradient along the length of the extruder for Runs 1-4.....	91
Figure 28: Simulated viscosity data versus melt temperature for Runs 1-4.....	92
Figure 29: Viscosity curve for HDPE with MFI of 2g/10min.....	93
Figure 30: Simulated melt viscosity gradient along the length of the extruder for Runs 5-8.....	94
Figure 31: Simulated viscosity data versus melt temperature for HDPE (Runs 5-8)	95
Figure 32: Simulated melt viscosity gradient during recovery along the length of the extruder for Runs 9-10.....	96
Figure 33: Simulated viscosity data versus melt temperature for Runs 9-10.....	99
Figure 34: Variation of melt temperature at the screw tip versus different number of grid points as well as their relative differences to the benchmark data (Run 1).....	105
Figure 35: Variation of recovery rate versus different number of grid points as well as their relative differences to the benchmark data (Run 1).....	105

Figure 36: Variation of screw torque versus different number of grid points as well as their relative differences to the benchmark data (Run 1).....	106
Figure 37: Variation of melt temperature at the screw tip versus different number of grid points as well as their relative differences to the benchmark data (Run 5).....	107
Figure 38: Variation of recovery rate versus different number of grid points as well as relative difference to benchmark data (Run 5).....	107
Figure 39: Variation of screw torque versus different number of grid points as well as their relative differences to the benchmark data (Run 5).....	108
Figure 40: Variation of melt temperature at the screw tip versus different number of grid points as well as relative difference to benchmark data (Run 9).....	109
Figure 41: Variation of recovery rate versus different number of grid points as well as relative difference to benchmark data (Run 9).....	109
Figure 42: Variation of screw torque versus different number of grid points as well as their relative differences to the benchmark data (Run 9).....	110
Figure 43: Variation of melt temperature versus certain variations of actual melt conductivity as well as their relative differences to the benchmark data (Run 1).....	112
Figure 44: Variation of screw torque versus various thermal conductivity values as well as their relative differences to the benchmark data (Run 1).....	113
Figure 45: Variation of melt temperature versus different thermal conductivity values as well as their relative differences to the benchmark data (Run 5).....	114
Figure 46: Variation of screw torque versus various thermal conductivity values as well as their relative differences to the benchmark data (Run 5).....	115
Figure 47: Variation of melt temperature versus different thermal conductivity values as well as their relative differences to the benchmark data (Run 9).....	116
Figure 48: Variation of screw torque versus thermal conductivity variation as well as their relative differences to the benchmark data (Run 9).....	117
Figure 49: Variation of melt temperature versus variation of heat capacity as well as their relative differences to the benchmark data (Run 1).....	118
Figure 50: Variation of screw torque versus heat capacity variation and their relative differences to the benchmark data (Run 1).....	119

Figure 51: Variation of melt temperature versus variation of heat capacity as well as their relative differences to the benchmark data (Run 5).....120

Figure 52: Variation of screw torque versus heat capacity variation as well as their relative differences to the benchmark data (Run 5).....120

Figure 53: Variation of melt temperature versus heat capacity as well as their relative differences to the benchmark data (Run 9).....121

Figure 54: Variation of screw torque versus different heat capacity values as well as their relative differences to the benchmark data (Run 9).....122

Figure 55: Cycle time versus screw torque for screw torque validation experiment125

Figure 56: Throughput versus screw torque for screw torque validation experiment126

Figure 57: Zero-shear rate viscosity: The viscosity change in the shear thinning polymers is minimal at lower shear rate values.....134

List of Appendices

Appendix A: The fourth and fifth-order algorithm for Runge-Kutta method with Cash-Carp development

Appendix B: Melting behavior and thermal properties of HDPE and PET

Chapter 1

INTRODUCTION

In the polymer industry today, the design of new screws is mainly a trial and error venture based on experience and experiments in which the operating conditions, or the screw geometry are systematically changed until the desirable performance is met. An economical approach would be the use of a reliable prediction tool, which would reduce the number of experiments to a more economical size therefore save resources and material via limiting the screw designs and experimenting of operating conditions. The mathematical modeling of the phenomenon taking place inside an injection machine will make possible the use of prediction tools to study, predict, and simulate the performance of such systems in advance. The application of the prediction tools will also help to explore the possibility of processing new screw designs without having to conduct the actual expensive experiments. These predictive tools will also assist to calculate

important performance parameters, including recovery rate, melt temperature and pressure during recovery, power consumption, and length of screw required for melting of a given resin with specific material properties and operating conditions. These tools will help to pave the way for the optimal control of the extrusion and injection processes, which is very much desired by the polymer processing industry.

In order to develop analytical software, it is essential to develop mathematical models that can accurately describe the polymer's fate in industrially relevant geometries [Bigg 73, Bigg 74, Broszeit 97, Chiruvella 95, Elbirli 84, Hyun 97, Viriyayuth 84, Yamamuro 98]. The availability of such models facilitates further optimization of the processing conditions. Complex helical geometry of extruders makes it very challenging to develop the above models [Zicheng 98, Yu 97a, Booy 04, Laurence 75, Nebrensky 73, Wang 04]. In the past, various attempts have been made to predict and approximate the rheological phenomenon during the extrusion and injection processes. These attempts resort to several simplifications including geometrical approximation, which may result in the underestimation or overestimation of the process output and affect the reliability of simulations.

This work develops a three dimensional mathematical model to portray the flow of a molten polymer inside the helical path of a single screw injection molding machine. For the ease of visualization, we first develop the mass, momentum, and energy balances in cylindrical geometry and then transform those models to the helical coordinates. To that end, we derive and utilize the necessary transformation tools. Subsequently, we develop an iterative computational algorithm based on shooting Newton-Raphson method in order to simulate the mathematical model.

The simulation results are then validated against experimental data obtained from ten different runs utilizing an industrial injection molding machine, processing two different polymers — high density polyethylene (HDPE) and polyethylene terephthalate (PET). From the standpoint of industrial practice, the direct benefit of this work is the ability to

effectively calculate adequate various state variables throughout the extent of the injection molding machine.

At last, we study how the variation in the input of certain parameters in the developed mathematical model can qualitatively and quantitatively influence the variation in the responses of the model. The sensitivity of the final solutions for selected experiments from the validation effort with respect to different grid sizes and thermo-physical properties are analyzed and their impact on certain responses including final recovery rate, melt temperature, and screw torque are investigated.

1.1 Injection Molding Process

Injection molding is the most commonly used manufacturing process for the fabrication of plastic parts. A wide variety of products are manufactured using injection molding process, which vary greatly in their size, complexity, and application. The injection molding process requires the use of an injection molding machine, raw plastic material, and a mold. Figure 1 depicts a typical single screw injection molding machine manufactured by Husky IMS.

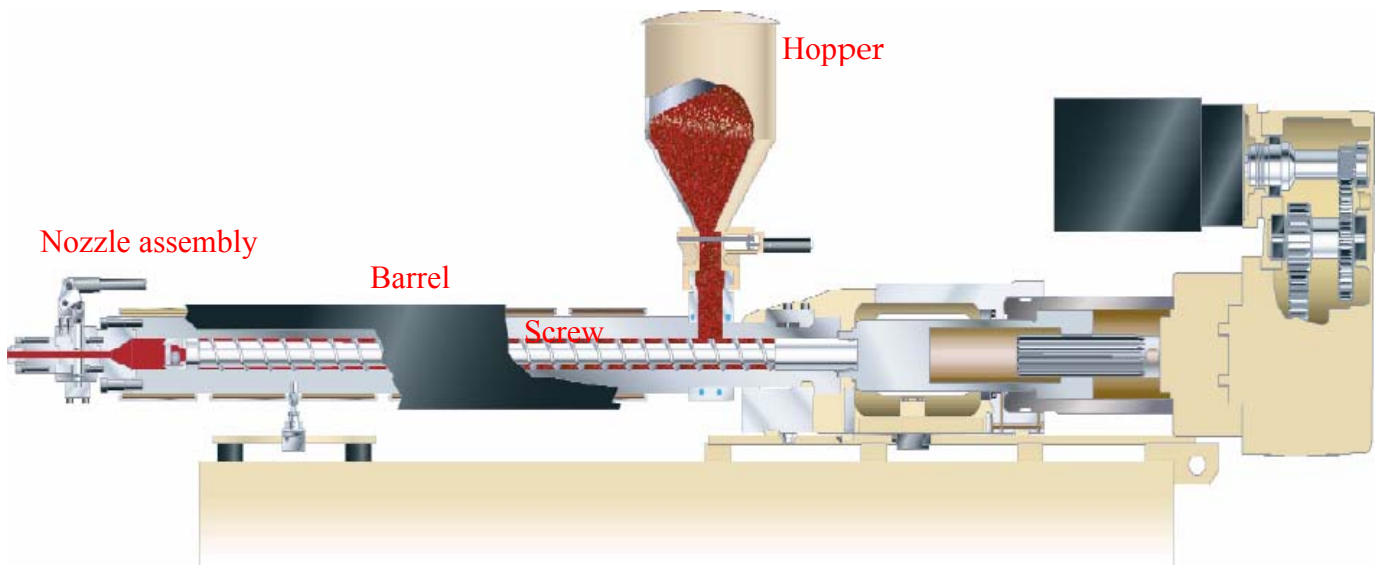


Figure 1: A schematic of a single screw Husky IMS injection machine

The plastic is fed through the hopper into the injection unit and melted by a combination of conduction through heating elements around the barrel and heat of dissipation through friction between the pellets and the screw. The final melt is then injected into the mold, where it cools and solidifies into the final part. The process cycle for injection molding is very short and normally consists of the following stages:

1. *Clamping* - Prior to the injection of the material into the mold, the two halves of the mold must first be securely closed by the clamping unit. Each half of the mold is attached to the injection molding machine and one half is allowed to slide. The clamping unit pushes the mold halves together and exerts sufficient force to keep the mold securely closed while the material is injected.
2. *Injection* - The raw plastic material, usually in the form of pellets, is fed into the injection molding machine, and advanced towards the mold by the injection unit. During this process, the material is melted by screw through heat (conduction and frictional). The molten plastic is then injected into the mold very quickly and the buildup of pressure packs and holds the material. The amount of material that is injected is referred to as the shot.
3. *Cooling and Holding* - The molten plastic that is inside the mold begins to cool as soon as it makes contact with the interior mold surfaces. As the plastic cools, it will solidify into the shape of the desired part. However, during cooling some shrinkage of the part may occur. The packing of material in the injection stage allows additional material to flow into the mold and reduce the amount of visible shrinkage. This process is referred to as *Holding* process.
4. *Ejection* - After sufficient time has passed, the cooled part may be ejected from the mold by the ejection system, which is attached to the rear half of the mold. When the mold is opened, a mechanism is used to push the part out of the mold. Force must be applied to eject the part because during cooling the part shrinks and adheres to the mold.
5. *Post Mold Cooling* – In some applications, the ejected parts are transferred into a post mold cooling unit to be cooled down to desired temperatures before the

packaging step. This will allow to shorten the “in-mold” time and subsequently the overall cycle time.

After the clamping stage and during the injection stage, pellets enter the region between the flights of the screw inside the injection unit. As shown in Figure 2, the polymer resin enters the region W between the two flights, “A” and “B”, of the screw. The depth of the screw (H) (in another words the radius of the screw shaft) varies along the length of the extruder. In this figure the melt is shown to move axially in the helical.

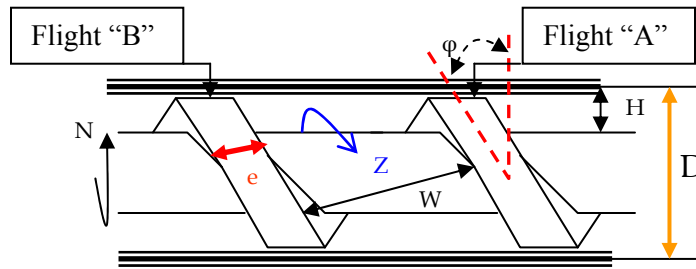


Figure 2: A schematic of the region around two flights of a screw

The focus of this research work is to study the behavior of the plastic material during melting process inside the helical shape of the screw.

The purpose of the screw is to produce, mix, and axially transport a well-melted, homogenized plastic in sufficient quantity to meet the production demand. Since thermal conduction contributes to the melting of polymer having a specific set of thermal properties, the design of the screw and processing conditions should be ideally optimized for each and every polymer type. Normally the function of extruder screws can be split into the following [Maddock 59]:

1. Feeding zone (conveying pellets from hopper to transition/melting section)
2. Melting or compression zone (converting pellets into a homogeneous and well-melted mixture)
3. Metering zone (pumping the melt through nozzles or dies)

The feeding zone of the screw is its first section in the direction of material flow and also contains the smallest screw diameter, where its function is conveying the solid axially towards the melting section. Typically, a feed section length of four to five diameters will allow enough pressure to develop and convey the material forward. During the flow passage through the feeding zone, the plastic is heated but kept below its melting temperature. In this study, it has been assumed that the first layer of melt appears as soon as the polymer enters the barrel. Movement of plastic in the feeding zone relies on adhesion of plastic to the barrel rather than the screw. The melting zone (also known as compression zone) is where the melting takes place. Here, the diameter of the screw shaft gradually increases, thereby forcing the material towards the barrel wall.

The primary melting mechanism in the feeding zone is the heat dissipation caused by friction rather than heat supplied from the barrel. Another important function of the melting zone is to keep air out of the melt. Air in the space between pellets entering the feed-throat is prevented from being dragged into the melt by the reducing flight depth in the melting zone. The ratio of feed depth to metering depth is called the compression ratio (CR). If the pressure gradient increases rapidly along the screw extruder, a smaller compression ratio needs to be chosen. This is the case for viscous polymers where a large CR causes rising of melt pressure in the screw channel that restricts the flow rate of the polymer melt. Another important note regarding CR is that two screws with same compression ratio but different depth values behave completely different. A 0.45/0.15 feed depth over metering depth will deliver a CR of 3:1 as well as a 0.3/0.1 ratio [Maddock 59], however the first screw will have a lower shear rate and higher output (not necessarily higher melt quality) as oppose to the latter case, which reacts the opposite (higher shear rate and lower flow rate). In the metering zone, the melting is complete and ready to be processed. The metering zone of the screw acts as a pump and sets the recovery rate of the screw.

In injection molding industry, screws must efficiently perform the tasks of pumping and recovering a shot of plastic melt at the available recovery time. The screws must be mechanically strong enough to handle rigorous injection processes [McKelvey 59, Chung

00, Colwell 59]. The task of screw designing is to find an optimum balance of all the tasks mentioned above. Ideally, it might be possible or advised to design a screw for each application. In the industry however, it is more desirable to rely on a set of screw designs to cover a wide range of plastic applications.

For certain materials or processes, the screw design is properly revised to accommodate the challenges in the process. Critical design elements that affect the output and quality of the extruders include: screw diameter, pitch, channel depth, compression ratio, screw L/D (more explanation on L/D is presented in section 4.4: The Screw L/D), mixing sections (dispersive and distributive), and length of each screw section. The proper L/D is determined by the process and application that is being satisfied. Figure 3 depicts the different zones of a typical simple screw.

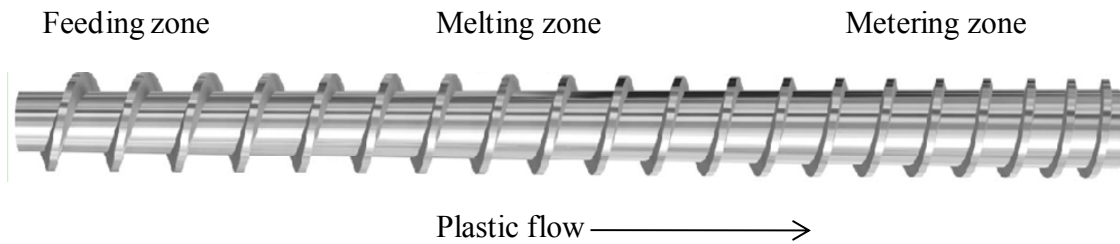


Figure 3: A schematic of a simple extruder screw

As can be seen in Figure 3, the screw shaft diameter increases gradually in the melting zone (this will be explained later in designing the mathematical equations). In the metering zone, the melting is complete and ready to be processed. The metering zone of the screw acts as a pump and sets the recovery rate of the screw. Theoretically, the recovery rate in an injection molding process is a function of three competing terms: drag flow (Q_d), pressure flow (Q_p), and leakage flow (Q_L) [Rauwendaal 86]. The recovery rate, Q , can be mathematically presented as:

$$Q = Q_d - Q_p - Q_L \quad (1.1)$$

Drag flow presents the maximum theoretical recovery rate that the screw can achieve. The pressure flow represents the negative influence on recovery from pressure in front of

the screw tip created by operating with backpressure. The greater the backpressure, the harder the screw has to work to recover the material. Increasing the backpressure results in increased work being done on plastic and creates better plastic mixing and melting however at the expense of increased pressure flow leading to decreased recovery rate. By increasing the backpressure, the pumping capability of the screw must work against more resistance to flow.

The leakage flow conceptually represents the leakage (back flow) across the lands of the screw flights. Leakage flow is proportional to the clearance area between tips of the screw flights and the barrel inside diameter. Wear of the screw and barrel will increase the screw to barrel clearance and increases the leakage flow and diminishes the recovery.

1.2 Development of Helical Coordinates

The non-orthogonal helical coordinate of an extruder screw is more complicated to develop than orthogonal natural system (e.g. cylindrical) but leads to better treatment of the flow behavior [Yu 97a, Yu 97b]. This research aims to develop the non-orthogonal model with no geometrical simplification. The advantages of such system can be described as:

- Using the true helical geometry. A comparison is done between the simulation results driven from helical model derived in this work and some commercially available models that have used simplified geometries in the development of their mathematical expressions. The results are summarized in Table 1:

Run	Throughput (kg/h)	Screw Torque (Nm)	Screw Power (kW)	Melt temp (°C)	Shear rate (1/s)
Experimental data	969	13472.54	121.65	283.12	29.78
Helical based simulation	961.65	13560.51	128.65	284.50	31.34
CompuPlast (Cartesian based model)	960.10	27412.06	266.13	308.74	612.80
PSI (Cylindrical based model)	973.55	38019.48	370.23	313.55	669.31

Table 1: A comparison between the helical based simulation tool developed in this work and non-helical based simulation packages. Results are compared with experimental data.

The version of the CompuPlast software used for the comparison purpose in this work was released in 2004 and the software is still under development. PSI is developed by the University of Paderborn in Germany and simulates manufacturing processes in single screw plasticizing units. It is a simplified cylindrical based model in which the simplified equations of change are solved to arrive at algebraic expressions. The program version for the comparison purpose in this work was released in 2001. Newer versions use the same strategy but are developed to include additional sections (e.g. wave section).

As can be seen in Table 1:

- Each model has been able to predict the throughput of the injection molding system with good accuracy.
 - The torque estimation with the geometrically simplified models has been between 2 to 3 times higher than the experimental data, while using the non-orthogonal model, for low and high process temperatures, the torque estimation has been within 2-3% of the actual experimental results.
 - Melt temperature prediction in the simplified models has been between 25-30°C higher than the measured values. The non-orthogonal model predicts melt temperature at the screw exit within 3-5°C of the actual results.
-
- Since the developed geometry is natural to that of the flow, the boundary conditions can be assigned without unnecessary approximations.
 - Inclusion of the tapering screw, which allows consideration of the screw details in the simulation that cannot be supported with the simplified models.
 - For the orthogonal system the modeling of the rotation of the screw element can be done by Multiple Reference Frames (MRF) and the Sliding Mesh techniques but with the non-orthogonal system (e.g. helical system) the helical axis itself can change place and orient so there is no need of using above techniques since the

screw rotation is defined with a mathematical expression. This will be defined later in the coordinate development section.

1.2.1 Application of Helical Geometry

Figure 4 depicts the actual geometry of a screw inside an extruder:

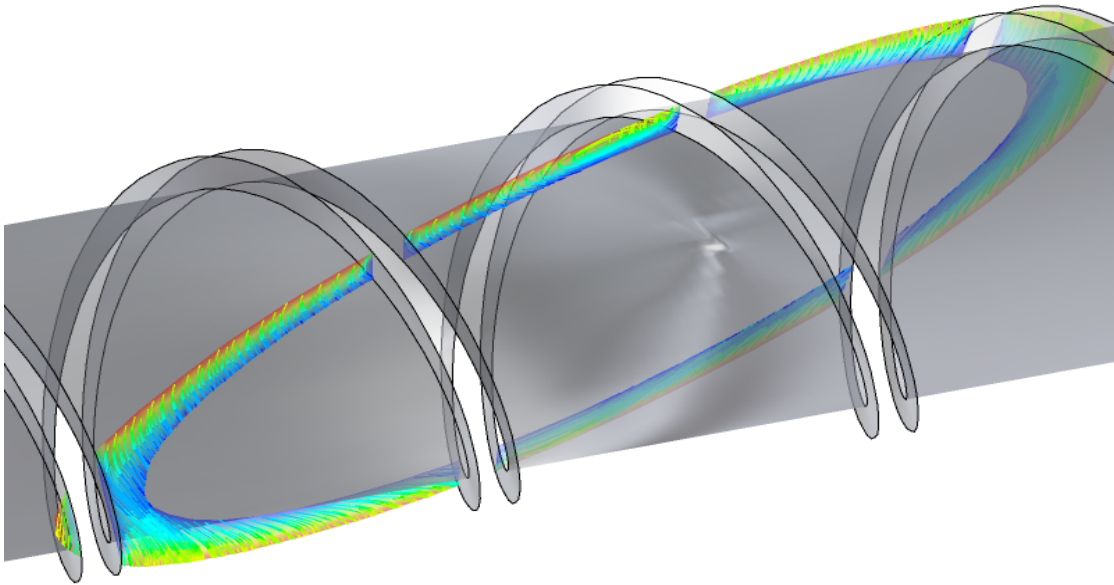


Figure 4: Helical geometry inside a single screw extruder

The helical motion can be viewed as a three dimensional motion with simultaneous rotation about and translation on an axis. The values of the helical rotation and translation are invariant to coordinate transformation, that is, they are independent of the chosen reference frame. During the motion of polymer melt in helical coordinates, the helical axis itself can change place and orient.

To further explain this approach, when a particle turns 1 radian in a helix, it sweeps “ r ” at the circumference. However, an axial displacement also occurs. The overall displacement of melt particle is the combination of these two movements (“ r ” at the circumference and “ k_4 ” in vertical displacement), therefore, the actual displacement travelled in helix direction for 1 radian will be $\sqrt{k_4^2 + r^2}$. Orthogonal systems are usually referred to as natural

systems. Systems where axes do not make a right angle are often called “physical” or non-orthogonal. In order to develop a physical system, the differential equations should be first developed in a natural system, and then using transformation equations, transformed to a desired physical system. Figure 5 depicts the orientation of the axes of a helical coordinate and correlates them to the same counterparts in a conventional system.

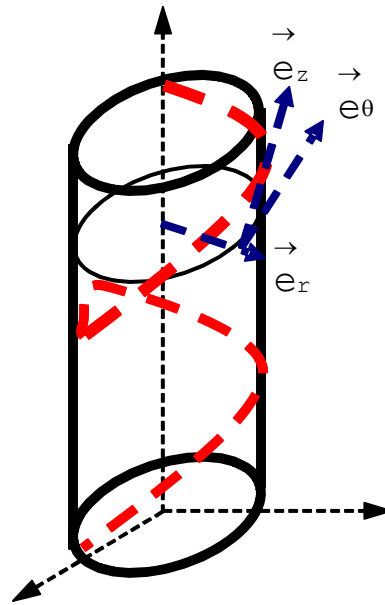


Figure 5: Helical axis coordinates: Normal (e_r), Tangential (e_θ) and Helical (e_z)

In Figure 5 the flow of the polymer melt in a section of helix is depicted with the red dotted line. The screw rotates with a velocity of N (m/s). If the geometry of screw is simplified to a rectangle, the flow has the option of moving in down channel, cross channel, and channel depth directions of the screw path. The early hydrodynamic analysis of melt flow in a screw had only considered this type of geometry [Chang 95, Cunha 94, Chung 71, Chung 75, Darnell 56, Fenner 77, Tadmor 67, Tadmor 70, Tadmor 72] and the equation of motion was solved for the down channel only. The average down channel velocity and the extruder throughput were obtained by integrating the velocity field over the cross channel direction. The analysis of the flow was simplified by assuming that the channel aspect ratio (width/depth ratio) was so large that the channel depth could not affect the down and cross channel flows. In some cases even two dimensional flow solutions were overlooked due to mathematical complication involved. In true geometry of a typical screw, the fluid travels through a helix path, which is formed by the flights of

the screw. The normal, tangential, and helical axes of an extruder screw can be correlated to the depth, cross, and down directions of a rectangular system respectively. As mentioned previously, transformers are needed to transform the equations of change from a natural geometry to a physical one. In this work, the derivatives and velocity profiles in a natural system (cylindrical coordinates) are transformed to a helical system, utilizing the chain rule and the laws of partial differentiation as follow [Aris 90]:

$$x_i = x_i(r, s, t) \Rightarrow \frac{dx_i}{dT} = \frac{dx_i}{dr} \frac{dr}{dT} + \frac{dx_i}{ds} \frac{ds}{dT} + \frac{dx_i}{dt} \frac{dt}{dT} \quad (1.2)$$

Based on the dependency of the parameters to the specific axes in helical coordinate, the equations are simplified and transformation matrices are developed. Below, the development of the velocity transformer is illustrated. The product of this development will generate the components of the velocity-transforming matrix (Figure 6).

$$\begin{bmatrix} u_r \\ u_\theta \\ u_z \end{bmatrix} = \begin{bmatrix} R & 0 & 0 \\ 0 & \frac{-1}{\sqrt{\left(\frac{x_1}{R}\right)^2 + k_4^2}} & \frac{1}{k_4} \\ 0 & 0 & R \end{bmatrix} \begin{bmatrix} u_1 \\ u_2 \\ u_3 \end{bmatrix}$$

Figure 6: Transformer matrix for velocity profiles

$$1. \quad r = \frac{x_1}{R}, \quad u_1 = u_r \quad (1.3)$$

$$u_r = \frac{dx_r}{dT} = \frac{dx_r}{dr} \frac{dr}{dT} + \frac{dx_r}{ds} \frac{ds}{dT} + \frac{dx_r}{dt} \frac{dt}{dT} = \frac{dx_r}{dr} \frac{dr}{dT} = Ru_1 \quad (1.4)$$

$$\text{where } \frac{dx_r}{dr} = R, \quad \frac{dr}{dT} = u_1 \quad (1.5)$$

$$2. \quad s = -x_2 \sqrt{\left(\frac{x_1}{R}\right)^2 + k_4^2}, \quad u_2 = u_\theta \quad (1.6)$$

$$u_\theta = \frac{dx_\theta}{dT} = \frac{dx_\theta}{dr} u_1 + \frac{dx_\theta}{ds} u_2 + \frac{dx_\theta}{dt} u_3 = \frac{1}{\sqrt{\left(\frac{x_1}{R}\right)^2 + k_4^2}} u_2 + \frac{1}{k_4} u_3 \quad (1.7)$$

$$\text{where } \frac{dx_\theta}{ds} = \frac{-1}{\sqrt{\left(\frac{x_1}{R}\right)^2 + k_4^2}}, \quad \frac{dx_\theta}{dt} = \frac{1}{k_4} \quad (1.8)$$

$$3. \quad t = \frac{x_3}{R} + k_4 x_2, \quad u_3 = u_z \quad (1.9)$$

$$u_z = \frac{dx_z}{dT} = \frac{dx_z}{dr} u_1 + \frac{dx_z}{ds} u_2 + \frac{dx_z}{dt} u_3 = R u_3 \quad (1.10)$$

$$\text{where } \frac{dx_z}{dt} = R \quad (1.11)$$

In Figure 6, u_1 , u_2 and u_3 represent the velocity profiles in cylindrical coordinate while u_r , u_θ and u_z correspond to the same profiles in a helical system. The minus sign in section 2 by convention and u_z , u_θ and u_z are in radian. The value under the square root is the distance along the flight or arc.

1.2.2 Transformer for velocity profiles

Based on the matrix shown in Figure 6, the velocity profiles in a helical coordinate for r , θ , and z directions can be specified by:

$$u_r = R \cdot u_1 \quad (1.12)$$

$$u_\theta = -\frac{1}{\sqrt{k_4^2 + r^2}} u_2 + \frac{1}{k_4} u_3 \quad (1.13)$$

$$u_z = R u_3 \quad (1.14)$$

In Equation (1.12), k_4 represents pitch of the screw.

1.2.3 Transformer for derivatives

With the same approach as the velocity profiles shown above, the derivative profiles in a helical system are related to their cylindrical counterparts by applying the chain rule and can be expressed by the following terms:

$$\frac{\partial}{\partial r} = \frac{1}{R} \frac{\partial}{\partial r} + \frac{rs}{(k_4^2 + r^2)R} \frac{\partial}{\partial \theta} \quad (1.15)$$

$$\frac{\partial}{\partial \theta} = -\sqrt{k_4^2 + r^2} \frac{\partial}{\partial \theta} + k_4 \frac{\partial}{\partial z} \quad (1.16)$$

$$\frac{\partial}{\partial z} = \frac{1}{R} \frac{\partial}{\partial z} \quad (1.17)$$

where, R represents the inner radius of the barrel ($R_s + \delta$), δ is the flight clearance, and s is the dimensionless helical coordinate

1.3 Geometries used in extrusion models

Cartesian and cylindrical coordinates are commonly used to explain the geometry of an injection unit or an extruder. The core reason is that the governing equations of flow in those coordinates are very well established. However, the true geometry of screw does not fit in such systems. The melt moves in a helix of a screw and can be viewed as a rotation around and translation (changing place) along an axis. The values of these rotations and translations are invariant to coordinate transformation.

1.4 Literature Survey

In helical coordinates (non-orthogonal), at least two axes are not perpendicular. Up to now, the concept of helical coordinate system has only been considered in very limited studies and not put into use as a simulation tool [Yu 97a]. In some publications although a helix is discussed, only 1D fluid is selected to obtain solutions [Yu 97a, Yu 97b]. While there has been acceptable treatment of non-isothermal and non-Newtonian fluids, simplification of the screw geometry has been mainly involved in various studies. The

most widely used simplification has been the unwrapping of the helix channel and presenting it as a straight, rectangular channel with moving barrel [Street 61, Tadmor 67].

Other simplifications include assumptions of Newtonian fluid with temperature independent thermo-physical properties and viscosity and flow in only one or two dimensions [Rauwendaal 98, Bigg 73, Bigg 74, Chiruvella 95].

Some researchers have solved the flow equations by using analytical methods in 1D [Agassant 96, O'Brian 92], finite difference method in 2D [Covas 99] and finite element in 3D with constant thermo-physical properties [Colwell 59, Griffith 62, Zamodits 69]. In addition, simplified approach based on a hybrid finite difference/finite element method was developed [Choi 87, Barton 02, Chang 95]. Three-dimensional non-Newtonian fluid flow in a geometrically simplified screw channel of a single screw extruder has also been investigated [Choo 80, Choo 81]. In all these approaches, either the geometry of the screw or the equations of change, especially the heat transfer equation and the thermo-physical properties are simplified. Some cases have neglected the contribution of the wall conduction effects, which is important in the accurate prediction of heat transfer, pressure and temperature rise, and other extruder characteristics [Creamer 76].

Zamodits [Zamodits 69] introduced a helical coordinate system to analyze molten flow in a single screw extruder, thus avoiding the geometrical simplifications (e.g. a long rectangular channel). Other researchers [Bigg 73, Bigg 74, Broszeit 97, Chiruvella 95, Elbirli 84, Hyun 97, Viriyayuth 84, Yamamuro 98] then adopted this approach. The study of Nebrensky et al. [Nebrensky 73] verified a relation between a natural basis and a physical basis (helical) through defined transformers. Laurence and Tung [Laurence 75] later showed that the transformers of Nebrensky were incomplete and presented their own, which were developed using a cylindrical system. The work by Laurence and Tung directly relates the movement at the direction of helix to the down channel direction and ignores a vertical movement. Wang et. al, [Wang 04] set up their helical system from a rectangular natural system. Yu et.al, [Yu 97a, Yu 97b] developed a different helical

coordinate frame and compared it with classical rectangular and cylindrical coordinate systems.

A summary of all the developed transformers mentioned above is shown in Table 2. None of these systems has provided explicit equations of change for the motion of a non-Newtonian flow in a 3D environment with no physical or thermo-physical simplifications (i.e. variation of viscosity, density, thermal conductivity, and volumetric heat capacity with respect to temperature). In Yu et.al, [Yu 97a, Yu 97b], the thermo-physical and viscosity properties are assumed to be constant and only the effect of curvature and helicity on the velocity profile of a 1D fully developed Newtonian flow along a helical channel is presented.

Researcher	Transformer in radial direction	Transformer in θ direction	Transformer in z direction
[Nebrensky 73]	$r = \frac{R}{R_b}$	$\theta = \theta \sqrt{\frac{r^2}{R_b^2} + \frac{L^2}{2\pi R_b^2}}$	$z = \frac{Z}{R_b} + \frac{L}{2\pi R_b} \theta$
[Laurence 75]	$r = r$	$\theta = a z + \theta$	$z = z$
[Wang 04]	$x = \bar{r} \cos \bar{\theta}$	$y = \bar{r} \sin \bar{\theta}$	$z = \bar{z} + \frac{L}{2\pi} \bar{\theta}$
[Yu 97a]	$x = r \cos[\varphi(l) + \theta]$	$y = r \sin[\varphi(l) + \theta]$	$z = l$

Table 2: Comparison of selected transformers developed by various researchers

In this research, we revised the approach by Nebrensky et. al and the corrected transformers are used to setup the three dimensional helical system.

Chapter 2

EXPERIMENTAL SETUP

In order to validate the prediction tool designed in this work, a series of experiments in the form of a design of experiment (DOE) was conducted and the results compared with the simulation predictions. A high density polyethylene (HDPE- Eltex B4020N1343 provided by BP SOLVAY) with melt flow index (MFI) of 2.0 g/10min and a polyethylene terephthalate (PET- INVISTA 1101 provided by INVISTA CANADA) with intrinsic viscosity (IV) of 0.83 dl/g were used in these experiments. PET has a unique ability to dramatically increase the viscosity of the liquid it is dissolved in, even at very low concentrations. IV is a quantitative assessment of this ability. Some of the properties of the resins utilized are presented in Table 3, including rheological parameters related to the Cross-WLF viscosity model, melt density, specific heat capacity, heat of fusion, and melting temperature.

Physical properties	PET	HDPE	Units
IV	0.83	-	dl/g
MFI	-	2.0	g/10min
Density	1.40	0.94	g/cm ³
Melting Point	245	138	°C
Melt Density	1.2	0.8	g/cm ³
Specific Heat Capacity	1.94	2.25	J/g°C
Heat of Fusion	65.5	45.0	J/g
n	0.5	0.4053	-
τ^*	60219855	52800	Pa
D1	3.839e+13	6.68e17	Pa.s
D2	373.00	153.15	K
A1	31.740	37.928	-
A2	40.9892	51.6000	-

Table 3: Some physical and rheological properties of the solid HDPE and PET grades provided by the resin suppliers and utilized in the experiments.

A schematic of the injection unit used in the experiments is shown in Figure 7. The vehicle to the test was a 400 ton injection molding machine. It was capable of processing different types of resins and screw designs including General Purpose and Barrier screws for processing of high density polyethylene, and PET screw for processing of PET resins. Due to the confidentiality agreements with Husky Injection Molding Systems Ltd., the configuration of the screw designs cannot be shown in this study. All screws had outside diameter of 80 mm and length of 25:1 L/D.

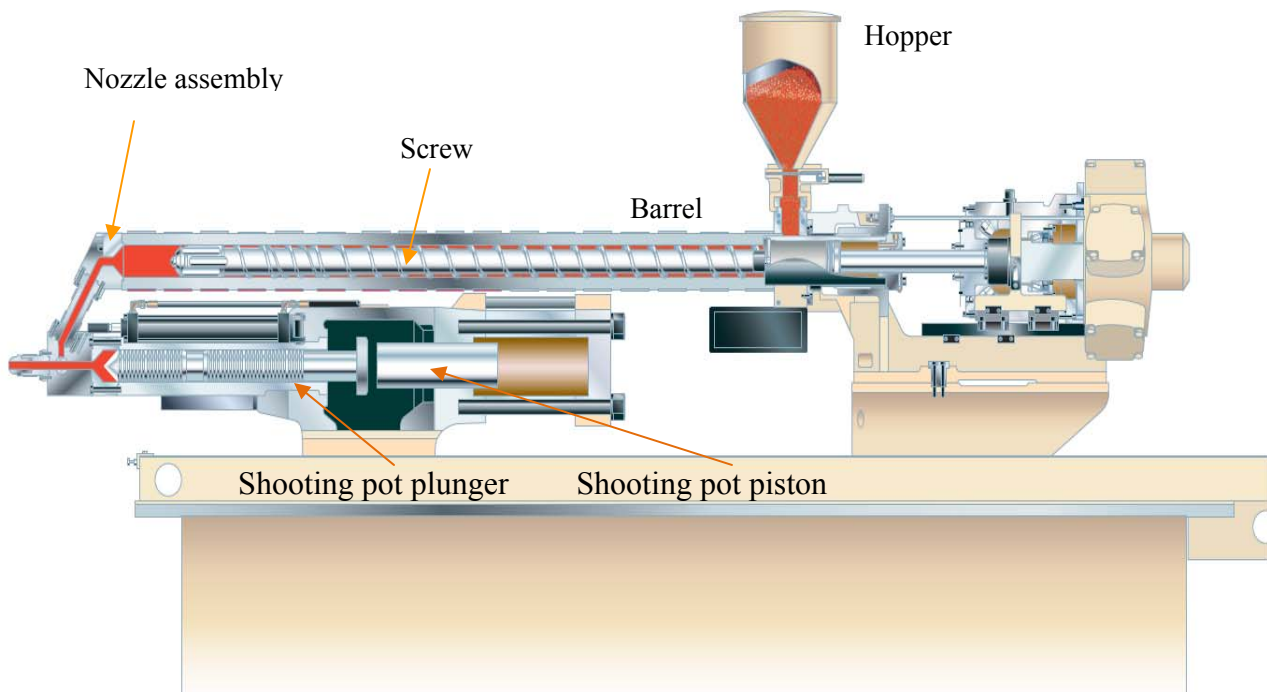


Figure 7: Schematic of the 400 ton injection molding system used in the validation of the simulation results. Different components of the system are shown on the injection unit.

2.1 Drying of PET Resin

Unlike the other major packaging resins (e.g., polyolefin, polystyrene, and PVC), PET pellet is an extremely hygroscopic thermoplastic, in that it readily absorbs moisture from the atmosphere. The presence of small amounts of moisture will hydrolyze PET in the melt phase, severely reducing its molecular weight. As a result, mechanical properties of PET decrease and end-product quality is compromised. Therefore, PET must be thoroughly dry just prior to melt processing. Figure 8 depicts the drop in the intrinsic viscosity of PET resin in the melt phase due to retained moisture content after the drying process (figure is from the PET Technology course material by Dr. Saleh Jabarin-University of Toledo).

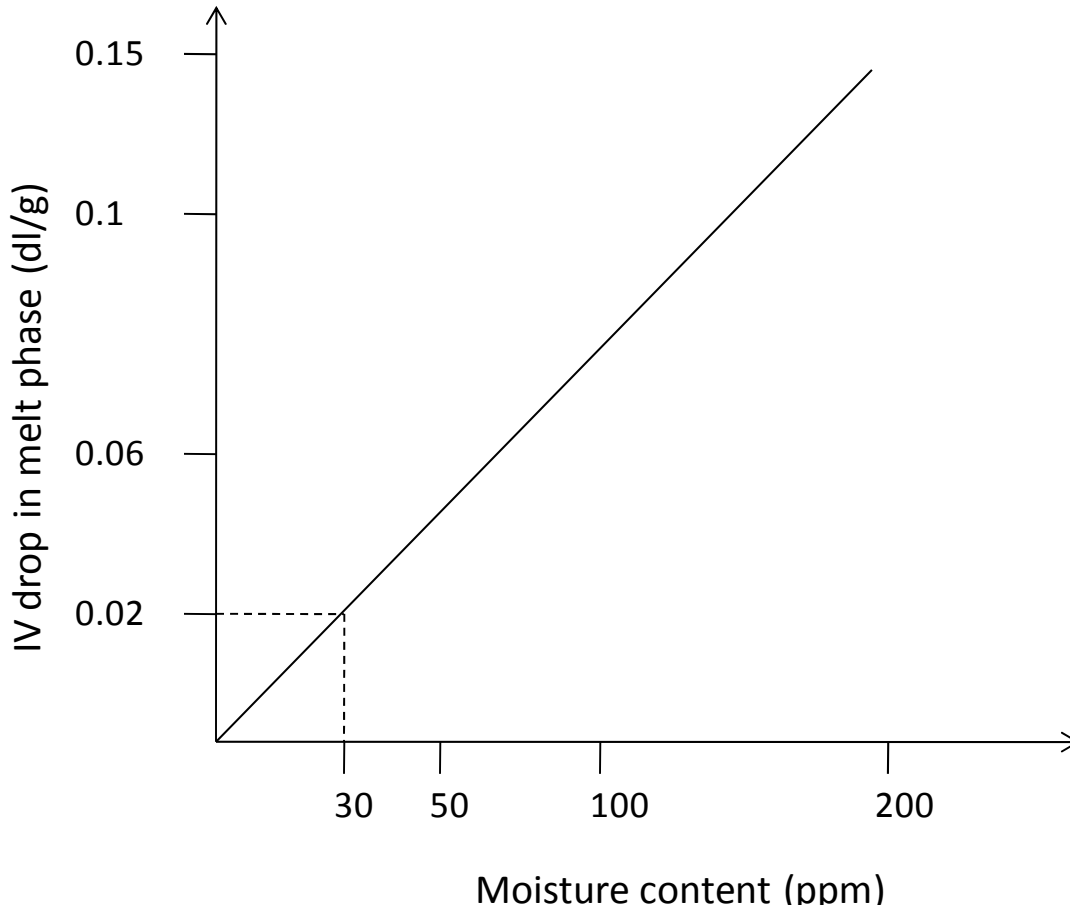


Figure 8: IV drop in the melt phase with respect to resin moisture content after drying process

The acceptable industry standard for the drop in the IV of the PET resin after the drying process is 0.02 dl/g, thus the physical properties of the final products are not affected.

PET is produced by a condensation reaction. Various starting materials are used and reacted in a series of steps to produce PET. This reaction, which also produces water, is reversible. Therefore, when un-dried PET is melted, the resin and water chemically react. Hydrolysis occurs and key mechanical properties of the PET are reduced. This hydrolysis reaction also changes PET melt viscosity and crystallization rate, making it very difficult to process into a quality end product.

Most PET drying is done in dehumidifying hoppers using hot air at a very low dew point. The dehumidified air passes through a bed of PET to extract moisture from the resin. A

desiccant material, such as silica, absorbs moisture from the circulating air. PET must be dried to <30 parts per million and maintained at this moisture level to minimize hydrolysis during melt processing. A dry resin will help control the Intrinsic Viscosity (IV) loss, which should be less than 0.02 dl/g. The PET should be dried at 170°-180°C, as a result, the initial PET resin temperature in the simulation tool is usually between 170 to 180°C compared to HDPE, which is at room temperature. Figure 9 depicts the dryer unit used at the experiments, which was located at the mezzanine level of the building where the injection unit was located and attached to the hopper of the injection unit.



Figure 9: The Piovani resin dryer (3500 Liter DP628L) utilized in the validation test

2.2 Extruder Instrumentation

The extruder was instrumented with control hardware to measure the melt pressure at the screw tip, (Kistler 6081A pressure transducer), and thermocouple to measure the melt temperature at the machine nozzle location, (Dynisco TG422J). The location of the temperature and pressure sensors are shown in Figure 10. The screw torque and the heater power draw were obtained from the motor amperage indicated by the machine control system.

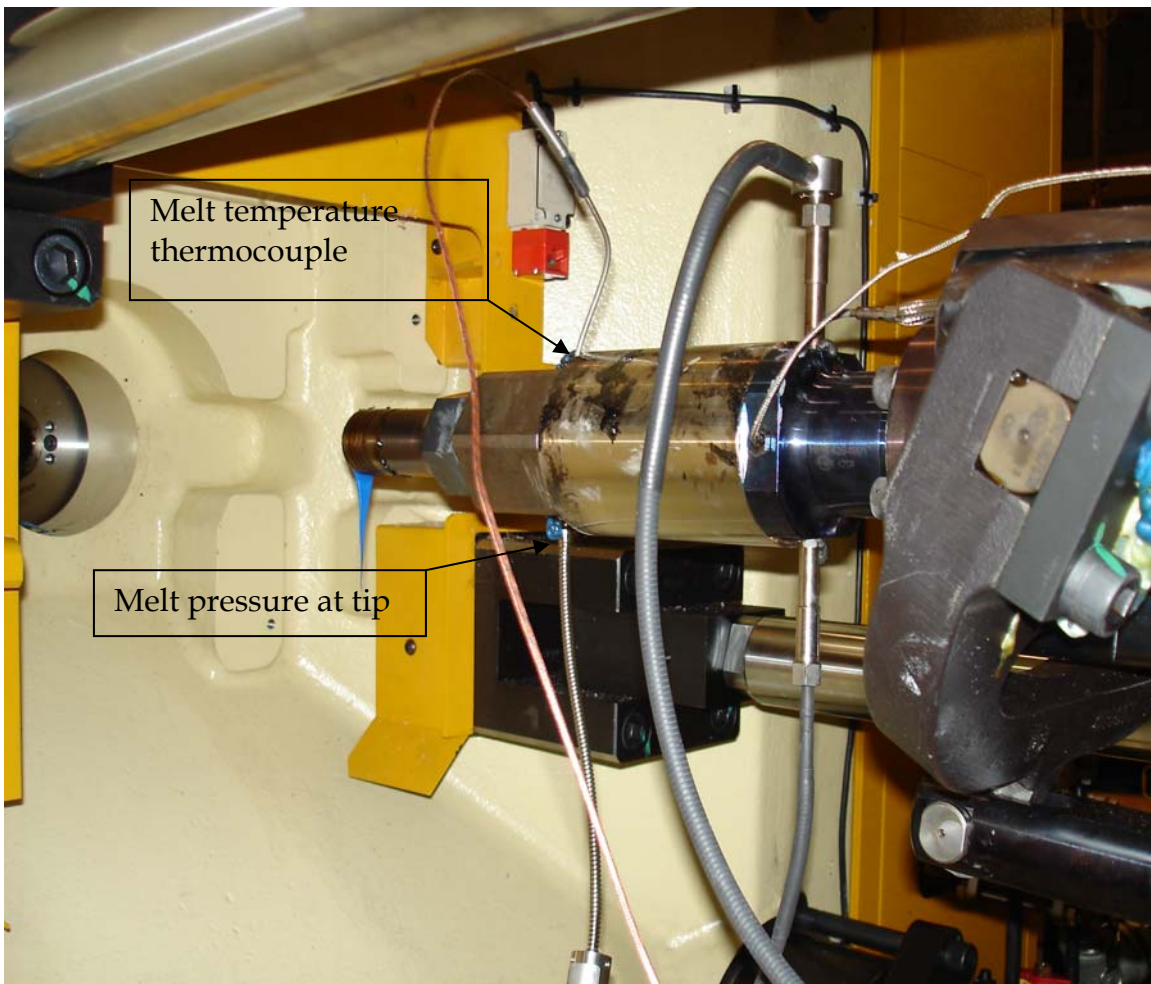


Figure 10: Location of the melt pressure and temperature sensors at the injection unit

The experimental procedure for the data collection was as follow:

1. Install the screw and establish the benchmark process using pre-defined operating conditions.
2. Wait until the process stabilizes (30 minutes).
3. Read and record the motor amperage indicated by the machine control system for the screw torque and heater power draw.
4. Purge the melt and measure the melt temperature using the temperature probe for 3 repetitions.
5. Read and record the pressure value using the data acquisition system.
6. Alter processing conditions based on the Design of Experiment and collect the required data.
7. Switch the screw to the next design.
8. When using PET resin, purge the HDPE resin thoroughly, switch to PET screw and conduct the steps above.

2.3 Design of Experiment

The Design of Experiment (DOE) is a planned approach for determining the relationship between cause and effect. This technique can be applied to any process with measurable inputs and outputs.

The basic goal of the DOE is to gain a sophisticated understanding of the relationship between variables that are varied within the experiment (factors) and their effect on the output (responses). This knowledge can be an extremely helpful tool to develop a new process or to improve the present one. The stability of the process can be enlarged, which means that it is minimally affected by external sources of variability. Any process can be considered as a black box, which will be affected by various controllable variables (X). These variables are the input factors. There are outputs or responses (Y), which can be measured. Nevertheless, there are always variables, such as environmental conditions, which cannot be controlled or sometimes not even be identified. These variables are the major cause for variability in the responses. Other sources of variability can be deviation around the set point or sampling and measurement errors. For good process knowledge it is essential to assess the variability of the system. Statistical Process Control (SPC) is a sophisticated tool for simply monitoring and filtering out the noise caused by variability, but it is a passive approach. For systematic improvements and breakthroughs a DOE application is required.

The traditional technique to get a better knowledge of the process is to change one factor-at-a-time (OFAT). This methodology is both time- and cost-consuming and no interactions between factors can be estimated. The DOE allows the changing of several independent factors at once and observing them simultaneously. The benefits of using Design of Experiment are listed in Table 4.

Benefits of Design of Experiment	
1	Very efficient; minimum number of required runs
2	Hidden replications constructed by running the design points
3	Interactions can be detected
4	Analysis is easy
5	Interpretation is not difficult
6	Design can be applied sequentially
7	Complex designs like Response Surface designs can be created

Table 4: Benefit of using Design of Experiment

The most important benefit of this method is the immense reduction of number of runs. These runs are assessed in a particular way and statistical calculations methods are required for analyzing the responses. The result of the analysis of the gathered data is an empirical mathematical model, which includes all vital input factors. This model, a first-order, second-order or a cubic model, describes the process with a function. Therefore, it provides predictions without running further experiments. Statistics, which are included in the analysis of variance (ANOVA), prove the statistical significance of the model.

It is relevant and quite important to determine the influence of and the interactions between the various input variables. Considering the time consumption and cost intensive characteristics of experimental works involved in the evaluation of the screw design and/or new polymers and processing conditions, it was decided to adopt a full factorial DOE to compare the experimental data and the prediction results. The independent variables susceptible of influencing the experimental results (dependent or output variables) are classified in several levels of intensity. The effect of a factor is defined as the change in response that results from a change in the factor level. The interaction between factors corresponds to the different responses observed when the level of one factor is changed, and the differences in response between the levels of this factor are not identical at all levels of the other factors.

Table 5 presents the independent factors chosen to be varied in this work plus a summary of the experimental results. The inputs to the experiments are:

1. Screw geometry
2. Complete characterization of the materials
 - a. Rheology – Melt
 - b. Thermodynamics – C_p , T_{melt} , Density
 - c. Mechanical
3. Operating conditions – screw speed, back pressure, cycle time, initial process settings, and the shot size

Run	Resin	Barrel temp (°C)	Screw speed (rpm)	Recovery time (sec)	Melt temp (°C)	Torque (Nm)	Shot weight (g)	Nozzle pressure (bar)
1	HDPE MFI=2g/10min GP (25:1)	210	190	1.76	244.2	4402	180	1149.6
2			286	1.36	245.0	4874	240	1135.0
3		230	190	1.76	253.0	4239	180	1113.0
4			286	1.36	252.8	4656	240	1101.0
5	HDPE MFI=2g/10min Barrier (25:1)	210	190	1.76	245.3	4402	180	1149.6
6			286	1.36	245.9	4874	240	1135.0
7		230	190	1.76	254.1	4239	180	1113.0
8			286	1.36	255.2	4656	240	1101.0
9	PET, IV=0.83dl/g PET (25:1)	285	300	2.70	299.3	8803	640	-
10		300		3.10	306.4	8085	640	-

Table 5: Design of experiment prepared for the validation of screw prediction tool results

Chapter 3

MATHEMATICAL MODELING AND SIMULATION

The mathematical modeling of the equations of change developing inside an injection machine or an extrusion unit will make possible the use of prediction tools to study the performance of systems under evaluation. This work discusses the implementation of such prediction tools for single screw injection molding machines. The mathematical modeling of injection molding process is a multi-objective problem, where it is necessary to satisfy simultaneously several measures such as mass flow rate, length of screw required for melting, melt temperature, and melt pressure during the recovery operation. Due to the complexity of the governing equations and the boundary conditions, analytical

methods can only be used in very few practical circumstances and numerical approaches are generally needed to obtain a reliable solution. However, analytical solutions are valuable for validating the physical insight into the basic mechanism and expected trends, and results for limiting or asymptotic conditions.

3.1 Momentum Balance- θ Direction; Helical

The unknowns in the extrusion and injection molding processes are the velocity, pressure, and temperature as function of r , θ , and z axes. Velocity distributions in the extruder are known by depending on the pressure in local equations of motion, which are the equations that describe the behavior of a system under the influence of applied force. Below, the equations of motion in cylindrical coordinate are developed and then transformed into a helical system. Since the viscosity is a function of temperature, the shear stress components (e.g. $\tau_{r\theta}$) need to take into account the variation of viscosity and shear rate in any rheological model that is used to illustrate the behavior of viscosity (in this study the power-law and Cross WLF viscosity models are utilized to define the rheological behavior of the polymer melt inside the helix channel).

$$\frac{\partial}{\partial t} (\rho V_\theta) dr d\theta dz = -dr d\theta dz \left(\frac{\partial}{\partial r} \phi_{r\theta} \right) - dr d\theta dz \left(\frac{\partial}{\partial \theta} \phi_{\theta\theta} \right) - dr d\theta dz \left(\frac{\partial}{\partial z} r \phi_{z\theta} \right) \quad (3.18)$$

Where

$$r = a + bz \quad (3.19)$$

$$\phi_{r\theta} = \tau_{r\theta} + \rho V_r V_\theta \quad (3.20)$$

$$\phi_{\theta\theta} = P + \tau_{\theta\theta} + \rho V_\theta^2 \quad (3.21)$$

$$\phi_{z\theta} = \tau_{z\theta} + \rho V_z V_\theta \quad (3.22)$$

$$\begin{aligned}
0 &= -\frac{\partial}{\partial r} (\tau_{r\theta} + \rho V_r V_\theta) - \frac{\partial}{\partial \theta} (P + \tau_{\theta\theta} + \rho V_\theta^2) - \frac{\partial}{\partial z} [r(\tau_{z\theta} + \rho V_z V_\theta)] \\
&= -\frac{\partial \tau_{r\theta}}{\partial r} - \frac{\partial P}{\partial \theta} - \frac{\partial \rho}{\partial T} \frac{\partial T}{\partial \theta} V_\theta^2 - 2\rho V_\theta \frac{\partial V_\theta}{\partial \theta} - bR[\tau_{z\theta} + \rho V_z V_\theta] \\
&\quad - (a + bz) \left[\frac{\partial \tau_{z\theta}}{\partial z} + \frac{\partial \rho}{\partial z} V_z V_\theta + \frac{\partial V_z}{\partial z} \rho V_\theta + \frac{\partial V_\theta}{\partial z} \rho V_z \right] \\
&= -\frac{\partial \tau_{r\theta}}{\partial r} - \frac{\partial P}{\partial \theta} - \rho V_\theta \frac{\partial V_\theta}{\partial \theta} - bR[\tau_{z\theta} + \rho V_z V_\theta] - (a + bz) \left[\frac{\partial \tau_{z\theta}}{\partial z} + \frac{\partial V_\theta}{\partial z} \rho V_z \right] \\
&\quad - V_\theta \left[\frac{\partial \rho}{\partial \theta} V_\theta + \frac{\partial V_\theta}{\partial \theta} \rho + (a + bz) \frac{\partial V_z}{\partial z} \rho + (a + bz) V_z \frac{\partial \rho}{\partial z} \right]
\end{aligned} \tag{3.23}$$

Note that b in Equation (3.19) is the taper of the screw, and a is the initial value of r . The incorporation of b as taper parameter enables accurate simulation of polymer flow through tapered channels. Using the above terms and utilizing the transforming equations, the following is the momentum balance along θ direction in helical geometry:

$$\begin{aligned}
\frac{r\eta}{RM} \frac{\partial^2 V_\theta}{\partial z^2} &= \left(\frac{\rho R r V_z}{M} - \frac{r}{RM} \frac{\partial \eta}{\partial z} + b r \eta \right) \frac{\partial V_\theta}{\partial z} + \left(\frac{1}{Rr} A_4 - \frac{\eta}{(Rr)^2} \right) A_2 - A_3 \left(\frac{\eta}{R} - A_4 \right) \\
+ \eta &\left(\frac{-1}{R^2 M} \frac{\partial^2 V_\theta}{\partial r^2} + \frac{1}{R^2 k_4} \frac{\partial^2 V_z}{\partial r^2} - \frac{2rs}{R^2 M^3} \frac{\partial^2 V_\theta}{\partial r \partial \theta} + \frac{2rs}{R^2 M^2 k_4} \frac{\partial^2 V_z}{\partial r \partial \theta} - \frac{(rs)^2}{R^2 M^5} \frac{\partial^2 V_\theta}{\partial \theta^2} + \frac{\eta (rs)^2}{R^2 M^4 k_4} \frac{\partial^2 V_z}{\partial \theta^2} \right) \tag{3.24} \\
- M \frac{\partial P}{\partial \theta} &+ \rho A_2 A_1 + b \rho R^2 V_z A_2 + \left[\frac{R \rho V_z}{k_4} - \frac{r}{R^2 k_4} \frac{\partial \eta}{\partial z} \right] \frac{\partial V_z}{\partial z}
\end{aligned}$$

In the above equation, k_4 is pitch of the screw, and η is polymer viscosity. V_θ and V_z represent melt velocity in screw angular and axial directions and s is the dimensionless helical coordinate and given by the product of $-\theta$ and M . In addition, the following terms are used to simplify Equation (3.24):

$$\begin{aligned}
M &= \sqrt{k_4^2 + r^2}; A_1 = \frac{\partial V_\theta}{\partial \theta}; A_2 = \frac{V_\theta}{M}; A_3 = \frac{1}{RM} \frac{\partial V_\theta}{\partial r} - \frac{rs}{RM^3} \frac{\partial V_\theta}{\partial \theta}; \\
A_4 &= \frac{1}{R} \frac{\partial \eta}{\partial r} + \frac{rs}{RM^2} \frac{\partial \eta}{\partial \theta}
\end{aligned} \tag{3.25}$$

As can be seen, Equation (3.24) is a partial differential equation with the order of two for the angular melt velocity gradient with respect to axial direction ($\frac{\partial^2 V_\theta}{\partial z^2}$). In order to

convert the above equation to an ordinary first order differential equation, the first partial derivative is defined as a new state variable

$$\alpha = \frac{\partial V_\theta}{\partial z} \quad (3.26)$$

in order to help obtain a set of ordinary differential equations for model simulation.

3.2 Momentum Balance-Z Direction-Helical

Following the same approach as the momentum balance in θ direction, the momentum balance in z direction of a cylindrical coordinate is developed and then transformed into the helical geometry. Thus,

$$\frac{\partial}{\partial t} (\rho V_z) dr d\theta dz = - dr d\theta dz \left(\frac{\partial}{\partial r} \varphi_{rz} \right) - dr d\theta dz \left(\frac{\partial}{\partial \theta} \varphi_{\theta z} \right) - dr d\theta dz \left(\frac{\partial}{\partial z} r \varphi_{zz} \right) \quad (3.27)$$

where

$$\varphi_{rz} = \tau_{rz} + \rho V_r V_z \quad (3.28)$$

$$\varphi_{\theta z} = \tau_{\theta z} + \rho V_\theta V_z \quad (3.29)$$

$$\varphi_{zz} = P + \tau_{zz} + \rho V_z V_z \quad (3.30)$$

In the following, the momentum equation is first developed and then transformed to the helical geometry:

$$0 = \frac{\partial}{\partial r} (\tau_{rz} + \rho V_r V_z) - \frac{\partial}{\partial \theta} (\tau_{\theta z} + \rho V_\theta V_z) - \frac{\partial}{\partial z} [r(P + \tau_{zz} + \rho V_z V_z)] \quad (3.31)$$

$$0 = - \frac{\partial \tau_{rz}}{\partial r} - \frac{\partial \tau_{\theta z}}{\partial \theta} - \frac{\partial \rho}{\partial \theta} V_\theta V_z - \frac{\partial V_\theta}{\partial \theta} \rho V_z - \frac{\partial V_z}{\partial \theta} \rho V_\theta - bR [P + \rho V_z V_z] - (a + bz) \frac{\partial P}{\partial z} + \frac{\partial \rho}{\partial z} V_z^2 + 2V_z \frac{\partial V_z}{\partial z} \rho \quad (3.32)$$

$$0 = - \frac{\partial \tau_{rz}}{\partial r} - \frac{\partial \tau_{\theta z}}{\partial \theta} - \frac{\partial V_z}{\partial \theta} \rho V_\theta - bR [P + \rho V_z^2] - (a + bz) \frac{\partial P}{\partial z} - (a + bz) V_z \frac{\partial V_z}{\partial z} \rho - V_z \frac{\partial V_\theta}{\partial \theta} \rho + \frac{\partial \rho}{\partial \theta} V_\theta + (a + bz) \frac{\partial V_z}{\partial z} \rho + (a + bz) \frac{\partial \rho}{\partial z} V_z \quad (3.33)$$

In the following, each element of the Equation (3.33) is transformed to the helical geometry separately to obtain the final momentum balance equation in z direction:

$$1) \frac{V_\theta}{Rr} \times \frac{\partial V_z}{\partial \theta} = \left(\frac{-1}{r^h M} V_\theta + \frac{1}{r^h k_4} V_z \right) \cdot \left(-M \frac{\partial V_z}{\partial \theta} + k_4 \frac{\partial V_z}{\partial z} \right) = \frac{V_\theta}{r} \frac{\partial V_z}{\partial \theta} - \frac{k_4}{Mr} V_\theta \frac{\partial V_z}{\partial z} - \frac{M}{k_4 r} V_z \frac{\partial V_z}{\partial \theta} + \frac{V_z}{r} \frac{\partial V_z}{\partial z} \quad (3.34)$$

$$2) V_z \frac{\partial V_z}{\partial z} = R V_z \cdot \frac{\partial V_z}{\partial z} \quad (3.35)$$

$$3) - \frac{\partial P}{\partial z} = \frac{-1}{R} \frac{\partial P}{\partial z} \quad (3.36)$$

$$4) \frac{\eta}{Rr} \frac{\partial V_z}{\partial r} = \eta \left(\frac{1}{Rr} \frac{\partial V_z}{\partial r} + \frac{s}{M^2} \frac{\partial V_z}{\partial \theta} \right) \quad (3.37)$$

$$5) \frac{\partial \eta}{\partial r} \frac{\partial V_z}{\partial r} = \frac{1}{R} \frac{\partial \eta}{\partial r} \frac{\partial V_z}{\partial r} + \frac{rs}{M^2} \frac{\partial \eta}{\partial r} \frac{\partial V_z}{\partial \theta} + \frac{r s}{M^2} \frac{\partial \eta}{\partial \theta} \frac{\partial V_z}{\partial r} + \frac{Rr^2 s^2}{M^4} \frac{\partial \eta}{\partial \theta} \frac{\partial V_z}{\partial \theta} \quad (3.38)$$

$$6) \eta \frac{\partial}{\partial r} \left(\frac{\partial V_z}{\partial r} \right) = \frac{\eta}{R} \frac{\partial^2 V_z}{\partial r^2} + 2 \frac{\eta rs}{M^2} \frac{\partial^2 V_z}{\partial r \partial \theta} + \frac{\eta Rr^2 s^2}{M^4} \frac{\partial^2 V_z}{\partial \theta^2} \quad (3.39)$$

Finally, after the transformation to the helical geometry, we obtain

$$\Rightarrow (R^2 r V_z \rho) \frac{\partial V_z}{\partial z} = A_4 \left(\frac{\partial V_z}{\partial r} + \frac{rs}{M^2} \frac{\partial V_z}{\partial \theta} \right) - r \frac{\partial P}{\partial z} + RM^2 \left(\frac{\partial \eta}{\partial \theta} \frac{\partial V_z}{\partial \theta} + \eta \frac{\partial^2 V_z}{\partial \theta^2} \right) - bR \left[P + \rho (R V_z)^2 \right] + \frac{\eta}{R} \frac{\partial^2 V_z}{\partial r^2} + 2 \frac{\eta rs}{M^2} \frac{\partial^2 V_z}{\partial r \partial \theta} + \frac{\eta r^2 s^2}{RM^4} \frac{\partial^2 V_z}{\partial \theta^2} + \rho R M A_2 \frac{\partial V_z}{\partial \theta} \quad (3.40)$$

3.3 Momentum Balance-radial Direction-Helical

The momentum balance in the radial direction of a helical coordinate is shown below.

The same approach as the momentum balance in the other two directions is used:

$$\frac{\partial}{\partial t} (\rho V_z) dr d\theta dz = -dr d\theta dz \left(\frac{\partial}{\partial r} \phi_{rr} \right) - dr d\theta dz \left(\frac{\partial}{\partial \theta} \phi_{r\theta} \right) - dr d\theta dz \left(\frac{\partial}{\partial z} r \phi_{rz} \right) \quad (3.41)$$

$$\phi_{rr} = P + \tau_{rr} + \rho V_r^2 \quad (3.42)$$

$$\phi_{r\theta} = \tau_{r\theta} + \rho V_\theta V_r \quad (3.43)$$

$$\phi_{rz} = \tau_{rz} + \rho V_z V_r \quad (3.44)$$

$$0 = -\frac{\partial}{\partial r} \left(P + \tau_{rr} + \rho V_r^2 \right) - \frac{\partial}{\partial \theta} \left(\tau_{r\theta} + \rho V_\theta V_r \right) - \frac{\partial}{\partial z} \left[r \left(\tau_{rz} + \rho V_z V_r \right) \right] \quad (3.45)$$

$$0 = -\frac{\partial P}{\partial r} \times \frac{\partial \tau_{r\theta}}{\partial \theta} - bR\tau_{rz} \frac{\partial \tau_{\theta z}}{\partial \theta} - (a + bz) \frac{\partial \tau_{rz}}{\partial z} \quad (3.46)$$

$$0 = -\frac{\partial P}{\partial r} - \frac{1}{r} \frac{\partial \eta}{\partial \theta} V_\theta - \frac{1}{r} \eta \frac{\partial V_\theta}{\partial \theta} + \frac{\partial \eta}{\partial \theta} \frac{\partial V_\theta}{\partial r} + \eta \frac{\partial}{\partial \theta} \frac{\partial V_\theta}{\partial r} \quad (3.47)$$

$$+ bR\eta \frac{\partial V_z}{\partial r} + (a + bz) \frac{\partial \eta}{\partial z} \frac{\partial V_z}{\partial r} + \eta \frac{\partial}{\partial z} \frac{\partial V_z}{\partial r}$$

Equation (3.47) then is transformed to the helical coordinates as explained below:

$$0 = -\frac{1}{R} \frac{\partial P}{\partial r} + \frac{rs}{M^2} \frac{\partial P}{\partial \theta} + \frac{k_4}{RMr} V_\theta - \frac{1}{Rr} V_z \frac{\partial \eta}{\partial z} + \frac{M}{Rrk_4} V_z - \frac{1}{Rr} V_\theta \frac{\partial \eta}{\partial \theta}$$

$$\frac{1}{Rr} \eta \frac{\partial V_\theta}{\partial \theta} - \frac{M}{k_4} \frac{\partial V_z}{\partial \theta} - \frac{k_4}{M} \frac{\partial V_\theta}{\partial z} + \frac{\partial V_z}{\partial z} + M \frac{\partial \eta}{\partial \theta} + k_4 \frac{\partial \eta}{\partial z} - \frac{1}{RM} \frac{\partial V_\theta}{\partial r} + \frac{1}{Rk_4} \frac{\partial V_z}{\partial r} - \frac{rs}{M^3} \frac{\partial V_\theta}{\partial \theta} + \frac{rs}{M^2 k_4} \frac{\partial V_z}{\partial \theta}$$

$$+ \eta \frac{1}{R} \frac{\partial^2 V_\theta}{\partial \theta \partial r} - \frac{M}{Rk_4} \frac{\partial^2 V_z}{\partial \theta \partial r} + \frac{rs}{M^2} \frac{\partial^2 V_\theta}{\partial \theta^2} - \frac{rs}{Mk_4} \frac{\partial^2 V_z}{\partial \theta^2} - \frac{k_4}{RM} \frac{\partial^2 V_\theta}{\partial z \partial r} + \frac{1}{R} \frac{\partial^2 V_z}{\partial z \partial r} - \frac{rsk_4}{M^3} \frac{\partial^2 V_\theta}{\partial z \partial \theta} + \frac{rs}{M^2} \frac{\partial^2 V_z}{\partial z \partial \theta}$$

$$+ bR\eta \frac{\partial V_z}{\partial r} + \frac{Rrs}{M^2} \frac{\partial V_z}{\partial \theta} + (a + bz) \frac{\partial \eta}{\partial z} \frac{1}{R} \frac{\partial V_z}{\partial r} + \frac{rs}{M^2} \frac{\partial V_z}{\partial \theta} + \eta \frac{1}{R} \frac{\partial^2 V_z}{\partial z \partial r} + \frac{rs}{M^2} \frac{\partial^2 V_z}{\partial z \partial \theta} \quad (3.48)$$

Finally, after the transformation to the helical geometry, we obtain:

$$0 = -\left(\frac{1}{R} \frac{\partial P}{\partial r} + \frac{rs}{M^2} \frac{\partial P}{\partial \theta} \right) + \left(\frac{k_4}{RMr} V_\theta - \frac{1}{Rr} V_z \right) \frac{\partial \eta}{\partial z} + \left(\frac{M}{Rrk_4} V_z - \frac{1}{Rr} V_\theta \right) \frac{\partial \eta}{\partial \theta}$$

$$- \frac{1}{Rr} \eta \left[\frac{\partial V_\theta}{\partial \theta} - \frac{M}{k_4} \frac{\partial V_z}{\partial \theta} - \frac{k_4}{M} \frac{\partial V_\theta}{\partial z} + \frac{\partial V_z}{\partial z} \right] + \left(-M \frac{\partial \eta}{\partial \theta} + k_4 \frac{\partial \eta}{\partial z} \right)$$

$$\left(\frac{-1}{RM} \frac{\partial V_\theta}{\partial r} + \frac{1}{Rk_4} \frac{\partial V_z}{\partial r} - \frac{rs}{M^3} \frac{\partial V_\theta}{\partial \theta} + \frac{rs}{M^2 k_4} \frac{\partial V_z}{\partial \theta} \right)$$

$$+ \eta \left(\frac{1}{R} \frac{\partial^2 V_\theta}{\partial \theta \partial r} - \frac{M}{Rk_4} \frac{\partial^2 V_z}{\partial \theta \partial r} + \frac{rs}{M^2} \frac{\partial^2 V_\theta}{\partial \theta^2} - \frac{rs}{Mk_4} \frac{\partial^2 V_z}{\partial \theta^2} - \frac{k_4}{RM} \frac{\partial^2 V_\theta}{\partial z \partial r} \right)$$

$$\left(+ \frac{1}{R} \frac{\partial^2 V_z}{\partial z \partial r} - \frac{rsk_4}{M^3} \frac{\partial^2 V_\theta}{\partial z \partial \theta} + \frac{rs}{M^2} \frac{\partial^2 V_z}{\partial z \partial \theta} \right)$$

$$+ bR\eta \left(\frac{\partial V_z}{\partial r} + \frac{Rrs}{M^2} \frac{\partial V_z}{\partial \theta} \right) + (a + bz) \left[\frac{\partial \eta}{\partial z} \left(\frac{1}{R} \frac{\partial V_z}{\partial r} + \frac{rs}{M^2} \frac{\partial V_z}{\partial \theta} \right) \right]$$

$$\left[+ \eta \left(\frac{1}{R} \frac{\partial^2 V_z}{\partial z \partial r} + \frac{rs}{M^2} \frac{\partial^2 V_z}{\partial z \partial \theta} \right) \right] \quad (3.49)$$

3.4 Equation of Continuity

A continuity equation is an equation of conservation of mass. This equation states that for an incompressible fluid flowing in a cylinder of varying cross-sections, the mass flow rate is the same everywhere. In view of the principle of conservation of mass, the only way that the mass of the volume V can change is by mass transport across the boundaries of the system. The mass transfer model for a cylindrical coordinate system is given by:

$$\frac{\partial \rho}{\partial t} + \frac{1}{r} \frac{\partial}{\partial r} (\rho r V_r) + \frac{1}{r} \frac{\partial}{\partial \theta} (\rho V_\theta) + \frac{\partial}{\partial z} (\rho V_z) = 0 \quad (3.50)$$

This equation needs to be first expanded and then transformed to a helical coordinate using the transformers developed earlier.

$$0 = \frac{1}{r} \frac{\partial}{\partial \theta} (\rho V_\theta) + \frac{\partial}{\partial z} (\rho V_z) = \frac{1}{r} V_\theta \frac{\partial \rho}{\partial \theta} + \rho \frac{\partial V_\theta}{\partial \theta} + V_z \frac{\partial \rho}{\partial z} + \rho \frac{\partial V_z}{\partial z} \quad (3.51)$$

$$= \frac{1}{r} [V_\theta \frac{\partial \rho}{\partial T} \frac{\partial T}{\partial \theta} + \rho \frac{\partial V_\theta}{\partial \theta}] + V_z \frac{\partial \rho}{\partial T} \frac{\partial T}{\partial z} + \rho \frac{\partial V_z}{\partial z} \quad (3.52)$$

$$= \frac{1}{Rr} \left(\frac{1}{M} V_\theta + \frac{1}{k_4} V_z \right) \frac{\partial \rho}{\partial T} \times \left(-M \frac{\partial T}{\partial \theta} + k_4 \frac{\partial T}{\partial z} \right) \\ + \frac{1}{Rr} \left[\rho \left(-M \frac{\partial}{\partial \theta} + k_4 \frac{\partial}{\partial z} \right) \left(\frac{-1}{M} V_\theta + \frac{1}{k_4} V_z \right) \right] \\ + RV_z \frac{\partial \rho}{\partial T} \frac{1}{R} \frac{\partial T}{\partial z} + \rho \frac{1}{R} \frac{\partial}{\partial z} (RV_z) \quad (3.53)$$

Rearranging Equation (3.53) provides:

$$\Rightarrow \frac{1}{Rr} \frac{\partial \rho}{\partial T} \left(V_\theta \frac{\partial T}{\partial \theta} - \frac{k_4}{M} V_\theta \frac{\partial T}{\partial z} - \frac{M}{k_4} V_z \frac{\partial T}{\partial \theta} + V_z \frac{\partial T}{\partial z} \right) + \frac{\rho}{Rr} \left(\frac{\partial V_\theta}{\partial \theta} - \frac{k_4}{M} \frac{\partial V_\theta}{\partial z} - \frac{M}{k_4} \frac{\partial V_z}{\partial \theta} + \frac{\partial V_z}{\partial z} \right) \\ + V_z \frac{\partial \rho}{\partial T} \frac{\partial T}{\partial z} + \rho \frac{\partial V_z}{\partial z} \quad (3.54)$$

Finally, after the transformation to the helical geometry, we obtain

$$\frac{-M}{Rr} \frac{\partial \rho}{\partial T} \frac{\partial T}{\partial \theta} A_2 + \frac{\rho}{Rr} \frac{\partial V_\theta}{\partial \theta} + V_z \frac{\partial \rho}{\partial T} \frac{\partial T}{\partial z} + \rho \frac{\partial V_z}{\partial z} = 0 \quad (3.55)$$

3.5 Assumptions

The assumptions made in development of the mathematical model are as follows:

- The polymer creates a thin melt layer on the barrel side immediately upon entry.
- The melt film flow is fully developed in the down and cross channel directions.
- The plug perfectly contacts all sides of the screw channel and barrel.
- Shear rate for the concurrent directions of motion and surface is negligible. As a result of this assumption the normal stress terms (τ_{zz} , $\tau_{\theta\theta}$, and τ_{rr}) are zero. In such surface-flow orientation, no stretch or elongation in flow is generated and the shear rate is zero. Thus:

$$\tau_{r\theta} = \tau_{\theta r} = -\eta \left[r \frac{\partial}{\partial r} \left(\frac{V_\theta}{r} \right) + \frac{1}{r} \frac{\partial V_r}{\partial \theta} \right] \quad (3.56)$$

$$\tau_{\theta z} = \tau_{z\theta} = -\eta \left[\frac{1}{r} \frac{\partial V_z}{\partial \theta} + \frac{\partial V_\theta}{\partial z} \right] \quad (3.57)$$

$$\tau_{zr} = \tau_{rz} = -\eta \left[\frac{\partial V_r}{\partial z} + \frac{\partial V_z}{\partial r} \right] \quad (3.58)$$

$$\tau_{rr} = \tau_{\theta\theta} = \tau_{zz} = 0 \Rightarrow \dot{\gamma}_{rr} = \dot{\gamma}_{\theta\theta} = \dot{\gamma}_{zz} = 0 \quad (3.59)$$

- There is no slip on the barrel wall of the extruder and the screw shaft surface.
- The solid bed is an isotropic and homogeneous continuum.
- Melt leakage over the flight tips is negligible.

3.6 Shear Rates

Shear rates can be explained as the velocity gradients, i.e., velocity divided by the gap measured in reciprocal seconds, s^{-1} . For Newtonian fluids, a plot of shear stress versus shear rate at a given temperature is a straight line with a constant slope that is independent of the shear rate and is called viscosity [Carley 53]. For non-Newtonian fluids [Choi 87, Fenner 80, Luyten 91], the slope of the shear stress versus shear rate curve will not be constant as we change the shear rate (Figure 11).

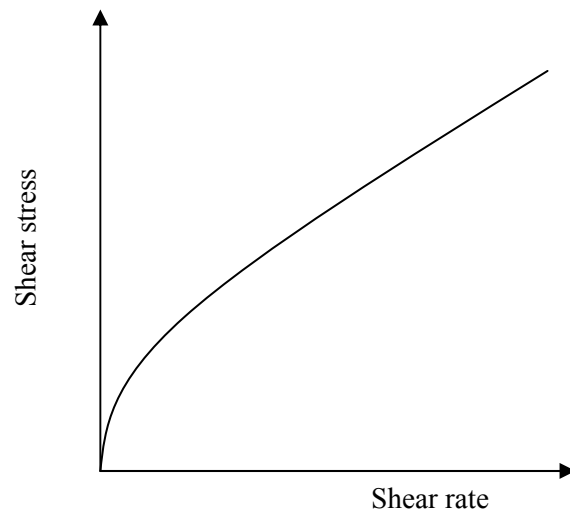


Figure 11: Shear-thinning behavior of polymer melts

As mentioned above, shear rate is equal to the velocity divided by the gap between two surface or layers of polymers (V/h). In injection molding industry, increasing the screw speed increases the rate of shearing, which has direct affect on the final melt temperature and consequently on the melt viscosity [Fleming 04]. As a result, the higher shear rate will ease the flow of polymers in the screw channel but is not necessarily a positive effect since higher shear rate might cause degradation of polymer melt. The velocity and shear rate profiles are anticipated and suggested in Figure 12.

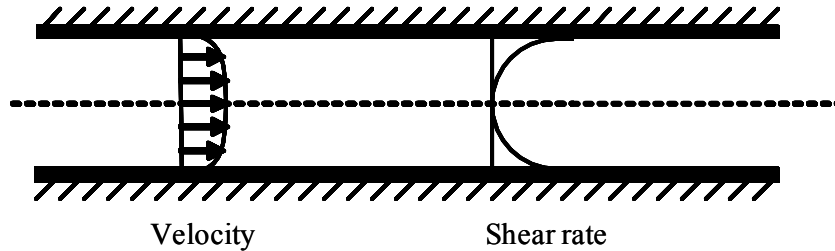


Figure 12: Velocity and shear rate profiles for flow in a tube

As can be seen in Figure 12, for a non-Newtonian flow inside a round tube, the velocity is minimum at the walls and maximum at the plane of symmetry. The shear rate also varies non-linearly from minimum along the central axis to maximum along the wall.

Normally, decreasing the barrel temperature in the feed zone will also increase the shear on the barrel surface and will improve solid conveying. This technique will also help in preventing premature melting in the feed section. When the screw and barrel have equal shear rates in the feeding/metering sections, forward conveying of the polymer will decrease or stop [Rautenbach 82]. In screw extruder channels, the shear rate can usually range from 10 to 10,000 s^{-1} or more.

3.7 Shear Stress

When a molten polymer is sheared, shear stresses are developed. The stress in the polymer melt is proportional to the product of the shear rate and the polymer viscosity at any given melt temperature. In Figure 13 below, a liquid is confined between two flat plates of area A separated by a distance D . When the upper plate is moved in x direction, the liquid is sheared. A constant force is typically required to move the top plate at a velocity relative to the lower plate (F). The shear stress is equal to the viscosity multiplied by the shear rate (measured in units of pressure i.e., MPa or psi).

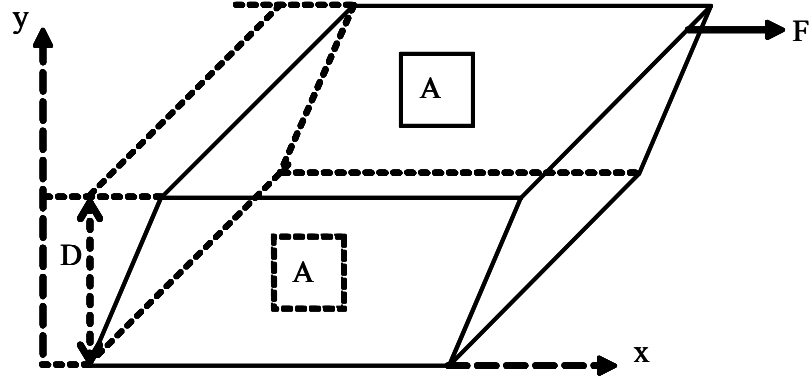


Figure 13: Schematic diagram of shear rate and shear stress surfaces

As explained before, polymer melts tend to develop normal stresses but the stress resulting of concurrent motion of surface and flow are zero. The reason is because the shear would cause extension in helical direction (in a helix) and uneven compression in normal and tangential directions. So, when a polymer melt is forced to flow, it is less compressed in the direction of helix than in the other two normal directions.

The corresponding shear stress to the shear rates in cylindrical coordinates, $(\tau_{rz}, \tau_{r\theta})$, are developed below. Later the final shear stress is then transformed to helical coordinate, utilizing the same velocity profiles.

3.7.1 Shear stress components in cylindrical coordinates:

$$\tau_{rz} = -\eta \left(\frac{\partial V_z}{\partial r} \right) \quad (3.60)$$

$$\tau_{r\theta} = -\eta r \frac{\partial}{\partial r} \left(\frac{V_\theta}{r} \right) = \frac{\eta}{r} V_\theta - \eta \frac{\partial V_\theta}{\partial r} \quad (3.61)$$

3.7.2 Shear stress components in helical coordinates:

$$\tau_{r\theta} = \frac{\eta}{Rr} \frac{1}{M} V_{\theta} + \frac{1}{k_4} V_z \eta \left[\frac{1}{RM} \frac{\partial V_{\theta}}{\partial r} \frac{rs}{M^3} \frac{\partial V_{\theta}}{\partial \theta} + \frac{1}{Rk_4} \frac{\partial V_z}{\partial r} + \frac{rs}{k_4 M^2} \frac{\partial V_z}{\partial \theta} \right] \quad (3.62)$$

$$\tau_{r\theta} = \frac{\eta}{Rr} \frac{1}{M} V_{\theta} + \frac{1}{k_4} V_z \eta \left[\frac{1}{RM} \frac{\partial V_{\theta}}{\partial r} \frac{rs}{M^3} \frac{\partial V_{\theta}}{\partial \theta} + \frac{1}{Rk_4} \frac{\partial V_z}{\partial r} + \frac{rs}{k_4 M^2} \frac{\partial V_z}{\partial \theta} \right] \quad (3.63)$$

All the terms in equations above are already described in previous equations.

3.8 Viscosity Models

Materials must undergo deformation in order to flow inside complex geometry of the extruder or injection units. This deformation is more usefully termed viscosity. It is apparent that the ability to measure the viscosity is beneficial to our expectations from a process performance.

Unlike incompressible fluids, polymer properties changes with variations in the material thermo-physical properties. Polymers are made of long chains, which at rest have multiple orientations that cause its anisotropic behavior. Once the polymer is melted and starts to flow, the chains will line up in the direction of the flow. This alignment reduces the resistance to the shear flow [Fridge 72]. In previous studies [Bigg 73, Broszeit 97, Carley 53, Chiruvella 95, Choi 87, Choo 80, Cunha 94, Dan-Nieh 85, Elbirli 84, Hami 80, Hyun 97, Li 94, Li 96, Lin 98, Maddock 59, Rauwendaal 98, Sokolinkoff 64, Tadmor 67, Zamodits 64] the viscosity of the polymer melt is either assumed to be constant or locally changed by variation in temperature and/or melt velocity. In this work, the viscosity is not constant and depends on temperature of the melt as well as the zero shear rates (and consequently the velocity fields of the polymer melt). Several models are presented to study the shear thinning behavior of polymer melts. In extrusion and injection processes, the Power-law and Cross WLF (Williams- Landel- Ferry) models are very well known and established to characterize the viscosity behavior of polymer melts

[Wrede 72]. The Power-law model characterizes the flow behavior of the material but it only works when shear rates are relatively high. This model does not account for the effect of pressure on the melt and might lead to inaccuracies. While Cross-WLF model is preferred for numerical simulations, power-law models are desirable for quick "back of the envelope" calculations relating material behavior, processing conditions, and geometry. A power law model is shown below:

$$\eta = k \dot{\gamma}^{n-1} \quad (3.64)$$

where k represents the viscosity at a reference shear rate (also known as consistency index), and n is the power law index that is the slope of viscosity curve with respect to shear rate. The Cross-WLF model is more appropriate for injection molding simulations as temperature and pressure sensitivities of the zero-shear viscosity are better represented. The following equations illustrate the Cross-WLF viscosity model [Wrede 72]:

$$\eta = \eta_0 \left(1 + \left(\frac{\eta_0 \dot{\gamma}_T}{\tau} \right)^{(1-n)} \right)^{-1} \quad (3.65)$$

$$\eta_0 = D_1 \exp \left[\frac{-A_1(T - T^*)}{A_2 + (T - T^*)} \right] \quad (3.66)$$

In Equation (3.66) T is temperature (K), T^* is the pressure dependent constant temperature (K) that is equal to $D_2 + D_3 P$ where D_2 and D_3 are plastic material constants.

In Equation (3.65) $\dot{\gamma}_T$ represents the total shear rate (1/sec). τ is the shear thinning transition (Pa), and η_0 is the zero-shear viscosity, which can be represented by the WLF form as follows:

- $T \geq T_g, \quad \eta_0(T, p) = D_1 e^{-A_1(t-T_g) / (A_2 + t-T_g)} \quad (3.67)$

- $T < T_g, \quad \eta_0(T, p) = \infty \quad (3.68)$

In Equations (3.67) and (3.68), T_g is the glass transition temperature of the material and n , τ , D_1 , D_2 , D_3 , A_1 , A_2 are model constants.

Since viscosity is assumed to be influenced by terms such as temperature and zero shear rate, it will have gradients with respect to those variables in the different directions of the helix. These gradients are equal since the viscosity is a scalar quantity rather than being a vector. Nevertheless, based on the nature of this simulation, the viscosity of the polymer melt flow is derived with respect to all three axes and placed in the respective momentum balance equations. The simulation results for the prediction of viscosity for each experiment are illustrated in the results chapter (Chapter 4, section 4.5), which also show that the viscosity at a given temperature is equal in all three helical axes. Figure 14 depicts the influence of shear rate on viscosity under similar processing conditions for a polypropylene resin. The instrument was a Goettfert Rheograph 2003 Capillary Rheometer and the ASTM test method was D 3835-96.

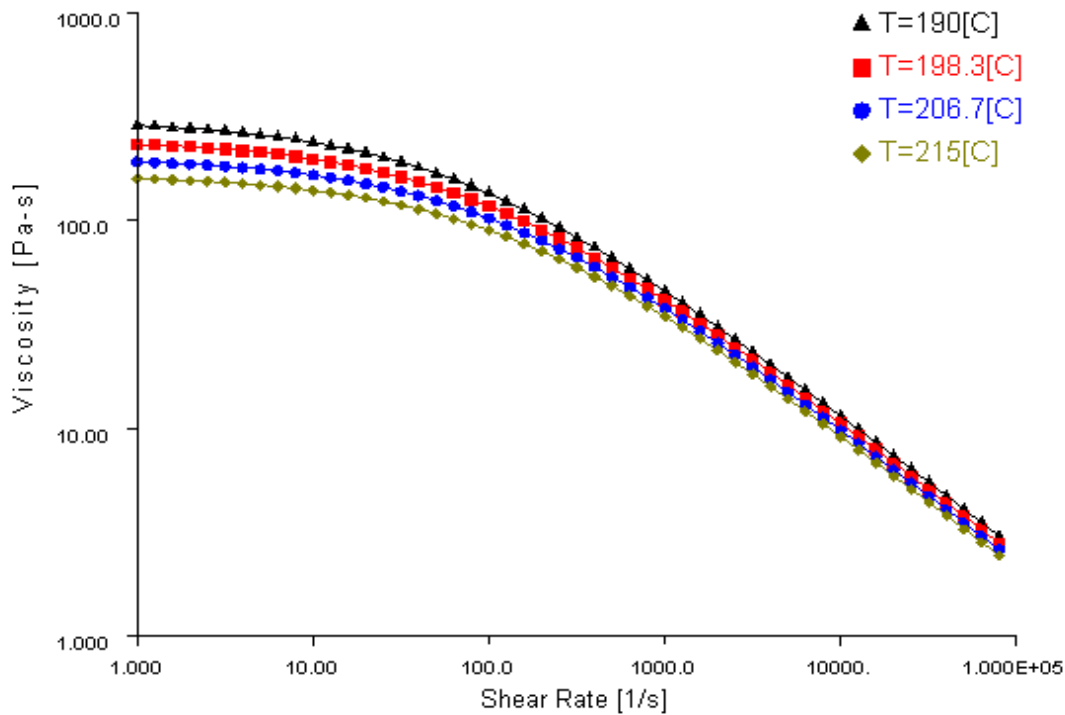


Figure 14: Influence of temperature on viscosity of polypropylene (Source: BP Solvay)

As the melt temperature increases the viscosity lessens. However, for higher shear rate values, increasing the melt temperature does not give the same result. The reason can be explained by the influence of shear rate on the non-Newtonian materials. The viscosity is found to decrease with increasing shear rate for vast majority of polymeric materials. The viscosity appears to be Newtonian at high shear rates so the influence of temperature on the viscosity decreases and increasing the temperature of the resin will not affect the final viscosity.

Below, the viscosity gradient with respect to the radial direction has been developed in details. The derivatives of viscosity with respect to other directions are similar and follow the same approach as below:

$$\eta = \frac{\eta_0}{1 + \left(\frac{\eta_0 \dot{\gamma}_T}{\tau}\right)^{(1-n)}} \Rightarrow \eta = \eta_0 \cdot \frac{1}{S} \Rightarrow \frac{\partial \eta}{\partial r} = \frac{\partial \eta_0}{\partial r} \cdot \frac{1}{S} + \eta_0 \cdot \frac{\partial}{\partial r} \left(\frac{1}{S}\right) \quad (3.69)$$

$$S = 1 + \left(\frac{\eta_0 \dot{\gamma}_T}{\tau}\right)^{1-n} \quad (3.70)$$

$$\Rightarrow \frac{\partial \eta}{\partial r} = \frac{\partial \eta_0}{\partial r} \cdot \frac{\eta}{\eta_0} - \frac{\eta_0}{S^2} \frac{\partial S}{\partial r} = \frac{\partial \eta_0}{\partial r} \cdot \frac{\eta}{\eta_0} - \frac{\eta^2}{\eta_0} \frac{\partial S}{\partial r} \quad (3.71)$$

As shown in the above, expansion of viscosity term with respect to the radial direction has generated more unknown terms (i.e. $\frac{\partial S}{\partial r}$ and $\frac{\partial \eta_0}{\partial r}$), where “S” represents the denominator of the Cross-WLF viscosity equation. For further simplification, these two new terms need to be derived with respect to radial direction and replaced in the main viscosity equation above.

$\frac{\partial S}{\partial r}$:

$$S = 1 + \left(\frac{\eta_0 \dot{\gamma}_T}{\tau}\right)^{1-n} \Rightarrow S_2 = \left(\frac{\eta_0 \dot{\gamma}_T}{\tau}\right)^{1-n} \Rightarrow \frac{\partial S}{\partial r} = \frac{\partial S_2}{\partial r} \Rightarrow \ln S_2 = (1 - n) \ln \left(\frac{\eta_0 \dot{\gamma}_T}{\tau}\right) \quad (3.72)$$

Since:

$$f(x) = \ln(x) \Rightarrow f'(x) = \frac{1}{x} \Rightarrow \frac{1}{S_2} \cdot \frac{\partial S_2}{\partial r} = (1-n) \frac{\tau}{\eta_0 \dot{\gamma}_T} \frac{\partial}{\partial r} \left(\frac{\eta_0 \dot{\gamma}_T}{\tau} \right) = \frac{(1-n)}{\eta_0 \dot{\gamma}_T} \frac{\partial}{\partial r} \left(\eta_0 \dot{\gamma}_T \right) \quad (3.73)$$

$$\Rightarrow \frac{\partial S_2}{\partial r} = \frac{S_2(1-n)}{\eta_0 \dot{\gamma}_T} \frac{\partial}{\partial r} \left(\eta_0 \dot{\gamma}_T \right) = \frac{\partial S}{\partial r} \quad (3.74)$$

$$\frac{\partial \eta_0}{\partial r} :$$

$$\eta_0 = D_1 \exp \left[\frac{-A_1(T - T^*)}{A_2 + (T - T^*)} \right] \quad (3.75)$$

$$\Rightarrow \frac{\partial \eta_0}{\partial r} = \frac{-D_1 A_1 (T - T^*)}{A_2 + (T - T^*)} \exp \left[\frac{-A_1(T - T^*)}{A_2 + (T - T^*)} \right] \cdot \left[\frac{-A_1 \frac{\partial T}{\partial r} (A_2 + (T - T^*)) + A_1 (T - T^*) \cdot \frac{\partial T}{\partial r}}{(A_2 + (T - T^*))^2} \right] \quad (3.76)$$

$$\Rightarrow \frac{\partial \eta_0}{\partial r} = \frac{-\eta_0 A_1 (T - T^*)}{A_2 + (T - T^*)} \cdot \left[\frac{-A_1 A_2}{(A_2 + (T - T^*))^2} \right] \cdot \frac{\partial T}{\partial r} \quad (3.77)$$

Based on the above two derivatives:

$$\frac{\partial \eta_0}{\partial r} = \frac{\eta_0 A^2 A_2 (T - T^*)}{(A_2 + (T - T^*))^3} \cdot \frac{\partial T}{\partial r} \quad (3.78)$$

Consequently, the gradient of the zero shear rates with respect to “ θ ” and “ z ” directions can be written as:

$$\frac{\partial \eta_0}{\partial \theta} = \frac{\eta_0 A^2 A_2 (T - T^*)}{(A_2 + (T - T^*))^3} \cdot \frac{\partial T}{\partial \theta} \quad (3.79)$$

$$\frac{\partial \eta_0}{\partial z} = \frac{\eta_0 A^2 A_2 (T - T^*)}{(A_2 + (T - T^*))^3} \cdot \frac{\partial T}{\partial z} \quad (3.80)$$

After replacing the above terms in Equation (3.71), the viscosity equations in different helical axes can be rewritten as:

$$\frac{\partial \eta}{\partial r} = \frac{\eta_0 A^2 1 A_2 (\Gamma - \Gamma^*)}{A_2 + (\Gamma - \Gamma^*)^3} \cdot \frac{\partial \Gamma}{\partial r} \cdot \frac{\eta}{\eta_0} - \frac{\eta^2}{\eta_0} \frac{A_2 (1 - n)}{\eta_0 \overset{\circ}{\gamma}_T} \left[\eta_0 \cdot \frac{\partial \overset{\circ}{\gamma}_T}{\partial r} + \overset{\circ}{\gamma}_T \left(\frac{\eta_0 A^2 1 A_2 (\Gamma - \Gamma^*)}{A_2 + (\Gamma - \Gamma^*)^3} \cdot \frac{\partial \Gamma}{\partial r} \right) \right] \quad (3.81)$$

$$\frac{\partial \eta}{\partial \theta} = \frac{\eta_0 A^2 1 A_2 (\Gamma - \Gamma^*)}{A_2 + (\Gamma - \Gamma^*)^3} \cdot \frac{\partial \Gamma}{\partial \theta} \cdot \frac{\eta}{\eta_0} - \frac{\eta^2}{\eta_0} \frac{A_2 (1 - n)}{\eta_0 \overset{\circ}{\gamma}_T} \left[\eta_0 \cdot \frac{\partial \overset{\circ}{\gamma}_T}{\partial \theta} + \overset{\circ}{\gamma}_T \left(\frac{\eta_0 A^2 1 A_2 (\Gamma - \Gamma^*)}{A_2 + (\Gamma - \Gamma^*)^3} \cdot \frac{\partial \Gamma}{\partial \theta} \right) \right] \quad (3.82)$$

$$\frac{\partial \eta}{\partial z} = \frac{\eta_0 A^2 1 A_2 (\Gamma - \Gamma^*)}{A_2 + (\Gamma - \Gamma^*)^3} \cdot \frac{\partial \Gamma}{\partial z} \cdot \frac{\eta}{\eta_0} - \frac{\eta^2}{\eta_0} \frac{A_2 (1 - n)}{\eta_0 \overset{\circ}{\gamma}_T} \left[\eta_0 \cdot \frac{\partial \overset{\circ}{\gamma}_T}{\partial z} + \overset{\circ}{\gamma}_T \left(\frac{\eta_0 A^2 1 A_2 (\Gamma - \Gamma^*)}{A_2 + (\Gamma - \Gamma^*)^3} \cdot \frac{\partial \Gamma}{\partial z} \right) \right] \quad (3.83)$$

As can be seen above, further expansion of viscosity gradients with respect to all three axes has led to even more unknown terms (i.e. $\frac{\partial \overset{\circ}{\gamma}_T}{\partial r}$, $\frac{\partial \overset{\circ}{\gamma}_T}{\partial \theta}$, $\frac{\partial \overset{\circ}{\gamma}_T}{\partial z}$). These terms are total shear rates with respect to different axes and need to be derived from the total shear rate expression. In cylindrical coordinate the total shear rate expression is presented by:

$$\overset{\circ}{\gamma}_T = \sqrt{\left[r \frac{d}{dr} \left(\frac{V_\theta}{r} \right) \right]^2 + \left(\frac{dV_z}{dr} \right)^2} \quad (3.84)$$

By applying the velocity and derivative transformers in the above cylindrical equation, the total shear rate in helical coordinate can be expressed as:

$$\begin{aligned} \frac{d}{dr} \left(\frac{V_\theta}{r} \right) &= \frac{r \frac{\partial V_\theta}{\partial r} - V_\theta}{r^2} \Rightarrow r \frac{d}{dr} \left(\frac{V_\theta}{r} \right) = \frac{\partial V_\theta}{\partial r} - \frac{1}{r} V_\theta = \left(\frac{1}{R} \frac{\partial}{\partial r} + \frac{rs}{RM^2} \frac{\partial}{\partial \theta} \right) \left(-\frac{1}{M} V_\theta \right) - \frac{1}{Rr} \left(-\frac{1}{M} V_\theta \right) \\ &= \left(-\frac{1}{RM} \frac{\partial V_\theta}{\partial r} - \frac{rs}{RM^3} \frac{\partial V_\theta}{\partial \theta} \right) + \frac{1}{RrM} V_\theta \end{aligned} \quad (3.85)$$

$$\frac{dV_z}{dr} = \left(\frac{1}{R} \frac{\partial}{\partial r} + \frac{rs}{RM^2} \frac{\partial}{\partial \theta} \right) R V_z = \frac{\partial V_z}{\partial r} + \frac{rs}{M^2} \frac{\partial V_z}{\partial \theta}$$

$$\overset{\circ}{\gamma}_T = \sqrt{\left[\left(-\frac{1}{RM} \frac{\partial V_\theta}{\partial r} - \frac{rs}{RM^3} \frac{\partial V_\theta}{\partial \theta} + \frac{1}{RrM} V_\theta \right) \right]^2 + \left[\frac{\partial V_z}{\partial r} + \frac{rs}{M^2} \frac{\partial V_z}{\partial \theta} \right]^2} \quad (3.86)$$

$$\frac{\partial \overset{\circ}{\gamma}_T}{\partial r} = \frac{1}{\overset{\circ}{\gamma}_T} \left(\overset{\circ}{\gamma}_{T1} \left[\frac{-1}{RM} \frac{\partial^2 V_\theta}{\partial r^2} - \frac{s}{RM^3} \frac{\partial V_\theta}{\partial \theta} - \frac{rs}{RM^3} \frac{\partial^2 V_\theta}{\partial r \partial \theta} - \frac{1}{RM^2} V_\theta + \frac{1}{RrM} \frac{\partial V_\theta}{\partial r} \right] + \overset{\circ}{\gamma}_{T2} \left[\frac{\partial^2 V_z}{\partial r^2} + \frac{s}{M^2} \frac{\partial V_z}{\partial \theta} + \frac{rs}{M^2} \frac{\partial^2 V_z}{\partial r \partial \theta} \right] \right) \quad (3.87)$$

$$\frac{\partial \overset{\circ}{\gamma}_T}{\partial \theta} = \frac{1}{\overset{\circ}{\gamma}_T} \left(\overset{\circ}{\gamma}_{T1} \left[\frac{-1}{RM} \frac{\partial^2 V_\theta}{\partial r \partial \theta} - \frac{rs}{RM^3} \frac{\partial^2 V_\theta}{\partial \theta^2} + \frac{1}{RrM} \frac{\partial V_\theta}{\partial \theta} \right] + \overset{\circ}{\gamma}_{T2} \left[\frac{\partial^2 V_z}{\partial r \partial \theta} + \frac{rs}{M^2} \frac{\partial^2 V_z}{\partial \theta^2} \right] \right) \quad (3.88)$$

$$\frac{\partial \overset{\circ}{\gamma}_T}{\partial z} = \frac{1}{\overset{\circ}{\gamma}_T} \left(\overset{\circ}{\gamma}_{T1} \left[\frac{-1}{RM} \frac{\partial^2 V_\theta}{\partial r \partial z} - \frac{rs}{RM^3} \frac{\partial^2 V_\theta}{\partial \theta \partial z} + \frac{1}{RrM} \frac{\partial V_\theta}{\partial z} \right] + \overset{\circ}{\gamma}_{T2} \left[\frac{\partial^2 V_z}{\partial r \partial z} + \frac{rs}{M^2} \frac{\partial^2 V_z}{\partial \theta \partial z} \right] \right) \quad (3.89)$$

3.9 Flow Rate

The plastic melt flows in three different axes of a helical system: helical (down channel), normal (radial), and tangential (cross channel).

Different theoretical equations exist for calculating the flow rate of polymer melt in an extrusion or injection molding process. One of the most common expressions is shown in Equation (3.90) [Rauwendaal 86]. The flow rate in this equation depends on drag flow [first part of the right hand side in Equation (3.90)] and pressure flow [second section of Equation (3.90)].

$$Q = W_\theta \pi N R_b^3 \sin \varphi \cos \varphi F(\beta) - \frac{W_\theta \sin^2 \varphi R_b^4}{16\eta} \left[1 - \beta^4 + \frac{(1 - \beta^2)^2}{\ln \beta} \right] \frac{dP}{dz} \quad (3.90)$$

where:

W_θ , N , $F(\beta)$, φ represent the angular channel width in radians, screw peripheral speed in rpm, ratio of the radii R_s/R_b , and helix angle, respectively. The term $\frac{dP}{dz}$ represents the pressure gradient (Pa).

As explained before, calculating the flow rate (or mainly known as throughput) requires the cycle as an input. That is why it is more desired to estimate the recovery rate of a

single screw injection unit that is cycle time-free, using the dimensions of the screw in its metering zone. This has been further explained in section 4.3, where the recovery rate for different processing conditions is simulated.

3.10 Energy Balance-Helical

The equation for energy in extrusion process is derived from the basic conservation principles. The thermal energy can be supplied to the material undergoing processing, through different thermal boundary conditions imposed. In addition to conventional heat transfer phenomena, viscous dissipation and work done by the moving fluid also act as a thermal source. Due to the poor thermal conductivity of polymer melt, the heating elements are not the major contributor to the melting process. The main supplier of heat is the rotation of the screw inside the extruder that smears the molten polymer between the solid bed and the barrel wall (work-induced heat), generating shear and mechanical heat. The viscous dissipation, $(\eta \cdot \tau)$, represents the irreversible part of the energy transfer due to the shear stress. Therefore, viscous dissipation gives rise to a thermal source in the flow and is always positive. Melt viscosity is also deeply dependent on the viscous dissipation [Fridge 72, Sokolinkoff 64] and solutions without considering this reliance will not adequately represent the thermal phenomenon in extrusion process. In this work, the energy balance equation in a helical coordinate is established to describe the temperature profile along the length of the extruder. This approach will enable the calculation of screw length required for completion of polymer melting for a specific set of processing conditions and screw geometry. This length is an important parameter for understanding the performance of a particular screw design and configuration. It can also be used to study how the processing conditions and other parameters will affect this length. Design of a screw plays a very important role in the energy generation and melting of a specific resin. Apart from its mechanical strength, a successful screw design is one in which the shear and heat generated from the screw elements are sufficient to ensure that the entire polymer is converted to a molten state before the end of the screw. The melt temperature is not uniform inside the screw channel and changes in all axes because of dissipative heat generation and heat conduction with the barrel and screw within the melt.

viscous dissipation (q_{DISS}). In the following, the energy balance in a cylindrical coordinate for a steady-state extrusion operation is developed:

$$\begin{aligned}
0 = & \left[(drdz) V_{\theta} \rho C_p T \right]_{\theta} - \left[(drdz) V_{\theta} \rho C_p T \right]_{\theta+d\theta} + \left[(rdrd\theta) V_z \rho C_p T \right]_z \\
& - \left[(rdrd\theta) V_z \rho C_p T \right]_{z+dz} + \left[(dzd\theta) V_r \rho C_p T \right]_r - \left[(dzd\theta) V_r \rho C_p T \right]_{r+dr} \\
& + \left[-K \frac{\partial T}{\partial r} (rd\theta dz) \right]_r - \left[-K \frac{\partial T}{\partial r} (rd\theta dz) \right]_{r+dr} + \left[-K \frac{\partial T}{\partial z} (rd\theta dr) \right]_z \\
& - \left[-K \frac{\partial T}{\partial z} (rd\theta dr) \right]_{z+dz} + \left[-K \frac{\partial T}{\partial \theta} (dzdr) \right]_{\theta} - \left[-K \frac{\partial T}{\partial \theta} (dzdr) \right]_{\theta+d\theta} \\
& + \left[\pi_{\theta} \cdot V_{\theta} \right]_{\theta} - \left[\pi_{\theta} \cdot V_{\theta} \right]_{\theta+d\theta} + \left[\pi_z \cdot V_z \right]_z - \left[\pi_z \cdot V_z \right]_{z+dz} \\
& + \left[\pi_r \cdot V_r \right]_r - \left[\pi_r \cdot V_r \right]_{r+dr} + q_{DISS}
\end{aligned} \tag{3.91}$$

where ρ , C_p , and K are density, volumetric heat capacity, and thermal conductivity of polymer melt respectively.

In Equation (3.91) the accumulation term is zero, [left hand side of the equation], due to the steady-state operation. The first six terms on the right hand side of the Equation (3.91) represent the heat flux by conduction followed by the conductive heat in all the helical axes, the work done by the fluid and finally the irreversible heat of dissipation

Due to the complexity of the energy equation and for the ease of visualization, the above terms are studied and expanded separately. Later they are transformed to helical geometry using the transformers developed earlier and then put back together to form the final energy balance equation in helical coordinates.

First the heat flux by conduction in angular direction is expanded and then transformed to helical coordinates as follow:

$$1. \left[(drdz) V_{\theta} \rho C_p T \right]_{\theta} - \left[(drdz) V_{\theta} \rho C_p T \right]_{\theta+d\theta} = - \frac{\partial}{\partial \theta} \left[V_{\theta} \rho C_p T \right] drdzd\theta \tag{3.92}$$

$$= - \left[\rho C_p T \frac{\partial V_\theta}{\partial \theta} + C_p T V_\theta \frac{\partial \rho}{\partial T} \frac{\partial T}{\partial \theta} + \rho T V_\theta \frac{\partial C_p}{\partial T} \frac{\partial T}{\partial \theta} + \rho C_p V_\theta \frac{\partial T}{\partial \theta} \right] dr dz d\theta \quad (3.93)$$

$$= - \left[\begin{aligned} & \rho C_p T \left(-M \frac{\partial}{\partial \theta} + k_4 \frac{\partial}{\partial z} \right) \left(-\frac{1}{M} V_\theta^h + \frac{1}{k_4} V_z^h \right) \\ & + C_p T \frac{\partial \rho}{\partial T} \left(-\frac{1}{M} V_\theta^h + \frac{1}{k_4} V_z^h \right) \left(-M \frac{\partial T}{\partial \theta} + k_4 \frac{\partial T}{\partial z} \right) \\ & + \rho T \frac{\partial C_p}{\partial T} \left(-\frac{1}{M} V_\theta^h + \frac{1}{k_4} V_z^h \right) \left(-M \frac{\partial T}{\partial \theta} + k_4 \frac{\partial T}{\partial z} \right) \\ & + \rho C_p \left(-\frac{1}{M} V_\theta^h + \frac{1}{k_4} V_z^h \right) \left(-M \frac{\partial T}{\partial \theta} + k_4 \frac{\partial T}{\partial z} \right) \end{aligned} \right] dr dz d\theta \quad (3.94)$$

$$= - \left[\begin{aligned} & \rho C_p T \left(\frac{\partial V_\theta^h}{\partial \theta^h} - \frac{M}{k_4} \frac{\partial V_z^h}{\partial \theta^h} - \frac{k_4}{M} \frac{\partial V_\theta^h}{\partial z^h} + \frac{\partial V_z^h}{\partial z^h} \right) \\ & + \left(C_p T \frac{\partial \rho}{\partial T} + \rho T \frac{\partial C_p}{\partial T} + \rho C_p \right) \\ & \cdot \left(V_\theta^h \frac{\partial T}{\partial \theta} - \frac{k_4}{M} V_\theta^h \frac{\partial T}{\partial z} - \frac{M}{k_4} V_z^h \frac{\partial T}{\partial \theta} + V_z^h \frac{\partial T}{\partial z} \right) \end{aligned} \right] dr dz d\theta \quad (3.95)$$

In the following the heat flux by conduction in axial direction of the screw is expanded and then transformed to helical coordinates. As can be seen, the thermo-physical properties vary along the screw direction as well as by temperature:

$$2. [(r dr d\theta) V_z \rho C_p T]_z - [(r dr d\theta) V_z \rho C_p T]_{z+dz} = -r \frac{\partial}{\partial z} [V_z \rho C_p T] dr d\theta dz \quad (3.96)$$

$$= -r \left[\rho C_p T \frac{\partial V_z}{\partial z} + C_p T V_z \frac{\partial \rho}{\partial z} + \rho T V_z \frac{\partial C_p}{\partial z} + \rho C_p V_z \frac{\partial T}{\partial z} \right] dr d\theta dz \quad (3.97)$$

$$= -r \left[\rho C_p T \frac{\partial V_z}{\partial z} + C_p T V_z \frac{\partial \rho}{\partial T} \frac{\partial T}{\partial z} + \rho T V_z \frac{\partial C_p}{\partial T} \frac{\partial T}{\partial z} + \rho C_p V_z \frac{\partial T}{\partial z} \right] dr d\theta dz \quad (3.98)$$

$$= -r \left[\begin{aligned} & \rho C_p T \left(\frac{1}{R} \frac{\partial}{\partial z^h} \right) (R V_z^h) + C_p T \frac{\partial \rho}{\partial T} \left(\frac{1}{R} \frac{\partial T}{\partial z^h} \right) (R V_z^h) \\ & + \rho T \frac{\partial C_p}{\partial T} \left(\frac{1}{R} \frac{\partial T}{\partial z^h} \right) (R V_z^h) + \rho C_p \left(\frac{1}{R} \frac{\partial T}{\partial z^h} \right) (R V_z^h) \end{aligned} \right] dr d\theta dz \quad (3.99)$$

$$= - \left[Rr \rho C_p T \frac{\partial V_z^h}{\partial z^h} + \left(C_p T \frac{\partial \rho}{\partial T} + \rho T \frac{\partial C_p}{\partial T} + \rho C_p \right) Rr V_z^h \frac{\partial T}{\partial z^h} \right] dr d\theta dz \quad (3.100)$$

The last term of the heat flux conduction is along the radial direction of the screw, which is first expanded and then transformed to helical coordinates as the other two heat flux terms:

$$3. \frac{\partial}{\partial t} (\rho V_z) dr d\theta dz = -dr d\theta dz \left(\frac{\partial}{\partial r} \phi_{rr} \right) - dr d\theta dz \left(\frac{\partial}{\partial \theta} \phi_{r\theta} \right) - dr d\theta dz \left(\frac{\partial}{\partial z} r \phi_{rz} \right) \quad (3.101)$$

$$\phi_{rr} = P + \tau_{rr} + \rho V_r^2 \quad (3.102)$$

$$\phi_{r\theta} = \tau_{r\theta} + \rho V_\theta V_r \quad (3.103)$$

$$\phi_{rz} = \tau_{rz} + \rho V_z V_r \quad (3.104)$$

$$0 = - \frac{\partial}{\partial r} (P + \tau_{rr} + \rho V_r^2) - \frac{\partial}{\partial \theta} (\tau_{r\theta} + \rho V_\theta V_r) - \frac{\partial}{\partial z} [r(\tau_{rz} + \rho V_z V_r)] \quad (3.105)$$

$$0 = - \frac{\partial P}{\partial r} - \frac{\partial \tau_{r\theta}}{\partial \theta} - bR \tau_{rz} \frac{\partial \tau_{\theta z}}{\partial \theta} - (a + bz) \left[\frac{\partial \tau_{rz}}{\partial z} \right] \quad (3.106)$$

$$0 = - \frac{\partial P}{\partial r} - \frac{1}{r} \frac{\partial \eta}{\partial \theta} V_\theta - \frac{1}{r} \eta \frac{\partial V_\theta}{\partial \theta} + \frac{\partial \eta}{\partial \theta} \frac{\partial V_\theta}{\partial r} + \eta \frac{\partial}{\partial \theta} \left(\frac{\partial V_\theta}{\partial r} \right) + bR \eta \frac{\partial V_z}{\partial r} \quad (3.107)$$

$$+ (a + bz) \left[\frac{\partial \eta}{\partial z} \frac{\partial V_z}{\partial r} + \eta \frac{\partial}{\partial z} \left(\frac{\partial V_z}{\partial r} \right) \right]$$

$$0 = - \left(\frac{1}{R} \frac{\partial P}{\partial r} + \frac{rs}{M^2} \frac{\partial P}{\partial \theta} \right) + \left(\frac{k_4}{RMr} V_\theta - \frac{1}{Rr} V_z \right) \frac{\partial \eta}{\partial z} +$$

$$\left(\frac{M}{Rrk_4} V_z - \frac{1}{Rr} V_\theta \right) \frac{\partial \eta}{\partial \theta}$$

$$- \frac{1}{Rr} \eta \left[\frac{\partial V_\theta}{\partial \theta} - \frac{M}{k_4} \frac{\partial V_z}{\partial \theta} - \frac{k_4}{M} \frac{\partial V_\theta}{\partial z} + \frac{\partial V_z}{\partial z} \right] + \left(-M \frac{\partial \eta}{\partial \theta} + k_4 \frac{\partial \eta}{\partial z} \right)$$

$$\left(\frac{-1}{RM} \frac{\partial V_\theta}{\partial r} + \frac{1}{Rk_4} \frac{\partial V_z}{\partial r} - \frac{rs}{M^3} \frac{\partial V_\theta}{\partial \theta} + \frac{rs}{M^2 k_4} \frac{\partial V_z}{\partial \theta} \right)$$

$$+ \eta \left(\frac{1}{R} \frac{\partial^2 V_\theta}{\partial \theta \partial r} - \frac{M}{Rk_4} \frac{\partial^2 V_z}{\partial \theta \partial r} + \frac{rs}{M^2} \frac{\partial^2 V_\theta}{\partial \theta^2} - \frac{rs}{Mk_4} \frac{\partial^2 V_z}{\partial \theta^2} - \frac{k_4}{RM} \frac{\partial^2 V_\theta}{\partial z \partial r} \right.$$

$$\left. + \frac{1}{R} \frac{\partial^2 V_z}{\partial z \partial r} - \frac{rsk_4}{M^3} \frac{\partial^2 V_\theta}{\partial z \partial \theta} + \frac{rs}{M^2} \frac{\partial^2 V_z}{\partial z \partial \theta} \right)$$

$$+ bR \eta \left(\frac{\partial V_z}{\partial r} + \frac{Rrs}{M^2} \frac{\partial V_z}{\partial \theta} \right) + (a + bz) \left[\frac{\partial \eta}{\partial z} \left(\frac{1}{R} \frac{\partial V_z}{\partial r} + \frac{rs}{M^2} \frac{\partial V_z}{\partial \theta} \right) \right.$$

$$\left. + \eta \left(\frac{1}{R} \frac{\partial^2 V_z}{\partial z \partial r} + \frac{rs}{M^2} \frac{\partial^2 V_z}{\partial z \partial \theta} \right) \right] \quad (3.108)$$

Sections 4, 5, and 6 below represent the conductive heat in radial, axial, and angular directions of a screw with cylindrical coordinates respectively. They are also expanded separately and then transformed to helical coordinates:

$$\begin{aligned}
& \left[-K \frac{\partial T}{\partial r} (rd\theta dz) \right]_r - \left[-K \frac{\partial T}{\partial r} (rd\theta dz) \right]_{r+dr} \\
4. &= -\frac{\partial}{\partial r} \left[-K \frac{\partial T}{\partial r} rd\theta dz \right] dr = \frac{\partial}{\partial r} \left[Kr \frac{\partial T}{\partial r} \right] d\theta dz dr \\
&= Rr \frac{\partial K}{\partial T} \left(\frac{\partial T}{\partial r} \right)^2 + K \frac{\partial T}{\partial r} + KRr \frac{\partial^2 T}{\partial r^2}
\end{aligned} \tag{3.109}$$

$$= \left[\begin{aligned} & Rr \frac{\partial K}{\partial T} \left[\frac{1}{R^2} \left(\frac{\partial T}{\partial r} \right)^2 + \frac{2r^h s}{RM^2} \frac{\partial T}{\partial r} \frac{\partial T}{\partial \theta} + \frac{(r^h s)^2}{M^4} \left(\frac{\partial T}{\partial \theta} \right)^2 \right] + \frac{K}{R} \frac{\partial T}{\partial r} + \frac{Krs}{M^2} \frac{\partial T}{\partial \theta} + \\ & KRr \left(\frac{1}{R^2} \frac{\partial^2 T}{\partial r^2} + \frac{2r^h s}{RM^2} \frac{\partial^2 T}{\partial r \partial \theta} + \frac{(r^h s)^2}{M^4} \frac{\partial^2 T}{\partial \theta^2} \right) \end{aligned} \right] dr d\theta dz \tag{3.110}$$

$$\begin{aligned}
5. & \left[-K \frac{\partial T}{\partial z} (rd\theta dr) \right]_z - \left[-K \frac{\partial T}{\partial z} (rd\theta dr) \right]_{z+dz} = -\frac{\partial}{\partial z} \left(-K \frac{\partial T}{\partial z} rd\theta dr \right) dz = \\ & \frac{\partial}{\partial z} \left(K \frac{\partial T}{\partial z} \right) rd\theta dr dz = r \frac{\partial K}{\partial T} \left(\frac{\partial T}{\partial z} \right)^2 + rK \frac{\partial^2 T}{\partial z^2}
\end{aligned} \tag{3.111}$$

$$= \left[\frac{r}{R} \frac{\partial K}{\partial T} \left(\frac{\partial T}{\partial z} \right)^2 + \frac{Kr}{R} \frac{\partial^2 T}{\partial z^2} \right] dr d\theta dz \tag{3.112}$$

$$\begin{aligned}
6. & \left[-K \frac{\partial T}{\partial \theta} (dzdr) \right]_\theta - \left[-K \frac{\partial T}{\partial \theta} (dzdr) \right]_{\theta+d\theta} = -\frac{\partial}{\partial \theta} \left(-K \frac{\partial T}{\partial \theta} dzdr \right) d\theta = \\ & \frac{\partial}{\partial \theta} \left(K \frac{\partial T}{\partial \theta} \right) dzdr = \left[\frac{\partial K}{\partial T} \left(\frac{\partial T}{\partial \theta} \right)^2 + K \frac{\partial^2 T}{\partial \theta^2} \right] dzdr
\end{aligned} \tag{3.113}$$

$$= \left[\begin{aligned} & \frac{\partial K}{\partial T} \left(M^2 \left(\frac{\partial T}{\partial \theta} \right)^2 - 2Mk_4 \frac{\partial T}{\partial z} \frac{\partial T}{\partial \theta} + k_4^2 \left(\frac{\partial T}{\partial z} \right)^2 \right) + \\ & K \left(M^2 \frac{\partial^2 T}{\partial \theta^2} - 2Mk_4 \frac{\partial^2 T}{\partial z \partial \theta} + k_4^2 \frac{\partial^2 T}{\partial z^2} \right) \end{aligned} \right] d\theta dz dr \tag{3.114}$$

Sections 7, 8, and 9 below represent the work done by the fluid in radial, axial, and angular directions of a screw with cylindrical coordinates respectively. They are also expanded separately and then transformed to helical coordinates:

$$7. [\pi_\theta \cdot V_\theta]_0 - [\pi_\theta \cdot V_\theta]_{\theta+d\theta} = -\frac{\partial}{\partial \theta} [\tau_{r\theta} V_\theta] dr d\theta dz = -\left[\frac{\partial \tau_{r\theta}}{\partial \theta} V_\theta + \tau_{r\theta} \frac{\partial V_\theta}{\partial \theta} \right] dr d\theta dz \quad (3.115)$$

$$\text{Because : } \tau_{r\theta} = \frac{\eta}{r} V_\theta - \eta \frac{\partial V_\theta}{\partial r} \quad (3.116)$$

$$-\left[\frac{\partial \tau_{r\theta}}{\partial \theta} V_\theta + \tau_{r\theta} \frac{\partial V_\theta}{\partial \theta} \right] dr d\theta dz = -\left[\begin{aligned} &\frac{\partial}{\partial \theta} \left(\frac{\eta}{r} V_\theta - \eta \frac{\partial V_\theta}{\partial r} \right) V_\theta \\ &+ \left(\frac{\eta}{r} V_\theta - \eta \frac{\partial V_\theta}{\partial r} \right) \frac{\partial V_\theta}{\partial \theta} \end{aligned} \right] dr d\theta dz \quad (3.117)$$

$$8. [\pi_\theta \cdot V_\theta]_0 - [\pi_\theta \cdot V_\theta]_{\theta+d\theta} = -\frac{\partial}{\partial \theta} [\tau_{r\theta} V_\theta] dr d\theta dz = -\left[\frac{\partial \tau_{r\theta}}{\partial \theta} V_\theta + \tau_{r\theta} \frac{\partial V_\theta}{\partial \theta} \right] dr d\theta dz \quad (3.118)$$

$$\text{Because : } \tau_{r\theta} = \frac{\eta}{r} V_\theta - \eta \frac{\partial V_\theta}{\partial r} \quad (3.119)$$

$$-\left[\frac{\partial \tau_{r\theta}}{\partial \theta} V_\theta + \tau_{r\theta} \frac{\partial V_\theta}{\partial \theta} \right] dr d\theta dz = -\left[\begin{aligned} &\frac{\partial}{\partial \theta} \left(\frac{\eta}{r} V_\theta - \eta \frac{\partial V_\theta}{\partial r} \right) V_\theta \\ &+ \left(\frac{\eta}{r} V_\theta - \eta \frac{\partial V_\theta}{\partial r} \right) \frac{\partial V_\theta}{\partial \theta} \end{aligned} \right] dr d\theta dz \quad (3.120)$$

$$\begin{aligned}
& \left. \begin{aligned}
& \frac{1}{Rr} \frac{\partial \eta}{\partial \theta} \left(\frac{-1}{M} V_\theta^2 - \frac{M}{k_4^2} V_z^2 + \frac{2}{k_4} V_\theta V_z \right) \\
& + \frac{\partial V_\theta}{\partial \theta} \left(\frac{-\eta V_\theta}{RrM} + \frac{\eta V_z}{Rrk_4} + \frac{rs}{M^3} V_\theta \frac{\partial \eta}{\partial \theta} - \frac{rsk_4}{M^4} V_\theta \frac{\partial \eta}{\partial z} - \frac{rs}{k_4 M^2} V_z \frac{\partial \eta}{\partial z} \right) \\
& + \frac{rs}{M^3} V_z \frac{\partial \eta}{\partial z} + \frac{\eta}{Rr} \left(\frac{-1}{M} V_\theta + \frac{1}{k_4} V_z \right) \\
& + \frac{1}{Rr} \frac{\partial \eta}{\partial z} \left(\frac{k_4}{M^2} V_\theta^2 + \frac{1}{k_4} V_z^2 - \frac{2}{M} V_\theta V_z \right) \\
& + \frac{\partial V_z}{\partial \theta} \left(\frac{\eta V_\theta}{Rrk_4} - \frac{\eta MV_z}{Rrk_4^2} - \frac{rs}{k_4 M^2} V_\theta \frac{\partial \eta}{\partial \theta} \right. \\
& \left. + \frac{rs}{M^3} V_\theta \frac{\partial \eta}{\partial z} + \frac{rs}{k_4^2 M} V_z \frac{\partial \eta}{\partial \theta} \right. \\
& \left. - \frac{rs}{k_4 M^2} V_z \frac{\partial \eta}{\partial z} - \frac{\eta M}{Rrk_4} \left(\frac{-1}{M} V_\theta + \frac{1}{k_4} V_z \right) \right) \\
& + \frac{\partial V_\theta}{\partial z} \left(\frac{\eta k_4}{RrM^2} V_\theta - \frac{\eta}{RrM} V_z - \frac{\eta k_4}{RrM} \left(\frac{-1}{M} V_\theta + \frac{1}{k_4} V_z \right) \right) \\
& + \frac{\partial V_z}{\partial z} \left(\frac{-\eta}{RrM} V_\theta + \frac{\eta}{Rrk_4} V_z + \frac{\eta}{Rr} \left(\frac{-1}{M} V_\theta + \frac{1}{k_4} V_z \right) \right) \\
& + \frac{\partial V_\theta}{\partial r} \left(\frac{1}{RM} V_\theta \frac{\partial \eta}{\partial \theta} - \frac{k_4}{RM^2} V_\theta \frac{\partial \eta}{\partial z} - \frac{1}{Rk_4} V_z \frac{\partial \eta}{\partial \theta} + \frac{1}{RM} V_z \frac{\partial \eta}{\partial z} \right) \\
& + \frac{\partial V_z}{\partial r} \left(\frac{-1}{Rk_4} V_\theta \frac{\partial \eta}{\partial \theta} + \frac{1}{RM} V_\theta \frac{\partial \eta}{\partial z} + \frac{M}{Rk_4^2} V_z \frac{\partial \eta}{\partial \theta} - \frac{1}{Rk_4} V_z \frac{\partial \eta}{\partial z} \right) \\
& + \frac{\partial^2 V_\theta}{\partial r \partial \theta} \left(\frac{-\eta}{R} \left(\frac{-1}{M} V_\theta + \frac{1}{k_4} V_z \right) + \frac{\eta}{RM} \right) \\
& + \frac{\partial^2 V_z}{\partial r \partial \theta} \left(\frac{\eta M}{Rk_4} \left(\frac{-1}{M} V_\theta + \frac{1}{k_4} V_z \right) + \frac{\eta}{Rk_4^2} \right) \\
& - \eta \left(\frac{-1}{M} V_\theta + \frac{1}{k_4} V_z \right) \left(\frac{rs}{M^2} \frac{\partial^2 V_\theta}{\partial \theta^2} - \frac{rs}{k_4 M} \frac{\partial^2 V_z}{\partial \theta^2} - \frac{k_4}{RM} \frac{\partial^2 V_\theta}{\partial r \partial z} \right) \\
& + \frac{\partial^2 V_z}{\partial r \partial z} \left(\frac{-\eta}{R} \left(\frac{-1}{M} V_\theta + \frac{1}{k_4} V_z \right) - \frac{\eta}{Rk_4} \right) \\
& + \frac{\partial^2 V_\theta}{\partial z \partial \theta} \left(\frac{\eta rsk_4}{M^3} \left(\frac{-1}{M} V_\theta + \frac{1}{k_4} V_z \right) - \frac{\eta rsk_4}{M^4} \right) \\
& + \frac{\partial^2 V_z}{\partial z \partial \theta} \left(\frac{-\eta rs}{M^2} \left(\frac{-1}{M} V_\theta + \frac{1}{k_4} V_z \right) - \frac{\eta rs}{k_4 M^2} \right) \\
& + \frac{\partial V_\theta}{\partial r} \left(\frac{-\eta}{Rk_4} \frac{\partial V_z}{\partial \theta} - \frac{\eta k_4}{RM^2} \frac{\partial V_\theta}{\partial z} + \frac{\eta}{RM} \frac{\partial V_z}{\partial z} \right) + \\
& \frac{\partial V_z}{\partial r} \left(\frac{-\eta}{Rk_4} \frac{\partial V_\theta}{\partial \theta} + \frac{\eta}{RM} \frac{\partial V_\theta}{\partial z} \right) + \frac{\eta rs}{M^3} \left(\frac{\partial V_\theta}{\partial \theta} \right)^2 \\
& + \frac{\partial V_\theta}{\partial \theta} \left(\frac{-\eta rs}{M^2 k_4} \frac{\partial V_z}{\partial \theta} + \frac{\eta rs}{M^3} \frac{\partial V_z}{\partial z} - \frac{\eta rs}{k_4 M^2} \frac{\partial V_z}{\partial \theta} \right) \\
& + \frac{\eta rs}{Mk_4^2} \left(\frac{\partial V_z}{\partial \theta} \right)^2 + \frac{\eta rs}{M^3} \frac{\partial V_z}{\partial \theta} \frac{\partial V_\theta}{\partial z} - \frac{\eta rs}{k_4 M^2} \frac{\partial^2 V_z}{\partial \theta \partial z}
\end{aligned} \right\} \text{drd } \theta \text{ dz}
\end{aligned}$$

(3.121)

$$9. [\pi_z \cdot v_z]_z - [\pi_z \cdot v_z]_{z+dz} = -\frac{\partial}{\partial z} [\tau_{rz} v_z] r dr d\theta dz = -\left[\frac{\partial \tau_{rz}}{\partial z} v_z + \tau_{rz} \frac{\partial v_z}{\partial z} \right] r dr d\theta dz \quad (3.122)$$

$$= -\left[\frac{\partial}{\partial z} \left(-\eta \frac{\partial v_z}{\partial r} \right) v_z - \eta \frac{\partial v_z}{\partial r} \frac{\partial v_z}{\partial z} \right] r dr d\theta dz = \frac{\partial}{\partial z} \left(\eta \frac{\partial v_z}{\partial r} \right) v_z + \eta \frac{\partial v_z}{\partial r} \frac{\partial v_z}{\partial z} \quad (3.123)$$

$$= \left(\frac{\partial \eta}{\partial z} \frac{\partial v_z}{\partial r} + \eta \frac{\partial}{\partial z} \left(\frac{\partial v_z}{\partial r} \right) \right) v_z + \eta \frac{\partial v_z}{\partial r} \frac{\partial v_z}{\partial z} \quad (3.124)$$

$$= \left[\begin{array}{l} \left[\frac{1}{R} \frac{\partial \eta}{\partial z} \left(\frac{1}{R} \frac{\partial}{\partial r} + \frac{rs}{M^2} \frac{\partial}{\partial \theta} \right) R v_z + \right. \\ \left. \eta \frac{1}{R} \frac{\partial}{\partial z} \left(\frac{1}{R} \frac{\partial}{\partial r} + \frac{rs}{M^2} \frac{\partial}{\partial \theta} \right) R v_z \right] R v_z \\ \left. + \eta \left[\frac{1}{R} \frac{\partial}{\partial r} + \frac{rs}{M^2} \frac{\partial}{\partial \theta} \right] R v_z \frac{1}{R} \frac{\partial}{\partial z} R v_z \right] r dr d\theta dz \quad (3.125)$$

$$= \left[\begin{array}{l} R r v_z \frac{\partial \eta}{\partial z} \frac{\partial v_z}{\partial r} + v_z \frac{(Rr)^2 s}{M^2} \frac{\partial \eta}{\partial z} \frac{\partial v_z}{\partial \theta} + R r \eta (1 + v_z) \frac{\partial^2 v_z}{\partial z \partial r} \\ + \frac{\eta (Rr)^2 s}{M^2} (1 + v_z) \frac{\partial^2 v_z}{\partial z \partial \theta} \end{array} \right] r dr d\theta dz \quad (3.126)$$

The last term of the energy balance equation is the heat of dissipation, which is shown by the equation below:

$$10. \overset{\circ}{q}_{Diss} = \left(\eta \gamma_{Total}^2 \right) R r dr d\theta dz; \quad (3.127)$$

A successful screw design is one in which the amount of shear heat generated is sufficient to ensure that all the polymer is converted to a suitable molten state before the end of the screw. In cylindrical coordinate the total shear rate is given by:

$$\gamma_{\text{Total}} = \sqrt{\left(r \frac{d}{dr} \left(\frac{V_\theta}{r}\right)\right)^2 + \left(\frac{dV_z}{dr}\right)^2} \quad (3.128)$$

Using the transformers matrices, the above equation will be transformed to helical coordinate as follows:

$$\frac{d}{dr} \left(\frac{V_\theta}{r}\right) = \frac{d}{dr} \left(\frac{-1}{RrM} V_\theta + \frac{1}{Rrk_4} V_z\right) = \left(\frac{1}{R} \frac{\partial}{\partial r} + \frac{rs}{M^2} \frac{\partial}{\partial \theta}\right) \cdot \left(\frac{-1}{RrM} V_\theta + \frac{1}{Rrk_4} V_z\right) \quad (3.129)$$

$$= \left(\frac{-1}{R^2Mr} \frac{\partial V_\theta}{\partial r} + \frac{1}{R^2k_4r} \frac{\partial V_z}{\partial r} - \frac{s}{RM^3} \frac{\partial V_\theta}{\partial \theta} + \frac{s}{RM^2k_4} \frac{\partial V_z}{\partial \theta}\right) \quad (3.130)$$

Since

$$r \cdot \frac{d}{dr} \left(\frac{V_\theta}{r}\right) = Rr \cdot \frac{d}{dr} \left(\frac{V_\theta}{r}\right) = \left(\frac{-1}{RM} \frac{\partial V_\theta}{\partial r} + \frac{1}{Rk_4} \frac{\partial V_z}{\partial r} - \frac{rs}{M^3} \frac{\partial V_\theta}{\partial \theta} + \frac{rs}{M^2k_4} \frac{\partial V_z}{\partial \theta}\right) \quad (3.131)$$

and

$$\frac{d}{dr} (V_z) = \frac{d}{dr} (RV_z) = \left(\frac{1}{R} \frac{\partial}{\partial r} + \frac{rs}{M^2} \frac{\partial}{\partial \theta}\right) \cdot (RV_z) = \frac{\partial V_z}{\partial r} + \frac{Rrs}{M^2} \frac{\partial V_z}{\partial \theta} \quad (3.132)$$

$$\gamma_{\text{Total}} = \sqrt{\left[\left(\frac{-1}{RM} \frac{\partial V_\theta}{\partial r} + \frac{1}{Rk_4} \frac{\partial V_z}{\partial r} - \frac{rs}{M^3} \frac{\partial V_\theta}{\partial \theta} + \frac{rs}{M^2k_4} \frac{\partial V_z}{\partial \theta}\right)\right]^2 + \left[\frac{\partial V_z}{\partial r} + \frac{Rrs}{M^2} \frac{\partial V_z}{\partial \theta}\right]^2} \quad (3.133)$$

Using Equations (3.92) to (3.127) from the energy balance equation and applying Equations (3.128) to (3.133) for the heat of dissipation, the energy balance equation in a helical coordinate for a non-Newtonian non-isothermal polymer melt flowing in the helix channel of an extruder screw can be expressed as:

$$\begin{aligned}
& -\frac{1}{Rr} \frac{\partial \eta}{\partial \theta} \left(\frac{-1}{M} V_0^2 - \frac{M}{k_4^2} V_z^2 + \frac{2}{k_4} V_0 V_z \right) \\
& - \frac{\partial V_0}{\partial \theta} \left(\frac{-\eta V_0}{RrM} + \frac{\eta V_z}{Rrk_4} + \frac{rs}{M^3} V_0 \frac{\partial \eta}{\partial \theta} - \frac{rs k_4}{M^4} V_0 \frac{\partial \eta}{\partial z} - \frac{rs}{k_4 M^2} V_z \frac{\partial \eta}{\partial z} + \frac{rs}{M^3} V_z \frac{\partial \eta}{\partial z} + \frac{\eta}{Rr} \left(\frac{-1}{M} V_0 + \frac{1}{k_4} V_z \right) \right) \\
& \quad \left(-\frac{\eta rs}{M^2 k_4} \frac{\partial V_z}{\partial \theta} + \frac{\eta rs}{M^3} \frac{\partial V_z}{\partial z} - \frac{\eta rs}{k_4 M^2} \frac{\partial V_z}{\partial \theta} \right) \\
& - \frac{1}{Rr} \frac{\partial \eta}{\partial z} \left(\frac{k_4}{M^2} V_0^2 + \frac{1}{k_4} V_z^2 - \frac{2}{M} V_0 V_z \right) \\
& - \frac{\partial V_z}{\partial \theta} \left(\frac{\eta V_0}{Rrk_4} - \frac{\eta M V_z}{Rrk_4} - \frac{rs}{k_4 M^2} V_0 \frac{\partial \eta}{\partial \theta} + \frac{rs}{M^3} V_0 \frac{\partial \eta}{\partial z} + \frac{rs}{k_4 M^2} V_z \frac{\partial \eta}{\partial \theta} - \frac{rs}{k_4 M^2} V_z \frac{\partial \eta}{\partial z} - \frac{\eta M}{Rrk_4} \left(\frac{-1}{M} V_0 + \frac{1}{k_4} V_z \right) \right) \\
& \quad \left(+ V_z \frac{(Rr)^2 s}{M^2} \frac{\partial \eta}{\partial z} \right) \\
& - \frac{\partial V_0}{\partial z} \left(\frac{\eta k_4}{RrM} V_0 - \frac{\eta}{RrM} V_z - \frac{\eta k_4}{RrM} \left(\frac{-1}{M} V_0 + \frac{1}{k_4} V_z \right) + \frac{\eta rs}{M^3} \frac{\partial V_z}{\partial \theta} \right) \\
& - \frac{\partial V_z}{\partial z} \left(\frac{-\eta}{RrM} V_0 + \frac{\eta}{Rrk_4} V_z + \frac{\eta}{Rr} \left(\frac{-1}{M} V_0 + \frac{1}{k_4} V_z \right) + R\eta C p T \right) \\
& - \frac{\partial V_0}{\partial r} \left(\frac{1}{RM} V_0 \frac{\partial \eta}{\partial \theta} - \frac{k_4}{RM^2} V_0 \frac{\partial \eta}{\partial z} - \frac{1}{Rk_4} V_z \frac{\partial \eta}{\partial \theta} + \frac{1}{RM} V_z \frac{\partial \eta}{\partial z} - \frac{\eta}{Rk_4} \frac{\partial V_z}{\partial \theta} - \frac{\eta k_4}{RM} \frac{\partial V_0}{\partial z} + \frac{\eta}{RM} \frac{\partial V_z}{\partial z} \right) \\
& - \frac{\partial V_z}{\partial r} \left(\frac{-1}{Rk_4} V_0 \frac{\partial \eta}{\partial \theta} + \frac{1}{RM} V_0 \frac{\partial \eta}{\partial z} + \frac{M}{Rk_4^2} V_z \frac{\partial \eta}{\partial \theta} - \frac{1}{Rk_4} V_z \frac{\partial \eta}{\partial z} + Rr V_z \frac{\partial \eta}{\partial z} - \frac{\eta}{Rk_4} \frac{\partial V_0}{\partial \theta} + \frac{\eta}{RM} \frac{\partial V_0}{\partial z} \right) \\
& - \frac{\partial^2 V_0}{\partial r \partial \theta} \left(\frac{-\eta}{R} \left(\frac{-1}{M} V_0 + \frac{1}{k_4} V_z \right) + \frac{\eta}{RM} \right) - \frac{\partial^2 V_z}{\partial r \partial \theta} \left(\frac{\eta M}{Rk_4} \left(\frac{-1}{M} V_0 + \frac{1}{k_4} V_z \right) + \frac{\eta}{Rk_4^2} \right) \\
& + \eta \left(\frac{-1}{M} V_0 + \frac{1}{k_4} V_z \right) \left(\frac{rs}{M^2} \frac{\partial^2 V_0}{\partial \theta^2} - \frac{rs}{k_4 M} \frac{\partial^2 V_z}{\partial \theta^2} - \frac{k_4}{RM} \frac{\partial^2 V_0}{\partial r \partial z} \right) \\
& - \frac{\partial^2 V_z}{\partial r \partial z} \left(\frac{-\eta}{R} \left(\frac{-1}{M} V_0 + \frac{1}{k_4} V_z \right) - \frac{\eta}{Rk_4} + R\eta(1 + V_z) \right) - \frac{\partial^2 V_0}{\partial z \partial \theta} \left(\frac{\eta rs k_4}{M^3} \left(\frac{-1}{M} V_0 + \frac{1}{k_4} V_z \right) - \frac{\eta rs k_4}{M^4} \right) \\
& - \frac{\partial^2 V_z}{\partial z \partial \theta} \left(\frac{-\eta rs}{M^2} \left(\frac{-1}{M} V_0 + \frac{1}{k_4} V_z \right) - \frac{\eta rs}{k_4 M^2} + \frac{\eta (Rr)^2 s}{M^2} (1 + V_z) - \frac{\eta rs}{k_4 M^2} \right) - \frac{\eta rs}{M^3} \left(\frac{\partial V_0}{\partial \theta} \right)^2 \\
& - \frac{\eta rs}{M k_4^2} \left(\frac{\partial V_z}{\partial \theta} \right)^2 + R\eta \gamma_{\text{total}}^2
\end{aligned}$$

(3.134)

Equation (3.134) can be rearranged first to the equation below:

$$\begin{aligned}
& - \left(r \frac{K}{R} + K k_4^2 \right) \frac{\partial^2 T}{\partial z^2} = \\
& - \rho C_p T \left(\frac{\partial V_\theta}{\partial \theta} - \frac{M}{k_4} \frac{\partial V_z}{\partial \theta} - \frac{k_4}{M} \frac{\partial V_\theta}{\partial z} + \frac{\partial V_z}{\partial z} \right) - \left(C_p T \frac{\partial \rho}{\partial T} + \rho T \frac{\partial C_p}{\partial T} + \rho C_p \right) \\
& \cdot \left(\left(V_\theta - \frac{M}{k_4} V_z \right) \frac{\partial T}{\partial \theta} + \left(V_z - \frac{k_4}{M} V_\theta + R r V_z \right) \frac{\partial T}{\partial z} \right) \\
& + R r \frac{\partial K}{\partial T} \left[\frac{1}{R^2} \left(\frac{\partial T}{\partial r} \right)^2 + \frac{2 r s}{R M^2} \frac{\partial T}{\partial \theta} \frac{\partial T}{\partial r} + \frac{(r s)^2}{M^4} \left(\frac{\partial T}{\partial \theta} \right)^2 \right] + \frac{K}{R} \frac{\partial T}{\partial r} + \frac{K r s}{M^2} \frac{\partial T}{\partial \theta} \\
& + K R r \left(\frac{1}{R^2} \frac{\partial^2 T}{\partial r^2} + \frac{2 r s}{R M^2} \frac{\partial^2 T}{\partial r \partial \theta} + \frac{(r s)^2}{M^4} \frac{\partial^2 T}{\partial \theta^2} \right) \\
& + \frac{\partial K}{\partial T} \left(\left(\frac{r}{R} + k_4^2 \right) \left(\frac{\partial T}{\partial z} \right)^2 + M^2 \left(\frac{\partial T}{\partial \theta} \right)^2 - 2 M k_4 \frac{\partial T}{\partial \theta} \frac{\partial T}{\partial z} \right) + K \left(M^2 \frac{\partial^2 T}{\partial \theta^2} - 2 M k_4 \frac{\partial^2 T}{\partial z \partial \theta} \right) \\
& - \frac{1}{R r} \frac{\partial \eta}{\partial \theta} \left(\frac{-1}{M} V_\theta^2 - \frac{M}{k_4^2} V_z^2 + \frac{2}{k_4} V_\theta V_z \right) \\
& - \frac{\partial V_\theta}{\partial r} \left(\frac{1}{R M} V_\theta \frac{\partial \eta}{\partial \theta} - \frac{k_4}{R M^2} V_\theta \frac{\partial \eta}{\partial z} - \frac{1}{R k_4} V_z \frac{\partial \eta}{\partial \theta} + \frac{1}{R M} V_z \frac{\partial \eta}{\partial z} \right) \\
& - \frac{\partial V_z}{\partial r} \left(\frac{-1}{R k_4} V_\theta \frac{\partial \eta}{\partial \theta} + \frac{1}{R M} V_\theta \frac{\partial \eta}{\partial z} + \frac{M}{R k_4^2} V_z \frac{\partial \eta}{\partial \theta} - \right. \\
& \left. \frac{1}{R k_4} V_z \frac{\partial \eta}{\partial z} - R r V_z \frac{\partial \eta}{\partial z} \right) \\
& - \frac{\partial^2 V_\theta}{\partial r \partial \theta} \eta \left(\frac{1}{R M} V_\theta - \frac{1}{R k_4} V_z \right) - \frac{\partial^2 V_z}{\partial r \partial \theta} \eta \left(\frac{-1}{R k_4} V_\theta + \frac{M}{R k_4^2} V_z \right) \\
& - \frac{\partial^2 V_\theta}{\partial \theta^2} \eta \left(\frac{r s}{M^3} V_\theta - \frac{r s}{M^2 k_4} V_z \right) \\
& - \frac{\partial^2 V_z}{\partial \theta^2} \eta \left(\frac{-r s}{M^2 k_4} V_\theta + \frac{r s}{M k_4^2} V_z \right) - \frac{\partial^2 V_\theta}{\partial r \partial z} \eta \left(\frac{-k_4}{R M^2} V_\theta + \frac{1}{R M} V_z \right) \\
& + \left(- \eta \left(\frac{1}{R M} V_\theta - \frac{1}{R k_4} V_z \right) + R r \eta V_z \right) \frac{\partial^2 V_z}{\partial r \partial z} \\
& - \eta \left(\frac{-k_4 r s}{M^4} V_\theta + \frac{r s}{M^3} V_z \right) \frac{\partial^2 V_\theta}{\partial z \partial \theta} + \left(- \eta \left(\frac{r s}{M^3} V_\theta - \frac{r s}{k_4 M^2} V_z \right) \right. \\
& \left. + \eta V_z \frac{(R r)^2 s}{M^2} \right) \frac{\partial^2 V_z}{\partial z \partial \theta} \\
& - \frac{\eta r s}{M k_4^2} \left(\frac{\partial V_z}{\partial \theta} \right)^2 - \frac{\eta r s}{M^3} \left(\frac{\partial V_\theta}{\partial \theta} \right)^2 \\
& + R r \eta \gamma \frac{2}{T}
\end{aligned} \tag{3.135}$$

After further rearrangements and simplifications, the final energy balance equation in helical coordinates is shown below:

$$\begin{aligned}
& \frac{K_r}{R} \frac{\partial^2 T}{\partial z^2} = -\rho C_p T V_\theta \frac{\partial V_\theta}{\partial \theta} - V_\theta \frac{\partial T}{\partial \theta} \left[C_p T \frac{\partial \rho}{\partial T} + \rho T \frac{\partial C_p}{\partial T} + \rho C_p \right] \\
& - \left[R r V_z \frac{\partial T}{\partial z} \left(C_p T \frac{\partial \rho}{\partial T} + \rho T \frac{\partial C_p}{\partial T} + \rho C_p \right) \right] \\
& - R r \rho (C_p T)^2 \frac{\partial V_z}{\partial z} - b R^2 V_z \rho C_p T \\
& - \frac{\partial K}{\partial T} \left[\frac{r}{R} \left(\frac{\partial T}{\partial r} \right)^2 + \frac{2 r^2 s}{R M^2} \frac{\partial^2 T}{\partial r \partial \theta} + \frac{r}{R} \frac{(rs)^2}{M^4} \left(\frac{\partial T}{\partial \theta} \right)^2 \right] - \frac{K}{R} \frac{\partial T}{\partial r} \\
& - \frac{K r s}{R M^2} \frac{\partial T}{\partial \theta} - K R r \left(\frac{1}{R^2} \frac{\partial^2 T}{\partial r^2} + \frac{2 r s}{R^2 M^2} \frac{\partial^2 T}{\partial r \partial \theta} + \frac{(rs)^2}{R^2 M^4} \frac{\partial^2 T}{\partial \theta^2} \right) - \frac{r}{R} \frac{\partial K}{\partial T} \left(\frac{\partial T}{\partial z} \right)^2 - K b \frac{\partial T}{\partial z} \\
& + \frac{V_\theta}{M} \left[\frac{1}{R r} \frac{\partial \eta}{\partial \theta} V_\theta + \frac{\eta}{R r} \frac{\partial V_\theta}{\partial \theta} - \frac{\partial \eta}{\partial \theta} \left(\frac{1}{R} \frac{\partial V_\theta}{\partial r} + \frac{r s}{R M^2} \frac{\partial V_\theta}{\partial \theta} \right) - \eta \left(\frac{1}{R} \frac{\partial^2 V_\theta}{\partial r \partial \theta} + \frac{r s}{R M^2} \frac{\partial^2 V_\theta}{\partial \theta^2} \right) \right] \\
& + \frac{\eta}{R r M} V_\theta \frac{\partial V_\theta}{\partial \theta} - \frac{\eta}{M} \left(\frac{1}{R} \frac{\partial V_\theta}{\partial r} + \frac{r s}{R M^2} \frac{\partial V_\theta}{\partial \theta} \right) \frac{\partial V_\theta}{\partial \theta} \\
& - M^2 \frac{\partial K}{\partial T} \left(\frac{\partial T}{\partial \theta} \right)^2 - K M^2 \frac{\partial^2 T}{\partial \theta^2} + R^2 r V_z \left(\frac{\partial \eta}{\partial z} \left[\frac{1}{R} \frac{\partial V_z}{\partial r} + \frac{r s}{R M^2} \frac{\partial V_z}{\partial \theta} \right] \right) \\
& + R^2 r V_z \eta \left(\frac{1}{R} \frac{\partial^2 V_z}{\partial r \partial z} + \frac{r s}{R M^2} \frac{\partial^2 V_z}{\partial \theta \partial z} \right) + R^2 r \eta \left[\frac{1}{R} \frac{\partial V_z}{\partial r} + \frac{r s}{R M^2} \frac{\partial V_z}{\partial \theta} \right] \frac{\partial V_z}{\partial z} \\
& + b R^3 V_z \eta \left[\frac{1}{R} \frac{\partial V_z}{\partial r} + \frac{r s}{R M^2} \frac{\partial V_z}{\partial \theta} \right] + q_{DISS}
\end{aligned} \tag{3.136}$$

The above equation is a combination of convective energy flux, heat conduction from the barrel to the polymer, work associated with molecular motion and by bulk fluid motion (flow system), and irreversible rate of internal energy increase per unit volume by viscous dissipation (q_{DISS}). As can be seen, the equation above is a partial differential equation with the order of two for the melt temperature gradient across the length of the extruder ($\frac{\partial^2 T}{\partial z^2}$). Also because the coordinate system is non-orthogonal, mixed derivatives are

appeared in the energy balance equation. Similar to Equation (3.26) and for the same aforementioned reason, we define a new state variable:

$$\beta = \frac{\partial T}{\partial z} \tag{3.137}$$

The following example illustrates the approach taken to simplify the mixed variables shown in Equation (3.136):

$$\frac{\partial^2 T}{\partial r \partial \theta} = \frac{\partial}{\partial r} \left(\frac{\partial T}{\partial \theta} \right) = \frac{\partial A}{\partial r} = \frac{A[i + 1, j] - A[i - 1, j]}{2\Delta r}$$

$$A = \frac{\partial T}{\partial \theta}$$

$$\text{Now : } \frac{\partial^2 T}{\partial r \partial \theta} = \frac{A[i + 1, j + 1] - A[i - 1, j - 1]}{4\Delta r \Delta \theta}$$

(3.138)

3.11 Initial and Boundary Conditions

The initial conditions under steady state along the z direction are as follows:

$$T(r, \theta, 0) = T_{ini} \quad (3.139)$$

$$V_{\theta}(r, \theta, 0) = \sqrt{k \frac{r^2}{4} + r^2} \quad (3.140)$$

$$V_z(r, \theta, 0) = r\omega \cos \psi \quad (3.141)$$

where V_{θ} , V_z , and T are known at $z=0$. T_{ini} represents the inlet resin temperature. Thus, the temperature of resin throughout the injection process at $z = 0$ is equal to its initial value at the inlet of the injection unit.

The boundary conditions for the model under steady-state operation are as follows:

At the barrel, the plastic melt temperature is equal to the set temperature of the barrel.

Also V_{θ} and V_z at the barrel are as follows:

$$T(1, \theta, z) = T_b \quad (3.142)$$

$$V_{\theta}(1, \theta, z) = 0 \quad (3.143)$$

$$V_z(1, \theta, z) = 0 \quad (3.144)$$

At the screw shaft an adiabatic process is assumed where no heat is gained or lost by the system so V_{θ} , V_z , and T at that location are given as follows:

$$\left(\frac{\partial T}{\partial r} \right)_{\frac{r}{R}, \theta, z} = 0 \quad (3.145)$$

$$V_z \left(\frac{r}{R}, \theta, z \right) = r\omega \cos \psi \quad (3.146)$$

$$V_{\theta} \left(\frac{r}{R}, \theta, z \right) = \sqrt{k \frac{r^2}{4} + r^2} \quad (3.147)$$

where V_θ and V_z are the melt angular and the axial velocities at the direction of the screw shaft. In Equations (3.146) and (3.147), ω represents the screw speed in rpm, and ψ is the solid conveying angle. At the screw shaft, the temperature change is adiabatic. Angular and axial melt velocities at barrel surface are zero. The mathematical model developed above is indeed complex, and obviously cannot be solved analytically. Hence, the next step is the numerical simulation of the developed model. At this point, it has to be noted that one could readily solve the developed model after discretizing its partial differential equations into a set of ordinary differential equations. The boundary conditions are straightforward as opposed to what they would have been in a non-helical geometry.

3.12 Solution Approach

The transport equations derived above (i.e. momentum balance equations and energy balance equations) are indirectly coupled because every velocity component appears in each momentum equation, the energy balance and the mass balance equations. The most complex issue to resolve is the role played by the pressure [Versteeg 07]. This term appears in all momentum equations, but there is evidently no equation for the pressure. In fluid computations we wish to calculate the pressure field as part of the solution, so its gradient is not known beforehand. If the correct pressure field is used in the momentum equations, the resulting velocity field should satisfy equation of continuity. This problem can be resolved by adopting an iterative solution strategy (e.g. SIMPLE algorithm of Patankar [Patankar 72]).

To start the algorithm, a guessed pressure field is used to solve the momentum equations. The velocity profiles computed from momentum equations will have to satisfy the equation of continuity. If this equation is not satisfied, then a pressure correction equation (e.g. Newton Raphson Method) is used to update the pressure field. So the aim is to progressively improve the guessed pressure fields until the convergence of velocity and pressure field. This algorithm is shown in Figure 16. As it has been laid out in the flow chart, an initial pressure guess is required to compute the velocity profiles from the momentum balance equations. A good pressure guess is atmospheric, which is the resin pressure under the feed hopper. In fact, our numerical experiments with different pressure

guesses corroborated this approach. Shear stress, shear rate and temperature profiles in all three axes are computed by the initial pressure guess as well as any updated guess. The velocity profiles will be applied to the mass balance equation. If these profiles can satisfy the equation of continuity (e.g. no residual is remained), the guessed pressure field will be used in the starting of the simulation, otherwise the pressure will be updated by the shooting method until the residual is insignificant. The shooting method equation is presented below:

$$P^{i+1} = P^i - \frac{F^i}{\left[\frac{\partial F}{\partial P}\right]^i} \quad (3.148)$$

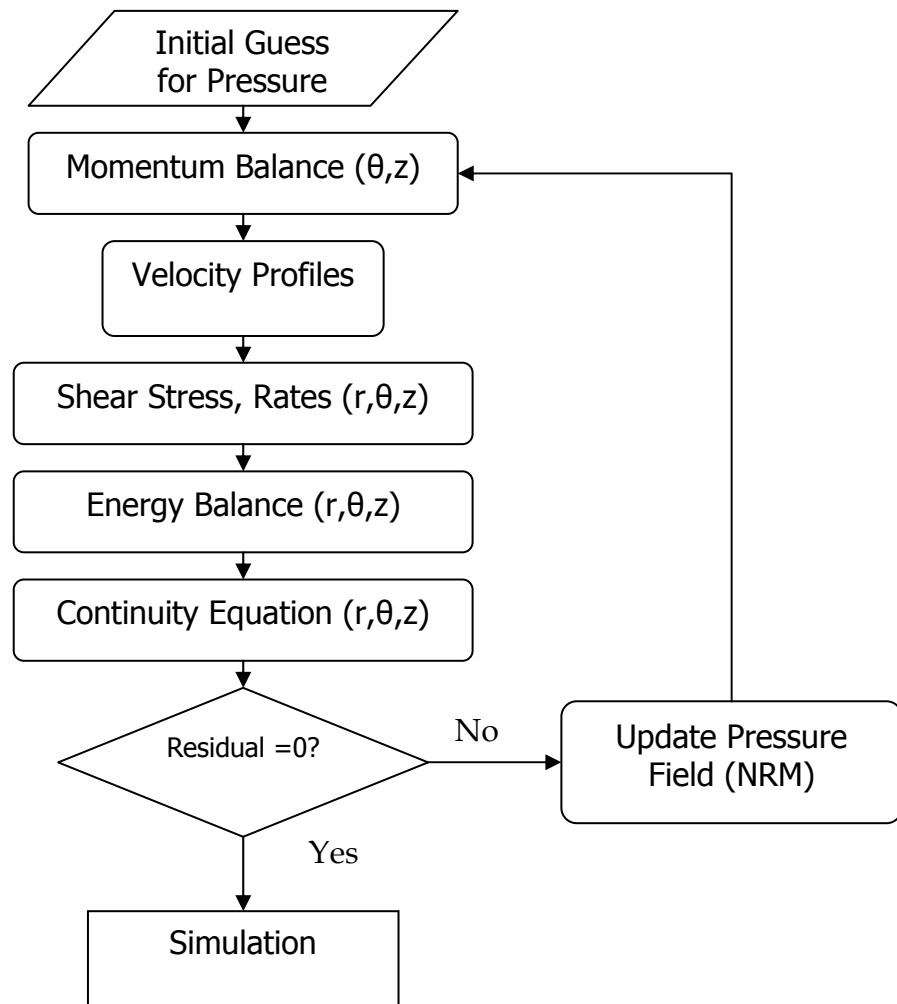


Figure 16: Solution algorithm

Where $F(V_\theta(p), V_z(p))$ is the equation of continuity. The denominator of the pressure correction equation is expanded as:

$$\left[\frac{\partial F}{\partial P} \right] = \frac{\partial F}{\partial V_\theta} \cdot \frac{\partial V_\theta}{\partial P} + \frac{\partial F}{\partial V_z} \cdot \frac{\partial V_z}{\partial P} \quad (3.149)$$

Therefore, it is necessary to derive the velocity gradients along θ and z directions with respect to pressure to replace in the pressure correction equation.

3.12.1 Derivation of $\frac{\partial V_\theta}{\partial p}$:

$$\begin{aligned}
&\Rightarrow \left(\frac{k_4}{Rr^h M^2} \frac{\partial V_\theta}{\partial P} - \left(\frac{1}{RrM} + \frac{1}{M} \right) \frac{\partial V_z}{\partial P} \right) \frac{\partial V_\theta}{\partial z} \\
&+ \left(\frac{k_4}{RrM^2} V_\theta - \left(\frac{1}{RrM} + \frac{1}{M} \right) V_z \right) \cdot \frac{\partial}{\partial z} \left(\frac{\partial V_\theta}{\partial P} \right) = \\
&\left(\frac{1}{RrM} \frac{\partial V_\theta}{\partial P} - \frac{1}{Rrk_4} \frac{\partial V_z}{\partial P} \right) \frac{\partial V_\theta}{\partial \theta} \\
&+ \left(\frac{1}{RrM} V_\theta - \frac{1}{Rrk_4} V_z - \frac{\eta s}{RM^3} - \frac{rs}{RM^3} \frac{\partial \eta}{\partial r} - \frac{r^2 s^2}{M^5} \frac{\partial \eta}{\partial \theta} \right) \\
&\cdot \frac{\partial}{\partial \theta} \left(\frac{\partial V_\theta}{\partial P} \right) + \left(\frac{-1}{Rrk_4} \frac{\partial V_\theta}{\partial P} + \frac{M}{Rrk_4^2} \frac{\partial V_z}{\partial P} \right) \frac{\partial V_z}{\partial \theta} \\
&+ \left(\frac{-1}{Rrk_4} V_\theta + \frac{M}{Rrk_4^2} V_z + \frac{\eta s}{Rk_4 M^2} + \frac{rs}{RM^2 k_4} \frac{\partial \eta}{\partial r} + \frac{r^2 s^2}{M^4 k_4} \frac{\partial \eta}{\partial \theta} \right) \cdot \frac{\partial}{\partial \theta} \left(\frac{\partial V_z}{\partial P} \right) \\
&+ \left(\frac{1}{RrM} \frac{\partial V_\theta}{\partial P} - \left(\frac{1}{Rrk_4} + \frac{1}{k_4} \right) \frac{\partial V_z}{\partial P} \right) \frac{\partial V_z}{\partial z} \\
&+ \left(\frac{1}{RrM} V_\theta - \frac{1}{Rrk_4} V_z - \frac{1}{k_4} V_z \right) \cdot \frac{\partial}{\partial z} \left(\frac{\partial V_z}{\partial P} \right) \\
&+ \left(\frac{\eta}{r^2 R^2 M} + \frac{1}{R^2 r M} \frac{\partial \eta}{\partial r} + \frac{s}{RM^3} \frac{\partial \eta}{\partial \theta} \right) \frac{\partial V_\theta}{\partial P} \\
&+ \left(-\frac{\eta}{r^2 R^2 k_4} - \frac{1}{R^2 r k_4} \frac{\partial \eta}{\partial r} - \frac{s}{RM^2 k_4} \frac{\partial \eta}{\partial \theta} \right) \frac{\partial V_z}{\partial P} + \\
&\left(-\frac{\eta}{rR^2 M} - \frac{1}{R^2 M} \frac{\partial \eta}{\partial r} - \frac{rs}{RM^3} \frac{\partial \eta}{\partial \theta} \right) \frac{\partial}{\partial r} \left(\frac{\partial V_\theta}{\partial P} \right) \\
&+ \left(\frac{\eta}{rR^2 k_4} + \frac{1}{R^2 k_4} \frac{\partial \eta}{\partial r} + \frac{rs}{RM^2 k_4} \frac{\partial \eta}{\partial \theta} \right) \frac{\partial}{\partial r} \left(\frac{\partial V_z}{\partial P} \right) \\
&- \frac{\eta}{R^2 M} \frac{\partial^2}{\partial r^2} \left(\frac{\partial V_\theta}{\partial P} \right) + \frac{\eta}{R^2 k_4} \frac{\partial^2}{\partial r^2} \left(\frac{\partial V_z}{\partial P} \right) - \frac{2\eta rs}{RM^3} \frac{\partial^2 \beta}{\partial r \partial \theta} + \frac{2\eta rs}{RM^2 k_4} \frac{\partial^2 \alpha}{\partial r \partial \theta} \\
&- \frac{\eta r^2 s^2}{M^5} \frac{\partial^2}{\partial \theta^2} \left(\frac{\partial V_\theta}{\partial P} \right) + \frac{\eta r^2 s^2}{M^4 k_4} \frac{\partial^2}{\partial \theta^2} \left(\frac{\partial V_z}{\partial P} \right)
\end{aligned} \tag{3.150}$$

3.12.2 Derivation of $\frac{\partial V_z}{\partial P}$:

$$\begin{aligned}
&\Rightarrow \left(-\frac{k_4}{rM} V_\theta + \left(\frac{1}{r} + R \right) V_z \right) \frac{\partial}{\partial z} \left(\frac{\partial V_z}{\partial P} \right) \\
&+ \left(-\frac{k_4}{rM} \frac{\partial V_\theta}{\partial P} + \left(\frac{1}{r} + R \right) \frac{\partial V_z}{\partial P} \right) \frac{\partial V_z}{\partial z} = \\
&- \left(\frac{1}{r} \frac{\partial V_\theta}{\partial P} - \frac{M}{rk_4} \frac{\partial V_z}{\partial P} \right) \frac{\partial V_z}{\partial \theta} \\
&- \left(\frac{1}{r} V_\theta - \frac{M}{r^h k_4} V_z - \frac{\eta s}{M^2} - \frac{rs}{M^2} \frac{\partial \eta}{\partial r} - \frac{Rr^2 s^2}{M^4} \frac{\partial \eta}{\partial \theta} \right) \cdot \frac{\partial}{\partial \theta} \left(\frac{\partial V_z}{\partial P} \right) \\
&+ \left(\frac{\eta}{Rr} + \frac{1}{R} \frac{\partial \eta}{\partial r} + \frac{rs}{M^2} \frac{\partial \eta}{\partial \theta} \right) \frac{\partial}{\partial r} \left(\frac{\partial V_z}{\partial P} \right) + \frac{\eta}{R} \frac{\partial^2}{\partial r^2} \left(\frac{\partial V_z}{\partial P} \right) \\
&+ 2 \frac{\eta rs}{M^2} \frac{\partial^2 \beta}{\partial r \partial \theta} + \frac{\eta Rr^2 s^2}{M^4} \frac{\partial^2}{\partial \theta^2} \left(\frac{\partial V_z}{\partial P} \right)
\end{aligned} \tag{3.151}$$

3.13 Simulation Details

The computational algorithm in the above section along with the viscosity model was programmed in an object-oriented paradigm. C++ language was used. The iterative corrections in the pressure field were terminated when the pressure changes dropped below 10^{-5} psi. The algorithm is computationally very intensive. It takes usually 10 to 12 hours to converge on a personal computer equipped with 3 GHz Pentium compiler and 1 GB RAM.

3.13.1 Grid Sizes

We used 2nd order finite difference formula [Chapra 05] to discretize the partial differential equations developed in this study. We are solving the final mathematical model with adaptive step size in two directions of r and θ . The z direction (Nz), is the point we store data in the program but the discretization is only along r and θ directions. The step size value for z direction (along the length of the screw) is selected as 10^{-4} mm

but depending on the stiffness of the equation, the step size will be changing between 10^{-3} and 10^{-7} mm along the z direction.

3.13.2 Calculation of Proper Shot Size

During the screw recovery in injection molding, the screw is pulled back to allow certain volume of melt to be collected in front of its tip. This volume is referred to as *Shot Size* and is quantified using the diameter of the screw. The shot sizes that a machine can handle are a matter requiring careful consideration. The issue to balance is mainly to have a consistent, good quality, and homogenous melt for large or small shot sizes. A good quality melt refers to a melt, which has adequate average bulk temperature for processing a specific polymer. This is illustrated in more details in Figure 17. As the screw recovers, the resin temperature rises, which is the result of barrel heat conduction and shear heat dissipation. At some point along the screw, the resin's average bulk temperature might reach a minimum value where the polymer is melted and is deemed suitable for injection.

If the polymer resin melts with good quality before the end of the screw, the remaining screw length can be added to the injection unit shot size. As a result the melt temperature continuous to rise and the processing window will expand, which creates more production opportunity. One thing to keep in mind is that if the shot size is too large, the melt resides in the barrel for a long and unnecessary period of time and might become thermally degraded in which the status of the melt changes from good to poor standing.

Generally, prediction tools calculate the melt bulk temperature along the length of the injection screw. A properly designed tool captures the “L/D” (screw length over screw diameter) requirement for melting of a specific resin. The software designed in this work will report the required L/D for melting the polymer resin for a specific screw geometry as well as the final melt temperature at the end of the screw so the proper shot size for that specific process, screw, and polymer resin can be calculated.

Therefore, in a properly designed program, the prediction results not only allow an early investigation into the screw L/D requirements for melting, but also indicates how far to

the end of the screw this quality will remain. In Figure 17, it is tried to visually explain the discussion above. In this figure, it is assumed that the desired bulk temperature (285°C in this case) occurs at L/D=23 of the screw (e.g. a screw with 1250 mm length and 50 mm diameter contains 25 L/D units). From 23 to 25 L/D, there is 2 L/D of screw available, which can be added to the shot size related to this process . As shown in Figure 17, there is 2 L/D volume of melt available in each cycle, which might either improve or degrade the melt before exiting the injection barrel and the tool designed in this work is capable of capturing this possibility.

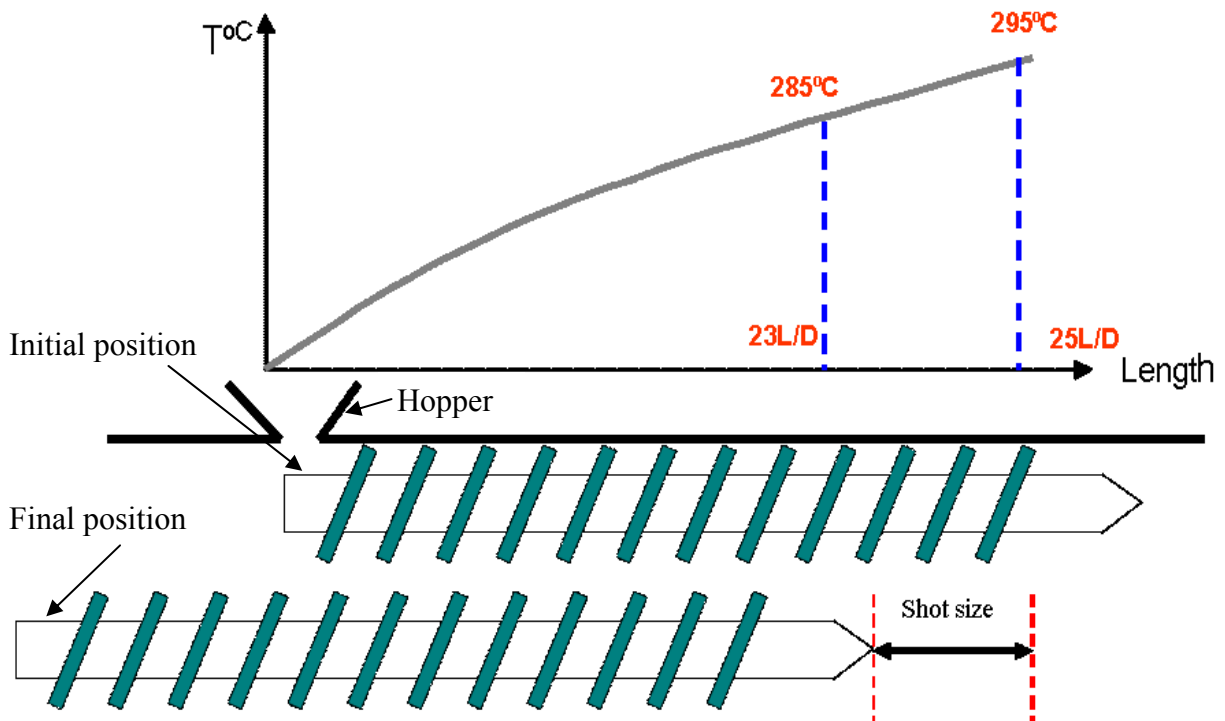


Figure 17: Linear motion of the screw. The simulation tool allows for a detailed investigation of melt bulk temperature at different points during the melting process.

3.13.3 'Screw Details':

Today in injection molding, molders are facing with many difficult challenges and new applications. Screw design is one practical science that most processors start with for new polymers and applications.

Recently with the development of new screws many dispersion and distribution problems with new polymers, additives, and colors are resolved. A simulation tool will make the validation of the screw performance designed for the purpose mentioned above fast and less expensive.

Since there are many different screw designs that exist throughout the injection molding industry, a reliable simulation program should allow investigation of all designs and study of their effectiveness at delivering good product quality at economic rates. In this work the design of screws is appropriately addressed and the details will be elaborated on in the following.

The software programs available commercially have mainly restrictions on how to detail a screw inside the simulation tool. Some have provided users with menus to pick screw known modules, elements, and sections. Vast majority of those packages incorporated the experimental data to the simulation tools for the purpose of validation and simplification. The sections of the screw (e.g. feed, compression, and metering) and their lengths can be selected in those packages but designs, which are not predetermined into the software initially are not mainly supported. In this work, the user can experience more flexibility with regards to the screw design. There are no limitations on the type, size, and location of the screw sections and modules and any geometry can be supported as long as it is properly integrated into the input file of the program. In order to facilitate and support any geometry in the screw, an array has been provided in the input file, which will allow the user to accurately draw their screw inside the simulation tool. The user needs to locate the ‘repeating’ units in a screw design and enter their start and end diameters as well as the lengths into the array. An example for a simple general purpose (GP) screw is shown below:

```
Initial Screw Diameter={47.82,47.82,59.84,69.84}  
End Screw Diameter={47.82,59.84,59.84,69.84}  
Length of each Screw Component={210,560,498,423}
```

In the above set of arrays, the first array indicates the initial screw shaft diameter of a section or repeating unit, while the second array specifies its end diameter. Figure 18 illustrates a schematic on how the above array matches the shape of the screw, which includes four distinct sections (i.e. feeding, melting, metering zone 1, and metering zone 2). As shown above, for the first 210 mm of the screw, the initial and end screw diameters are equal (47.82 mm), which indicates the feed section of the screw. This can be referred to as a repeatable unit where a mathematical relation specifies the changes in the screw geometry for the beginning and end of the screw length. Later, the second section of the screw (i.e. melting section) has an initial shaft diameter of 47.82 mm and end shaft diameter of 59.84 mm with a length of 560 mm. This is also a repeatable unit with slope. For the last two sections, there are two metering zones, one with equal and the other with a slop in initial and end screw shaft dimensions.

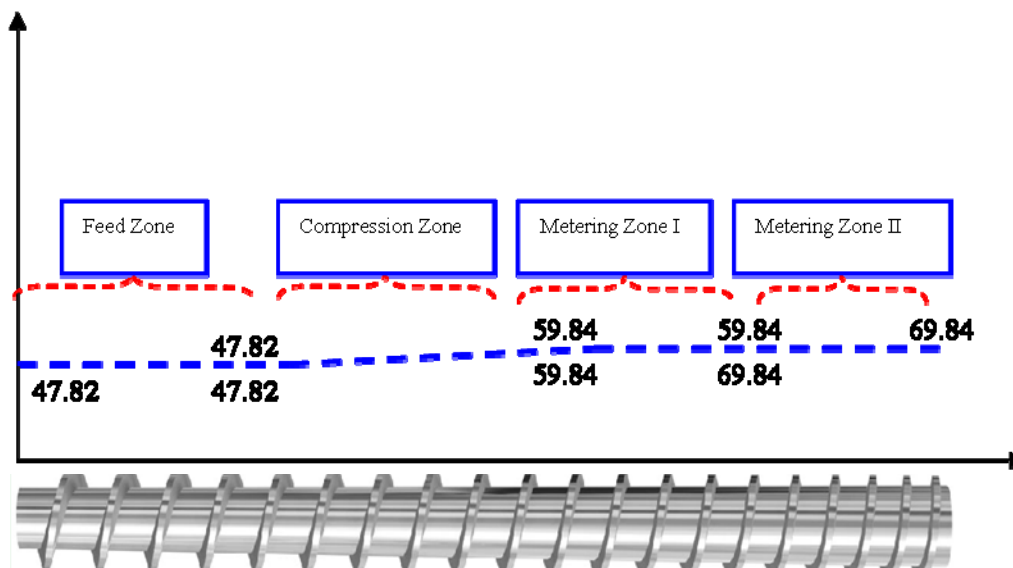


Figure 18: Characterization of the screw geometry inside the simulation input database (numerical units in mm)

In case an additional section is needed in the screw design (e.g. a barrier section, etc.), the array dimension will simply change to 5 and one more member is added inside the bracket to take into account the new section and its dimensions in the program.

3.14 Input Data Required for the Simulation

The accuracy of the simulation results depends on the accuracy of the input data. Basing predictions and evaluations on improperly evaluated processes could result in unexplainable simulation outcome. The most desirable situation is to obtain the processing properties of resins or resin mixtures (virgin material, regrind, additives, colorants, or even different types of plastic resins) from a polymer laboratory. Typically, this data consists of the following:

- Processing properties of the resin(s), including thermal, rheological and physical properties
- Screw geometry
- Extruder equipment conditions
- Operating conditions of the process

The prediction tool has the capability to store the data for different applications for any future reference. With the above information, the simulator explores the ‘what-if’ situations. The simulation results provide the ability to facilitate all design changes and observe the outcome in terms of production rate and product quality without conducting the actual experiment.

3.14.1 Pressure and Temperature

The steady-state model is time independent and the state variables (pressure and temperature) are investigated along the length of extruder. Some of the basic input data into the simulation software for Run 9 of the experimental tests (PET resin with barrel heat set of 285°C), which can be acquired from the screw blue print and material suppliers, are shown in Table 6.

Screw Speed	350	rpm
Barrel ID	80	mm
Screw OD	69.86	mm
Inlet resin temperature to the barrel	180	°C
Initial Pressure	0.1	Mpa
Barrel temperature setting	285	°C
Screw Back Pressure	300	psi

Table 6: Required screw processing parameters for the experimental tests

The following can be described as a typical behavior in the pressure and temperature of a PET material during the melting process in an injection unit. For the pressure profile, starting with atmospheric pressure at the feed throat location, initially a rapid increase in melt pressure is observed, which is due to the solid conveying that causes an exponential pressure growth in the feed region. It is then followed by steady pressure increase through the remainder of the feed section. The pressure rise will slow down (but still on the rise) along the transition and compression sections of the screw. Somewhere in the transition zone, a massive pressure drop is observed leading to the final screw backpressure, which is usually a fixed value and is equal to the hydraulic pressure multiplied by the intensification ratio of the injection unit (IR). This behavior depicts a typical performance of pressure change along the length of a single screw extruder.

For the temperature profile, the process starts with the resin entering from the dryer hopper to the injection unit and subsequently undergoing a sharp jump to its temperature due to contact with the heated barrel wall. Afterwards the steady increase of the melt temperature can be tracked along the screw axis.

Chapter 4

RESULTS

In this section the outcome of the simulation results are discussed in details. Melt temperature profile and melt pressure profile during recovery, screw length required to melt a specific resin (referred to as L/D), screw torque, screw power consumption, and viscosity change during the process are discussed respectively.

4.1 Melt Temperature at the Screw Tip

Table 7 summarizes the predicted melt temperature at the tip of the screw for Runs 1 through 10. In Runs 1-8 the melt temperature of a HDPE with MFI of 2 g/10min under different processing conditions and screw designs is simulated and compared to experimental data. Runs 9 and 10 compare the simulated versus measured melt temperature of a PET resin with intrinsic viscosity of 0.83 dl/g, utilizing a PET screw. A complete analysis for each case is explained later.

Run	Simulated Melt Temperature (°C)	Measured Melt Temperature (°C)
1	241.2	244.2
2	246.5	245.0
3	250.4	253.0
4	256.4	252.8
5	243.6	245.3
6	248.4	245.9
7	253.2	254.1
8	258.3	255.2
9	293.1	299.3
10	304.4	306.4

Table 7: Simulated versus measured melt temperature for Runs 1 to 10 (see Table 5 for reference) at the screw tip

4.1.1 Runs 1 to 4: HDPE Melt Simulation with General Purpose Screw

As indicated in Table 5-Chapter 2, in Runs 1 to 4, an HDPE resin with MFI of 2g/10min was utilized. The barrel heat settings ran at two different levels of 210°C and 230°C and on each level, the screw rotation speed varied from 190 to 286 rpm. The screw utilized in Runs 1 to 4 was a general purpose screw (GP) with L/D ratio of 25 and OD of 80 mm. The experimental results show that increasing the screw speed increases the melt temperature measured in front of the screw, regardless of the barrel heat setting temperature, due to the increased heat of dissipation. In Runs 1 and 2 with the barrel heat set at 210°C, the measured melt temperature increased from 244.2 to 245°C as the screw rotational speed increased from 190 to 286 rpm, respectively. The simulation tool predicted the same trend but slightly different results. The temperature of melt at the screw tip for Run 1, where the screw speed was at 190 rpm with barrel heat setting of 210°C, is simulated at 241.2°C. When the screw speed increases to 286 rpm with the same barrel heat, the simulated melt temperature increases to 246.5°C. In Runs 3 and 4 the barrel heat set changed to 230°C with screw speed changing from 190 to 286 rpm. The experimental results show a higher melt temperature measurement in Runs 3 and 4

compared to Runs 1 and 2 but almost no difference in the melt temperature measurement as the screw speed changes. The melt temperature measured at 253 and 252.8°C as the screw speed increased from 190 to 286 rpm, respectively. The simulation tool predicted that the melt temperature would be at 250.4°C in Run 3, but it would rise to 256.4°C when the screw speed increased to 286 rpm in Run 4. The lower melt temperature measured in Run 4 (although insignificant) shows that direct measurement of melt temperature with a probe is not as robust as expected. Overall, the simulation results are within 2% of the experimental data in Runs 1-4.

The increase in melt temperature by increasing the screw speed (simulated and measured) is theoretically explainable. The effect of screw rotating speed on the melt temperature change was investigated [Sbarski 97, Fischer 97] and it was found that increasing screw rotating speed led to increased heat of dissipation (greater melt temperature rise). This is plausible by the two following reasons:

First, increasing the screw speed led to higher shear heating and thus increased melt temperature. Second, considering the flow patterns for both low and high screw speeds, it was concluded that the total flow length of the circumferential flow in the case of higher screw speed was greater than that of the circumferential flow with lower screw speed due to the larger radius of flow circulation, resulting in higher melt temperature rise for higher screw rotating speed. Increasing screw rotating speed tends to generate a large amount of circumferential flow, implying that the flow length of the circumferential flow has increased, which results in an increase in melt temperature around barrel location. The insignificant temperature difference in the experimental data might have been influenced by non-homogeneity of the melt and the fact that due to polymer's poor heat conductivity, measurement of melt temperature in one location would not reflect the actual melt bulk temperature but only the surface or very small area of the purged melt. Figure 19 depicts the change in the simulated average melt temperature across the screw length from L/D of 8 to the end of the screw for Runs 1 to 4. As summarized in Table 7, the average bulk melt temperature at the screw tip in Run 1 is 241.2°C. HDPE does not require preheating, so the resin enters the section between the screw flights at the feeding

zone at room temperature and rises as the resin is subjected to shear heating and heat conduction from the barrel heating elements. Along Runs 1 to 4, where the common element is utilization of the GP screw, Run 1 holds the lowest average melt temperature because the barrel heat set and screw speed are at their minimum values.

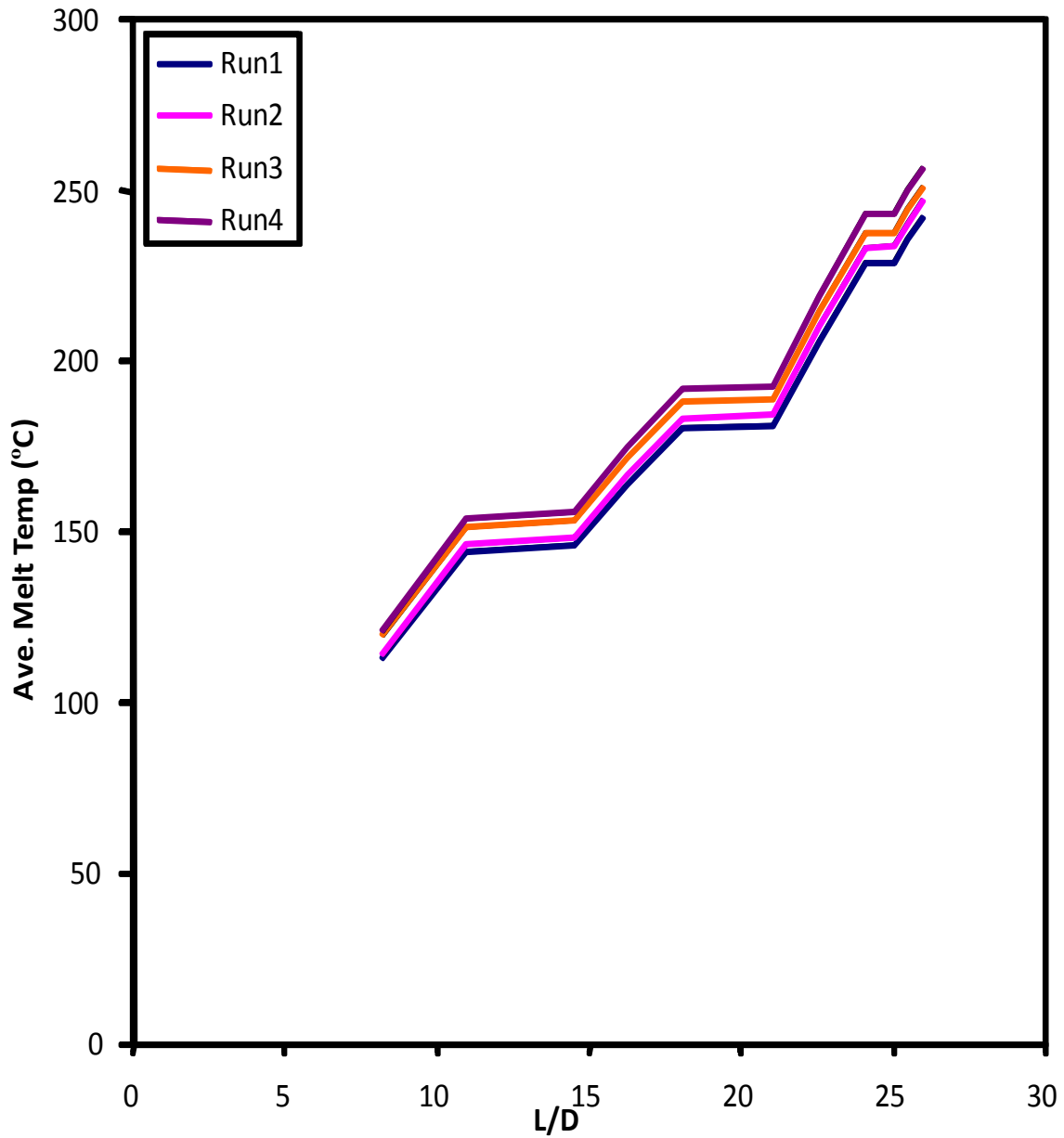


Figure 19: Simulated melt temperature along the length of the extruder for Runs 1-4

For Run 2 the simulated average bulk melt temperature at the screw tip is 246.5°C, which is higher than Run 1 due to the increase in screw speed and subsequently higher shear heating.

In Run 3, the barrel heat is set at 230°C compared to Runs 1 and 2 with 210°C barrel heat. The screw speed is at its lower level (190 rpm). The simulated average bulk melt temperature at the screw tip in this run is 250.4°C. The average simulated bulk melt temperature at the screw tip in Run 4 is 256.4°C. Along Runs 1 to 4, Run 4 holds the highest simulated average melt temperature because the barrel heat set and screw speed are at their maximum values.

The change in the melt temperature profiles for Runs 1-4 depicted in Figure 19 is due to specific design of the general purpose (GP) screw. One important factor in any screw design is to avoid excessive shear heating (also known as overrides) along the length of the screw. The melt temperature rises rapidly while the channel depth is too shallow and eases off to allow the melt to circulate, increase its conductive melting, and cool down and be prepared for the next shearing zone along the screw. At the same time the average melt temperature increases as the melt moves towards the end of the screw but according to the geometry of the screw and the shear heating associated with it. The geometry of the screw will greatly impact the final melt quality at the screw end and can generate either a homogeneous or inhomogeneous melt. As mentioned earlier, due to confidentiality agreements with Husky IMS, the screw design cannot be depicted in this document.

4.1.2 Runs 5 to 8: HDPE Melt Simulation with Barrier Screw

In Runs 5 to 8, the same HDPE resin with the same processing conditions as Runs 1 to 4 was used but the screw type changed to a Barrier screw. Screw designers are constantly asked to improve output quantity without sacrificing quality—or to improve both at the same time. Barrier-type feed screws are the most widely used designs in high-output, high-quality extrusion. In some injection applications, the pressure build-up at the end of the feed section is too high, encouraging wear and tear and impairing the stability of the

process. This can be countered by enlarging the pitch or making the screw channel deeper, although this involves the risk of plasticization and inhomogeneity problems. A better solution than a screw with a stepped pitch or channel depth is a Barrier screw [Fischer 97]. At the beginning of the Barrier plasticization section, the conveying flight changes to a greater pitch; the beginning of the Barrier flight also has a higher pitch. The depth of the channels is adjusted to the desired conveying and melting characteristics. These two measures result in a fairly balanced, low pressure profile, or even in a pressure build-up towards the end of the screw. In Barrier screws the solid material is kept separate from the melt in the melting section (Figure 20).

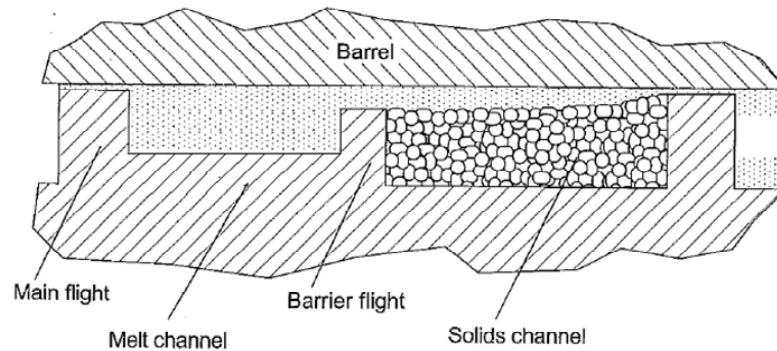


Figure 20: Cross section of a Barrier screw. The solid bed is kept separate from the melt in the melting zone

There are many different versions of this design by virtually all manufacturers and designers, but the basic part of the design is common in all of these versions. In Barrier screws the primary channel width is maintained allowing the Barrier flight and auxiliary channel to be formed with the remaining width. The advantages derived from properly designed Barrier screws are improved rate, better melt temperature distribution, and improved melt quality.

The experimental results show that for Runs 5 and 6, where the barrel heat was at 210 °C, as the screw speed increased from 190 to 286 rpm the melt temperature measured in front of the barrel increased from 245.3 to 245.9 °C, respectively. The simulation software predicted also an increase in the melt temperature from 243.6 to 248.4 °C as the screw speed increased from 190 to 286 rpm in Runs 5 and 6, respectively. In Runs 7 and 8, the barrel heat setting was fixed at 230 °C and the screw speed changed from 190 to 286 rpm.

The melt temperature in Run 7 was measured at 254.1°C and after the screw speed increased to 286 rpm, the temperature increased to 255.2 °C. Logically, the melt temperature is expected to rise as the screw speed increases. The simulation tool predicted a melt temperature of 253.2 °C for Run 7 (barrel heat at 230 °C and screw speed at 190 rpm) and 258.4 °C for the same heat but screw speed of 286 rpm in Run 8. Figure 21 depicts the simulated melt temperature variation across the screw length in Runs 5-8.

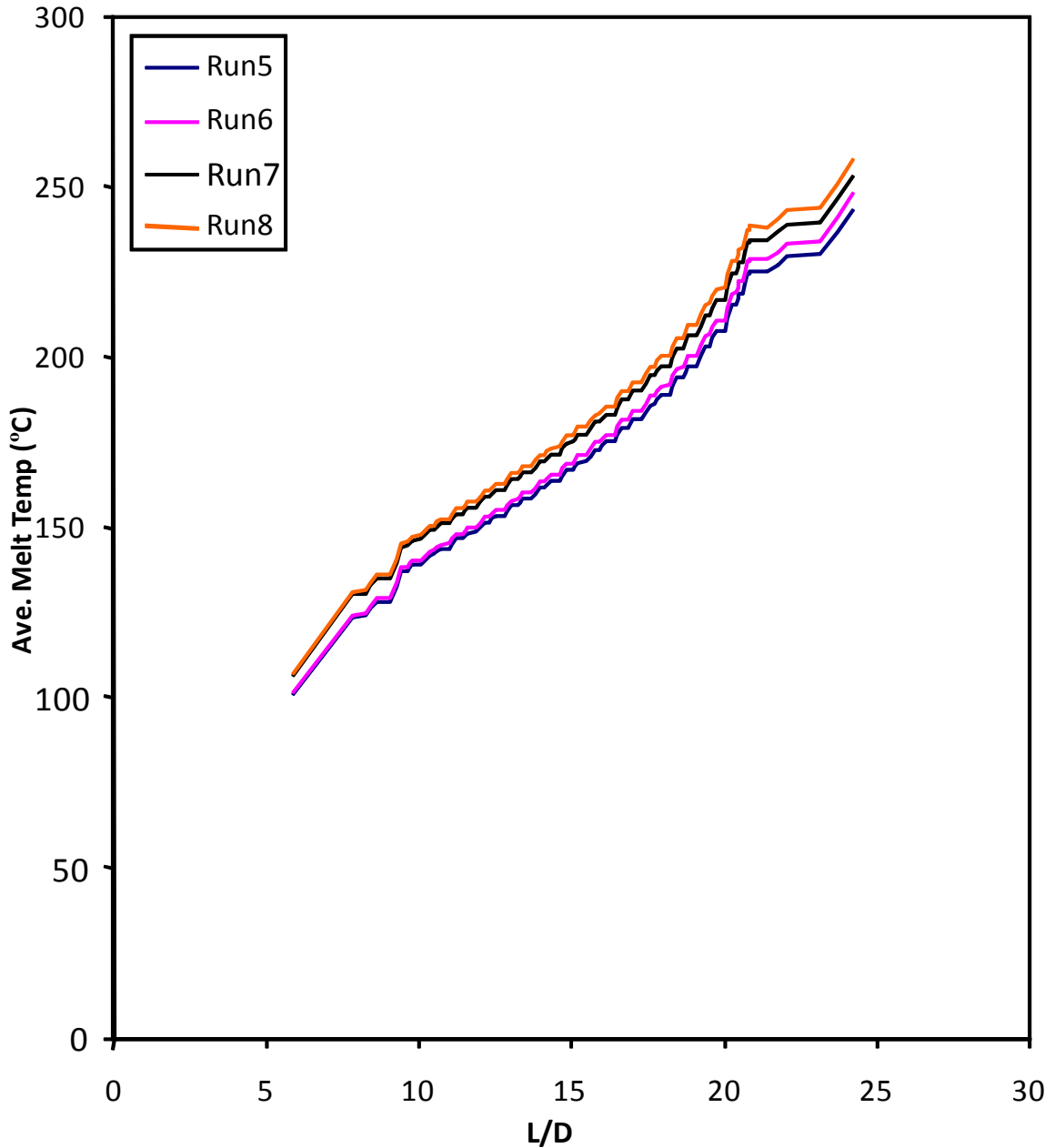


Figure 21: Simulated melt temperature along the length of the extruder for Runs-5-8

As can be seen in Figure 21, the melt temperature profiles in Runs 5-8 are different than the ones in Runs 1-4 with a GP screw. There is no “ease-off” areas in the melt temperature profile with the Barrier screw but the rate of the melting is more gradual than the melting rate with the GP screw. This is related to the specific geometry of the Barrier screw and is explained more in Figure 22.

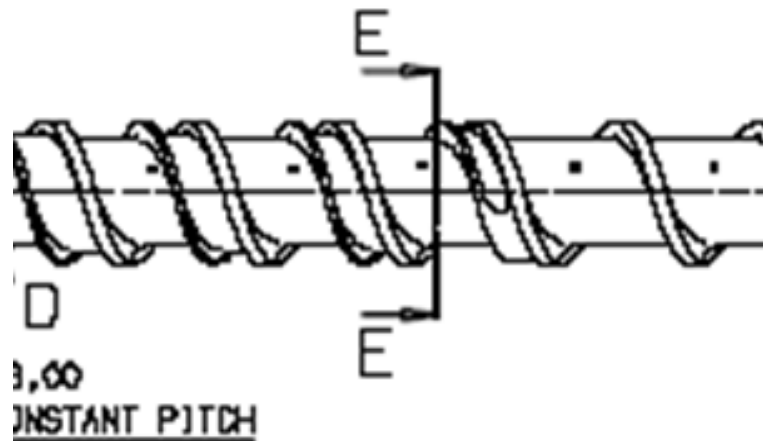


Figure 22: A small section of the Barrier screw utilized in the validation is shown in this figure. The various changes in geometry is done to control the temperature and homogeneity of the final melt.

As can be seen in Figure 22, more modern screw designs (compared to the GP screw) use a Barrier flight. As the melt film is wiped off the barrel surface by the main flight, the melt is deposited into a separate melt channel. A Barrier flight divides the solid and melt channels such that the clearance over the Barrier flight will only allow melt to enter into this channel. The main function of a Barrier flight is to separate the melted polymer from the solid bed and keep the solid bed from becoming unstable and prematurely breaking up. By continuously removing the melt film over the Barrier flight, the solid bed surface remains intact. This allows for a greater solid bed surface area on the barrel wall to keep the viscous energy dissipation via shearing as high as possible. That is why the shear energy is also high. It is believed that this type of phase separation will increase the melting rates as compared to non-Barrier type screws, which is seen in the experimental and simulation results.

Overall, it can be summarized that compared to the GP screw, the melt temperature simulated and measured at the screw tip of the Barrier screw is higher (3 to 4°C), which is expected considering the geometry of the Barrier screw. Also the increase in melt temperature is more gradual in Barrier screw compared to the GP screw, which is also a more desirable property for a given screw design. The simulation results are within 2% of the experimental data, which shows the reliability of the program to simulate melt temperature with different processing conditions and screw designs.

4.1.3 Runs 9 to 10: PET Melt Simulation with PET Screw

In Runs 9 and 10, a PET resin with intrinsic viscosity (IV) of 0.83 dl/g was utilized. The injection unit was integrated with a PET screw and the machine heat setting included two levels of 285 and 300 °C. Figure 23 depicts the changes in the simulated average melt temperature across the screw length for Runs 9 and 10. As mentioned in Table 5, the barrel heat set in Run 9 was 285 °C and due to the shear heating, the actual measured average bulk melt temperature at the screw tip went up to 299.3°C. In Run 10 where the barrel heat was set at 300 °C, the actual measured average bulk melt temperature at the screw tip rose to 306.4 °C, which shows higher than the melt temperature in Run 9 but with less difference to the barrel heat set (6.4 versus 14.3 °C, respectively).

As can be seen in Figure 23, the initial pellet temperature at the entry to the injection unit ($z=0$) is already at an elevated temperature. This, as mentioned previously, is due to the fact that PET needs to be dehumidified before processing to a moisture level of around 50 PPM, otherwise massive drop in final molecular weight is observed.

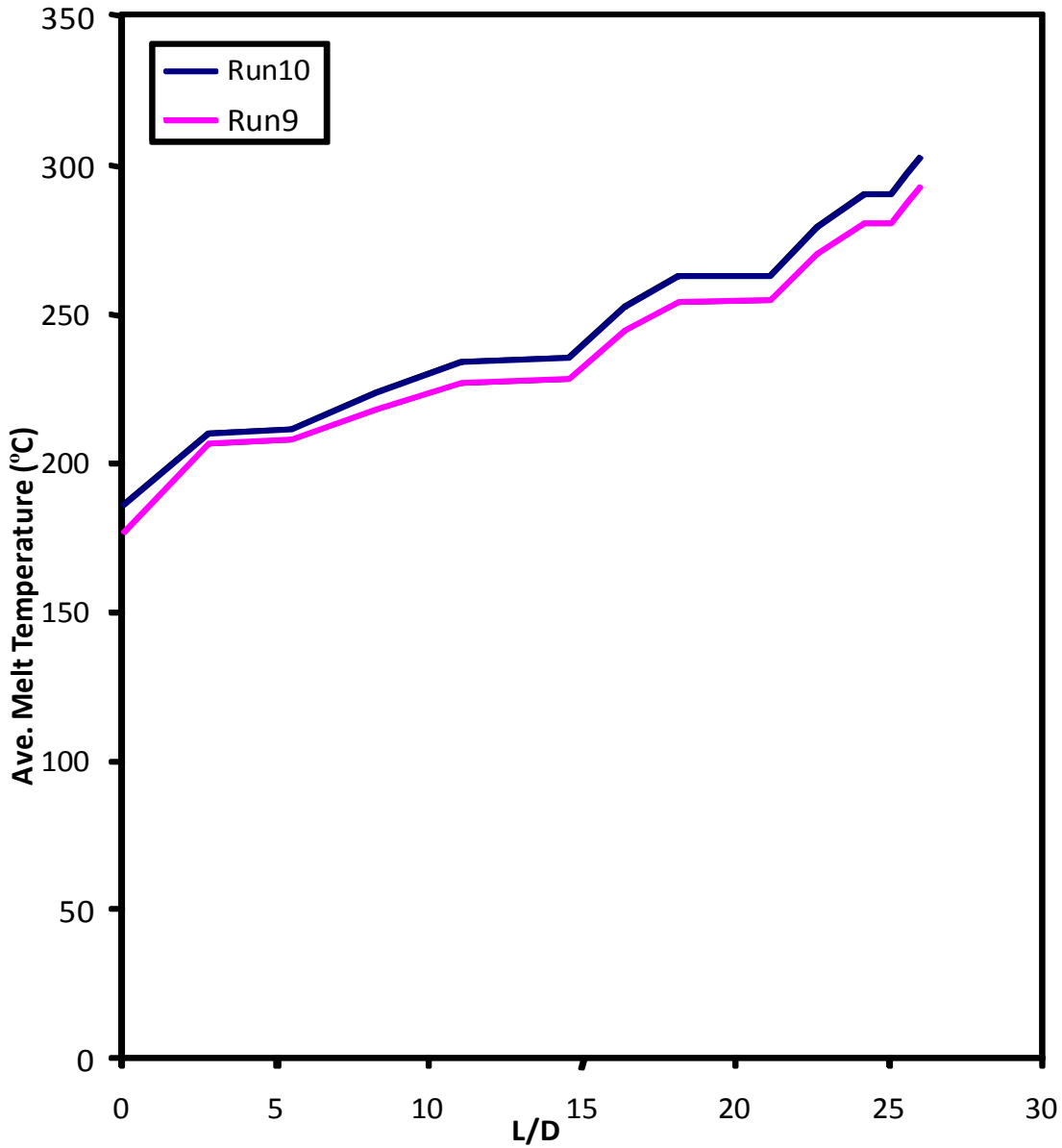


Figure 23: Simulated melt temperature along the length of the extruder for Runs 9-10

In the experimental work, the melt temperature is measured at the screw tip in the machine nozzle, which is the immediate location after the melt exits the injection unit. The melt temperature simulated for the barrel heat set at 285 °C in Run 9 is 293.1 °C, which is about 2% less than the experimental results. As mentioned in the theory, the majority of heat required for melting is supplied by the heat dissipation due to friction

between the screw and resin. This can be understood directly in Run 10 where the barrel heat setting is changed to 300 °C. In Run 10 the melt temperature measured at the screw tip is only 306.4 °C, which has not increased from the set point (300 °C) as much as the melt did in Run 9 when the barrel heat was at 285 °C (Increased to 299.3 °C, which is 6.4 °C increase comparing to 14.3 °C in Run 9). This proves that increasing the barrel heat alone is not the lone source of providing heat to the melt and it has less impact comparing to the screw geometry or increasing/decreasing the friction. The melt temperature simulated for the barrel heat set at 300°C in Run 10 shows close proximity with the experimental data. The simulated melt temperature is 304.4 °C, which compared to the experimental data of 306.4 °C shows a variation of ~2%.

4.2 Melt Pressure During Recovery

Table 8 summarizes the measured versus simulated melt pressure during the screw recovery by the simulation tool in front of the screw tip for Runs 1 to 10. The process engineers are usually interested in the control devices on the injection machines that calculate the melt pressure during injection rather than recovery. The injection pressure proves the capability of the injection unit for injecting a certain plastic object. The melt pressure during injection is the product of hydraulic pressure and machine's intensification ratio and can be calculated with analytical equations. The calculation of melt pressure during injection involves pressure drop (machine pressure minus hydraulic pressure), hydraulic flow (square root of pressure drop times machine's constant), and the injection velocity (hydraulic flow by the bore area). The melt pressure during the recovery is related to the reciprocating plasticizing screw surface area, screw speed, melt viscosity, and its initial backpressure value, while the melt pressure during the injection is related only to the injection piston and machine plunger sizes.

As can be seen in Table 8, it is clear that the Barrier screw generates more plastic pressure during recovery compared to GP screw for Runs 1-8. For one specific screw design, as the screw rotational speed increases, the melt pressure in front of the screw tip during the recovery also increases.

Run	Simulated Melt Pressure at screw tip (psi)	Measured Melt Pressure at screw tip (psi)
1	1844.8	1882.8
2	2263.4	2311.0
3	1771.5	1805.2
4	2173.4	2216.4
5	1961.0	2004.1
6	2405.9	2456.4
7	1883.1	1918.8
8	2310.3	2356.5
9	824.7	842.8
10	578.7	587.4

Table 8: Simulated versus measured melt pressure (see Table 5) during recovery for Runs 1 to 10

4.2.1 Runs 1 to 4: HDPE Melt Pressure Simulation with GP Screw

For Runs 1-8, as depicted in Table 5, the screw backpressure was set at 754 psi. In Runs 1 and 2 with barrel heat at 210°C, the simulated melt pressure during recovery increased from 1844.8 to 2263.4 psi as the screw speed increased from 190 to 286 rpm, respectively. In Runs 3 and 4 with barrel heat at 230°C, the melt pressure simulated during screw recovery increased from 1771.5 to 2173.4 psi as the screw speed increased from 190 to 286 rpm, respectively. Figure 24 depicts the simulated melt pressure variation during recovery for Runs 1-4. As can be seen, the lowest pressure build up during recovery belongs to Run 3 where the barrel heat is at the higher level (230°C) and the screw speed is at the lower level (190 rpm). In all cases in Figure 24, the pressure initially shows a rapid increase, which is due to the solid conveying that causes an exponential pressure growth in the feed region. It is then followed by steady pressure increase through the remainder of the feeding zone. The pressure rise will slow down (but still on the rise) along the transition and compression zones of the screw. Somewhere in the metering zone, a massive pressure drop is observed leading to the final screw backpressure. Comparing the high and low barrel temperature, the lower

barrel heat causes increase in melt pressure during recovery, which moves against the final throughput of the injection unit.

The maximum measured melt pressure during screw recovery in Runs 1-2 are within ~2% from the simulated results. The maximum measured melt pressure during screw recovery in Runs 3-4 are also within ~2% from the simulation results, which shows the capability of the simulation tool to predict reliable melt pressure during recovery.

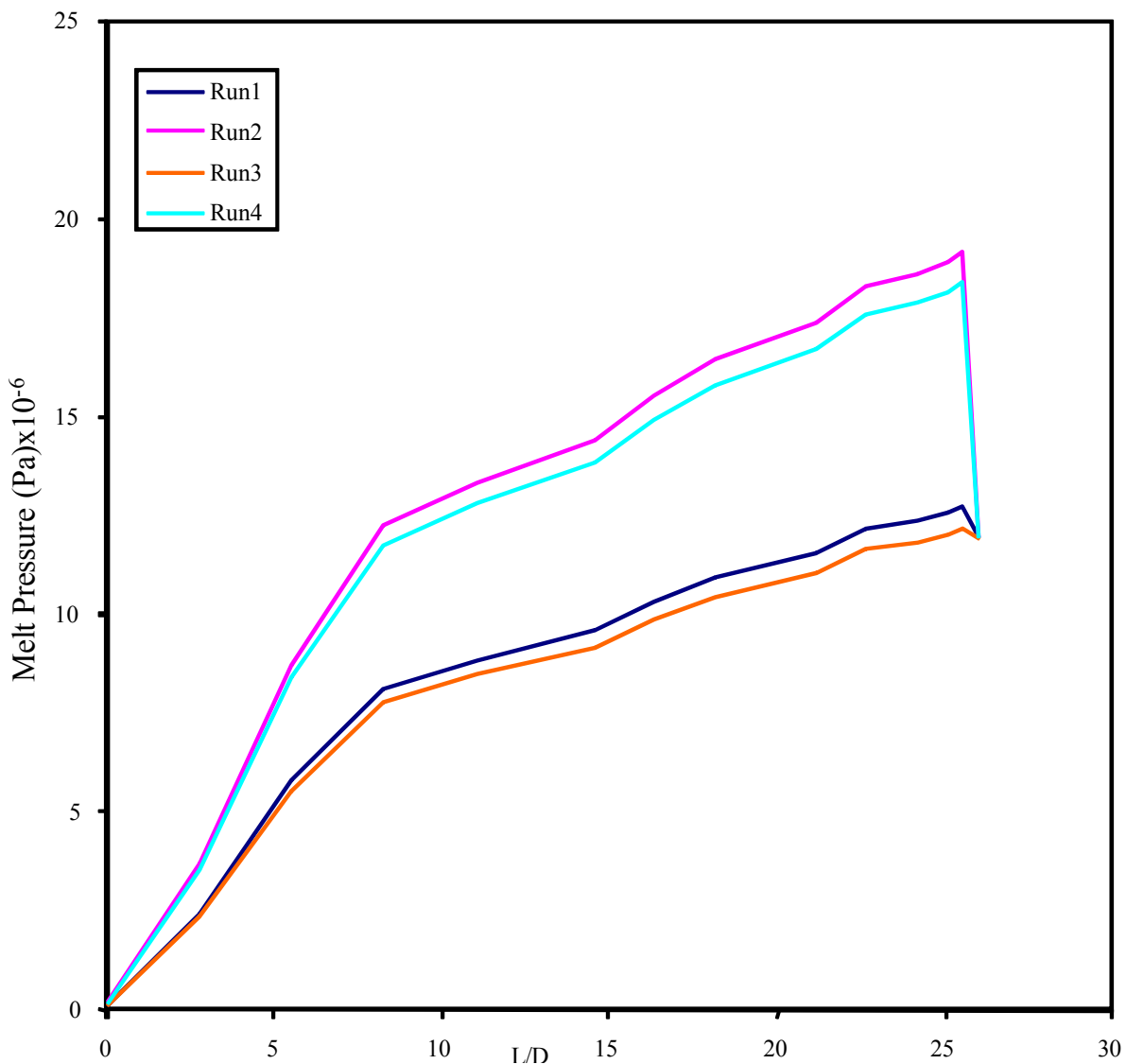


Figure 24: Simulated melt pressure during screw recovery along the length of the screw for Runs 1-4

From the pressure simulation results for Runs 1-4 it can be concluded that as the temperature of the melt increases, its pressure during the recovery decreases. Although a desired condition, there should be a balance between the final melt pressure during the recovery and melt's final temperature. Higher melt temperature usually leads to some thermal degradation and generation of unwanted chemicals that might require additional operations to be removed from the melt (e.g. Acetaldehyde, which causes odors and require expensive scavengers to get rid of). Also it can be concluded that at constant barrel temperature, the melt pressure increases along the length of the extruder as the screw rotational speed increases.

4.2.2 Runs 5 to 8: HDPE Melt Pressure Simulation with Barrier Screw

For Runs 5-8 the screw was replaced with a Barrier screw for better melting and less wear. All processing conditions are similar to Runs 1 to 4. Figure 25 depicts the melt pressure variation during recovery for Runs 5-8. As can be seen, the melt pressure gradient increases along the length of the extruder as the screw rotational speed increases. The lowest pressure build up during recovery belongs to Run 7 where the barrel heat is the highest, (230°C), and the screw speed is the lowest, (190 rpm). Compared to Runs 1-4 with a general purpose screw (GP screw), the initial pressure build up is faster in Barrier screws and shows a more rapid increase in the feeding zone but for the remainder of the screw length, the melt pressure is more steadily increasing. The advantage of the Barrier screw over the GP screw is the amount of pressure buildup at the end of the feeding zone. The simulation results show that the pressure at the end of feeding zone for the runs with GP screw is lower than the runs with Barrier screw (i.e. 1103.2 psi in Run 1 versus 1124.1 psi in Run 5). The higher pressure at the end of feeding zone but more steadily increasing in the melting and metering zones will lead to reduction of wear and tear and impairing the stability of the process.

In summary, the melt pressure during recovery for Run 5 at the screw tip is 1961.0 psi, which compared to Run 1 that has the same processing conditions, is ~100 psi higher. In Run 6, the barrel heat is still at 210°C but the screw speed has increased from 190

rpm to 286 rpm. The simulated melt pressure during recovery for this run is 2405.9 psi, which first, is higher compared to Run 2 with the same processing conditions, and second, is the highest within Runs 5-8. The reason is due to higher screw speed and at the same colder barrel heat set.

In Run 7 the barrel heat set is increased to 230°C and the screw speed is set at 190 rpm. The melt pressure during recovery has dropped to 1883.1 psi, which is the lowest melt pressure within Runs 5 to 8. Run 7 holds the highest barrel heat set (subsequently highest melt temperature) and lowest screw rpm.

In Run 8, the barrel heat set is still at 230°C but the screw speed is changed back to 190 rpm. The simulated melt pressure during recovery for this Run is 2310.3 psi.

The maximum measured melt pressure during screw recovery in Runs 5-8 at the screw tip are within ~2% from the simulated values, which again illustrates the accuracy of the simulation tool in predicting the final melt pressure during recovery.

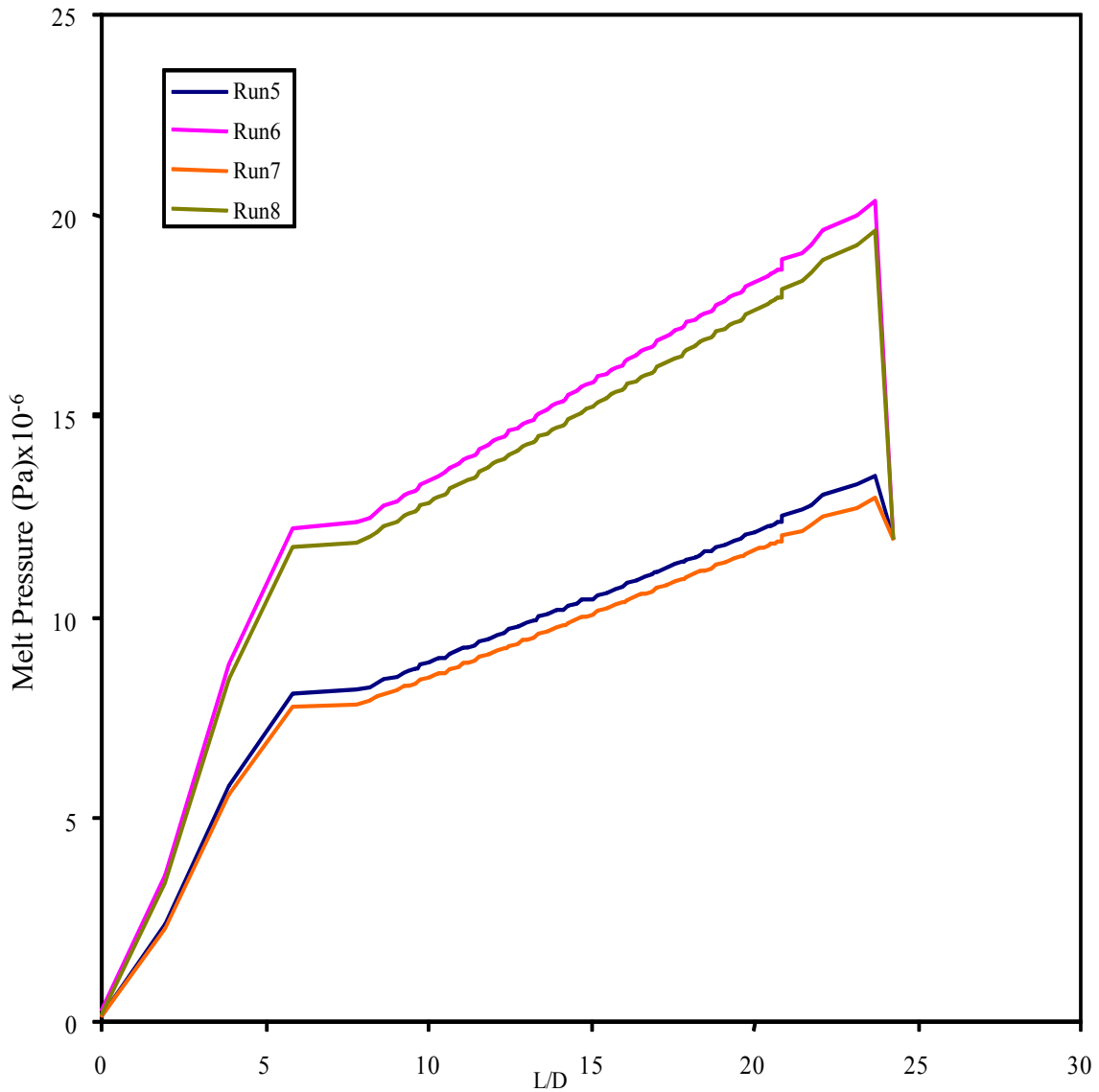


Figure 25: Simulated melt pressure during recovery along the length of the extruder for Runs 5-8

In injection molding, understanding of pressure readout during recovery would enable the screw performance to be more accurately described. Melt pressure during recovery can be correlated to the recovery time of the screw, which is also an indication of screw performance. A properly designed screw will generate proper melt pressure at the end of recovery and eliminates screw recovery time variation.

4.2.3 Runs 9 to 10: PET Melt Pressure Simulation with PET Screw

In Runs 9-10, the screw backpressure was set at 300 psi with two barrel heat setting of 285 and 300 °C, respectively. Figure 26 compares the simulated melt pressure variation during recovery for Runs 9 and 10 with the PET screw. As can be seen, the simulated melt pressure during the recovery at 285 °C barrel heat is greater than the simulated melt pressure during recovery at 300 °C in Run 10. This concludes that higher temperature setting of the barrel heat contributes to lower pressure build-up during the screw recovery. At 285 °C the melt pressure simulated during recovery was 824.7 psi and it decreased as expected to 578.7 psi as the barrel heat increased to 300 °C.

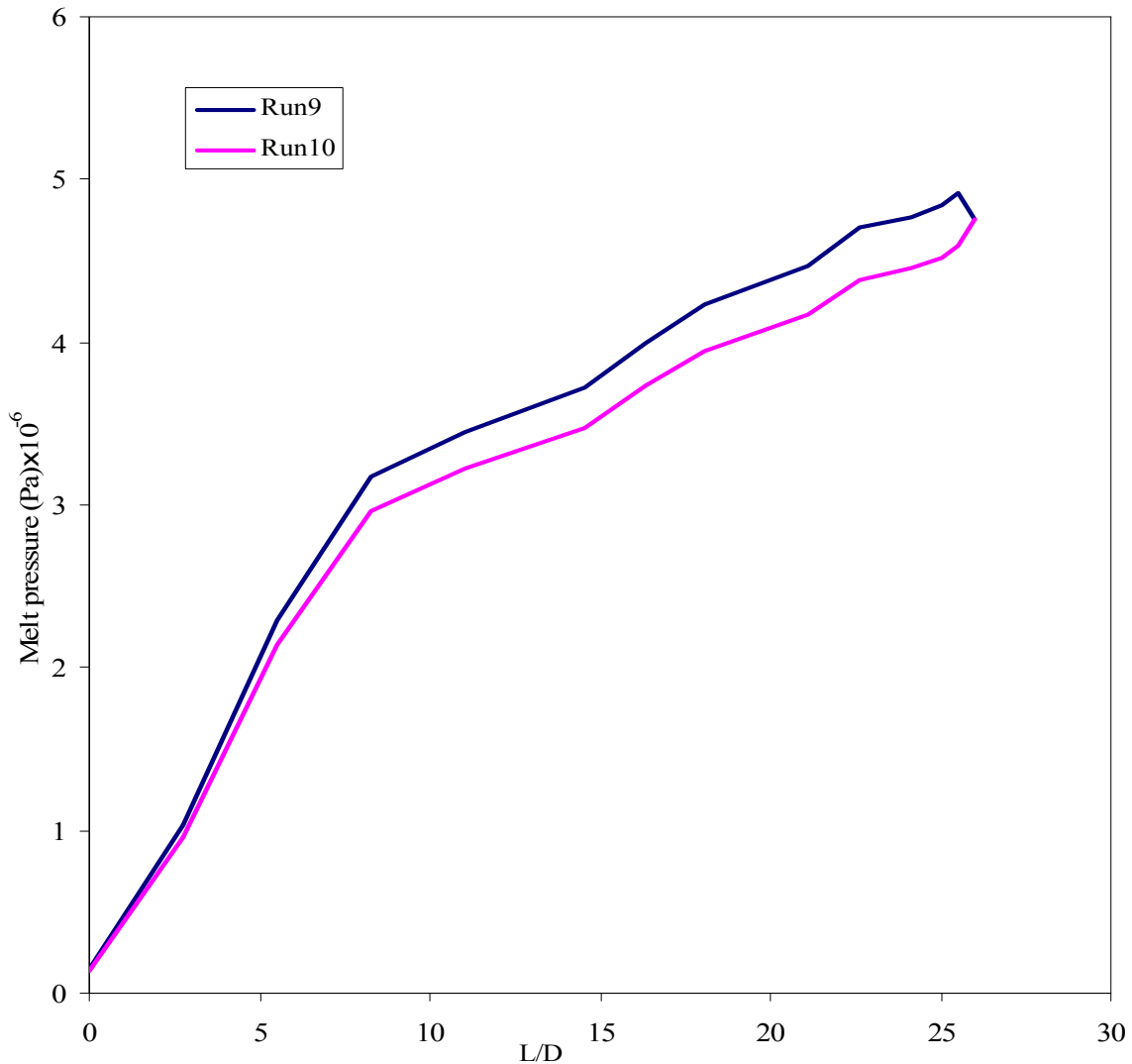


Figure 26: Simulated melt pressure during recovery along the length of the extruder for Runs 9 and 10

4.3 Recovery Rate

The recovery rate is calculated using the melt velocity and the metering zones surface area of the screw. In the simulation tool, the melt velocity profiles at the metering zone is calculated by the momentum equations and subsequently the final recovery rate in helical coordinates is computed according to the following equation:

$$\text{Recovery Rate} = \iint V_z(a + bz) \frac{rsk_4}{\sqrt{k_4^2 + r^2}} \, drd\theta \quad (4.152)$$

Table 9 summarizes the recovery rate results for Runs 1 to 10 and compares the prediction results with the experimental data.

Run	Simulated recovery rate (kg/h)	Measured recovery rate (kg/h)
1	422.2	440.7
2	635.6	639.2
3	422.7	440.7
4	636.3	644.5
5	437.1	449.5
6	657.1	651.2
7	437.1	449.2
8	657.2	655.8
9	1000.8	1012.3
10	1006.6	1014.0

Table 9: Simulated versus measured recovery rate (see Table 5) for Runs 1 to 10

As can be seen, the simulated recovery rates for different Runs in Table 9 are very close to the experimental results ($\pm 4.2\%$). Barrier screws (Runs 5-8), are higher in the recovery rate for a given processing condition than the GP screw (Runs 1-4) due to the generation of more heat, which was explained in melt temperature comparison earlier.

4.4 The Screw “L/D”

Often screw length is referenced to its diameter as L/D ratio. The L/D ratio is a major factor in the effectiveness of the extruder and of the types of material that it can process. For most extruder types, the L/D ratio has increased as technology has advanced. The limitation to high L/D ratios is the torque available from the motor (longer screws mean higher friction) and the capacity of the thrust bearings of the extruder. As mentioned earlier, at some point inside the barrel, the melt average bulk temperature will reach minimum desirable melt processing temperature. From that location forward, the melt temperature keeps rising and holds its processing quality unless its temperature rises up to a point that would cause resin degradation. The program predicts the required screw length (L/D) for melting of a specific resin. Table 10 summarizes the simulated L/D requirements for the resin and processing conditions in Runs 1 to 10.

Experiment	Simulated L/D
1	24.54
2	20.94
3	23.05
4	20.17
5	23.56
6	19.97
7	22.95
8	19.04
9	22.44
10	21.29

Table 10: Simulated L/D for Runs 1 to 10

As can be seen, for GP screw (Runs 1 to 4), the lowest L/D belongs to the case where the screw speed and barrel heat are at higher levels. As explained earlier, higher shear heating generation plus more conduction through barrel contributes to higher melt temperature and subsequently lower L/D requirements. The highest L/D belongs to Run 1

where the barrel heat and the screw speed are at their lower level. This means that it takes more time for the resin to be melted to the minimum resin processing temperature requirement.

For the Barrier screw (Runs 5 to 8), the same rule is followed as for the GP screw with the difference that this screw has a better melting capability and requires less L/D in general for melting compared to the GP screw. For the PET screw, the L/D requirements reduced as the barrel heat increased from 285 to 300°C due to better conduction cooling.

4.5 Viscosity

As mentioned previously, Cross-WLF model is employed in the simulation tool to predict the gradient of viscosity along the extruder length as the temperature of the plastic resin rises. In this section the simulation results for the viscosity gradient along the screw length for each run is illustrated and in some cases compared with the data provided by the resin suppliers. Table 11 illustrates the viscosity simulation data at the tip of the screw for Runs 1 to 10. The related melt temperature for the final viscosity is also shown.

Run	Simulated viscosity (Pa.s)	Simulated melt temperature (°C)
1	331.7	241.2
2	322.6	246.5
3	317.2	250.4
4	293.9	256.4
5	327.4	243.6
6	315.7	248.4
7	304.3	253.2
8	281.3	258.3
9	529.7	293.1
10	502.6	304.4

Table 11: Simulated viscosity values for Runs 1 to 10. The resin in Runs 1-8 is HDPE, while in Runs 9-10 PET resin has been used.

In Runs 1 to 4, HDPE resin was utilized under different processing conditions resulting in different final melt temperature and pressure. Figure 27 depicts the changes in the viscosity for Runs 1 to 4 across screw length. In Runs 1 and 2 the barrel heat set is at 210°C but the screw speed is higher in Run 2 (286 versus 190 rpm). In Runs 3 and 4 the barrel heat set is at 230°C and like Runs 1 and 2, two sets of screw speed is used (286 rpm in Run 4 versus 190 rpm in Run 3).

In Runs 1 and 2 the viscosity at the screw tip is simulated at 331.7 and 327.6 Pa.s, respectively. In Runs 3 and 4 the final viscosity at the same location is lower compared to Runs 1 and 2 due to higher melt temperature and stands at 317.2 and 293.9 Pa.s, respectively. The final melt temperature related to each run is also depicted on Figure 27.

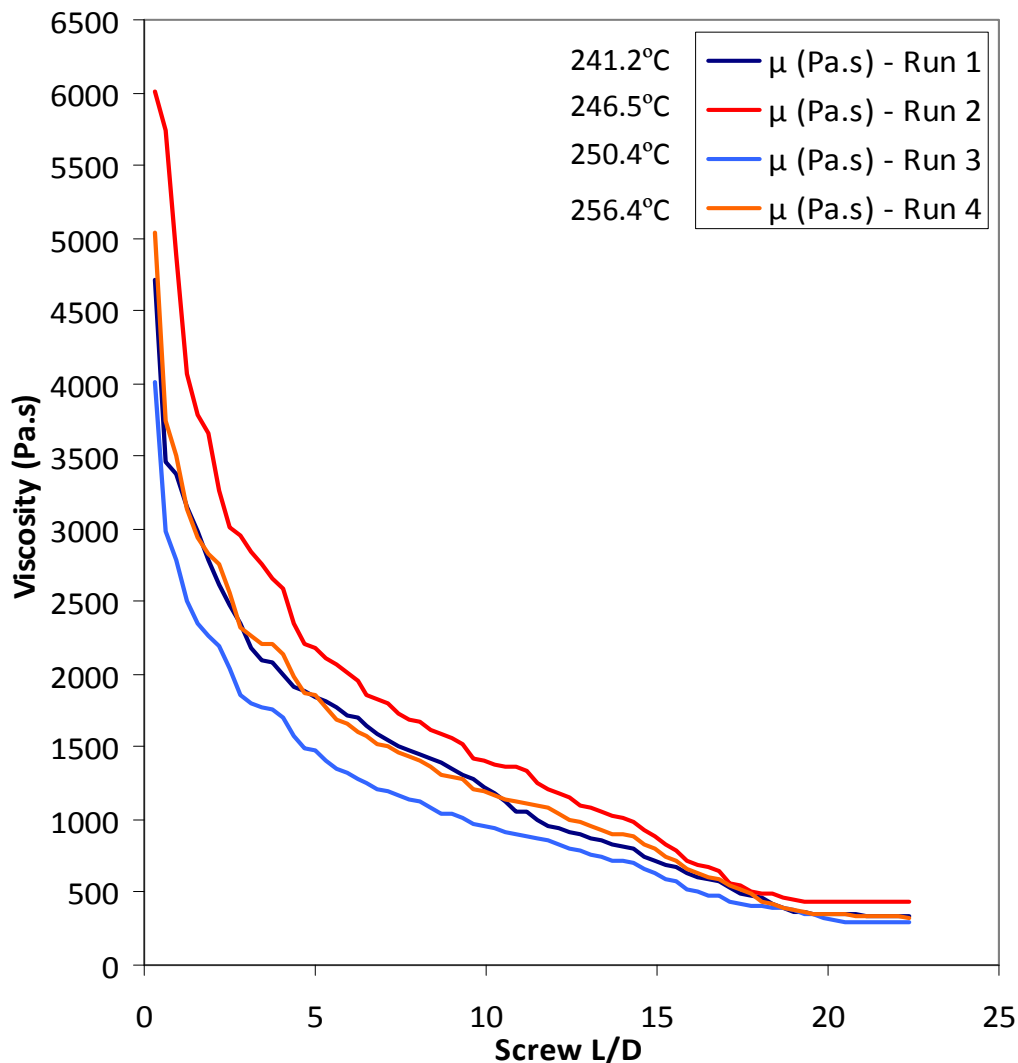


Figure 27: Simulated melt viscosity gradient along the length of the extruder for Runs 1-4

Figure 28 plots simulated melt viscosity versus simulated melt temperature for Runs 1 to 4. Some resin suppliers provide viscosity data with respect to melt temperature, which is particularly useful when different grades of plastic resins are compared. Continual control and monitoring melt viscosity during the process is also important to the throughput of a system. At higher melt temperature the melt viscosity is lower so throughput of the system increases.

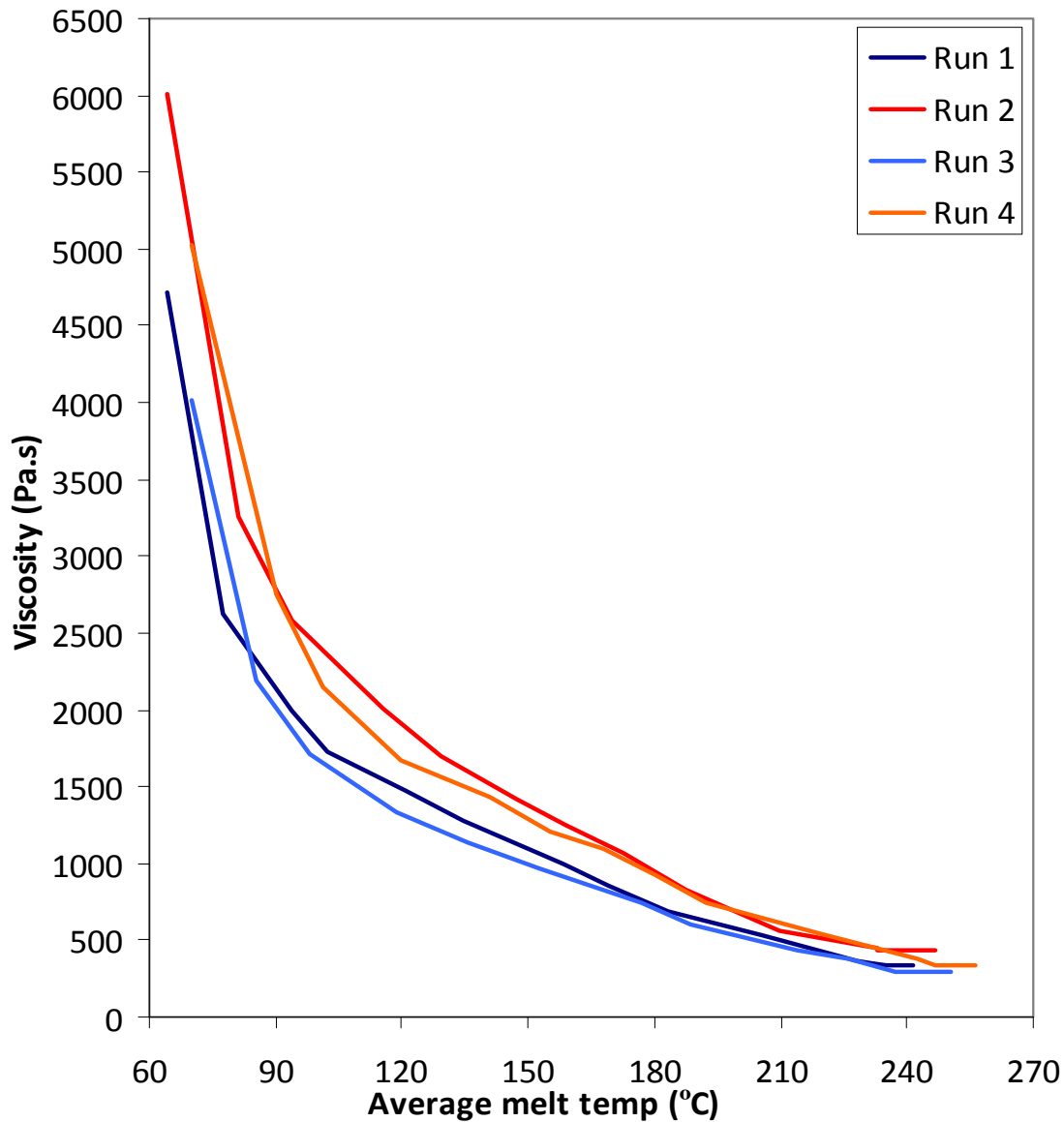


Figure 28: Simulated viscosity data versus melt temperature for Runs 1 to 4

Figure 29 depicts the viscosity versus temperature curve provided by the resin manufacturer (BP SOLVAY Eltex) for the HDPE resin (MFI of 2 g/10min), which is determined at constant rotor speed of 190 rpm.

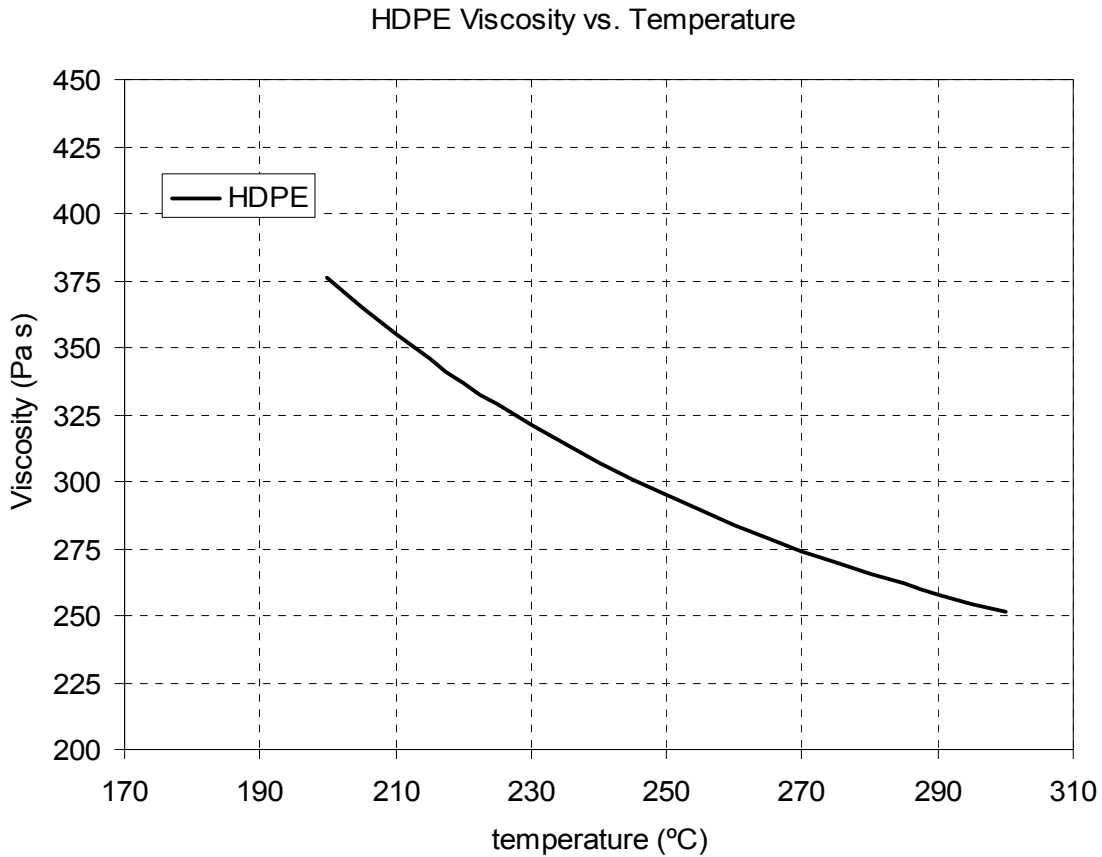


Figure 29: Viscosity curve for HDPE with MFI of 2g/10min

The data to generate the Run 1 and Run 3 curves in Figure 27 is collected at the screw speed of 190 rpm. The viscosity values in Figure 29 at 241°C and 250°C melt temperatures are 314 and 286.7 Pa.s, respectively, which are in good agreement with the simulation results (331.7 in Run 1 and 317.2 Pa.s in Run 3).

Figure 30 depicts the change in the melt viscosity with respect to screw L/D for Runs 5 to 8. In Runs 5 and 6 the barrel heat set is at 210°C with higher screw speed in Run 6 (286 versus 190 rpm). In Runs 7 and 8 the barrel heat set is at 230°C and the screw speed is 286 rpm in Run 8 versus 190 rpm in Run 7. In Runs 5 and 6 the viscosity at the screw tip is simulated at 327.42 and

315.7 Pa.s, respectively. In Runs 7 and 8 the viscosity at the screw tip is lower compared to Runs 5 and 6, which is due to higher melt temperature (304.3 and 281.3 Pa.s, respectively). In Figure 30 the melt temperature associated with each run is also depicted.

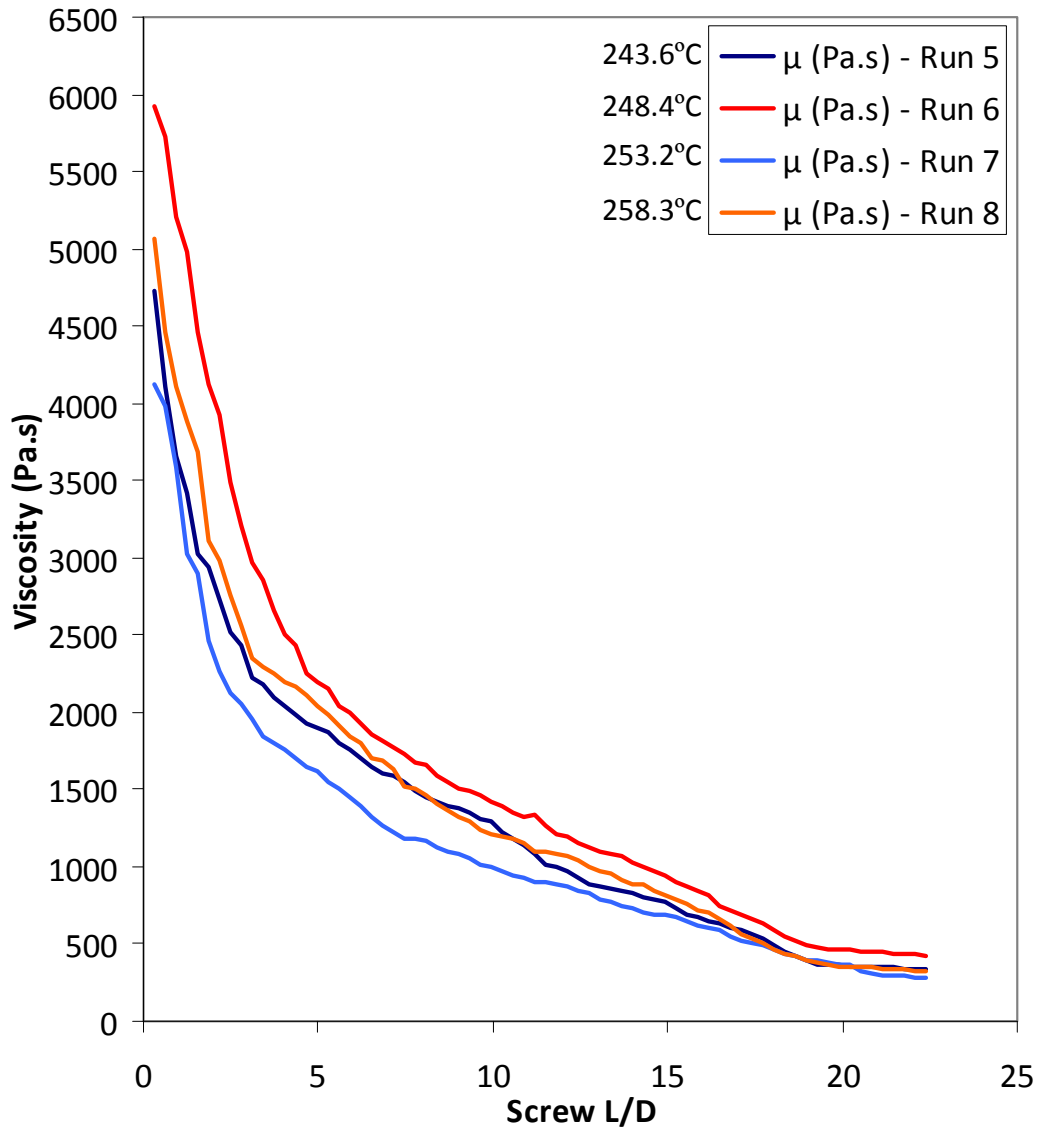


Figure 30: Simulated melt viscosity gradient along the length of the extruder for Runs 5-8

In general, Runs 5 to 8 contain more final melt temperature than Runs 1 to 4. The reason, as mentioned earlier, is because of utilization of the Barrier screw. In turn the simulated viscosity is also exhibiting slightly lowers values compared to Runs 1-4 with the same processing conditions.

Figure 31 depicts the simulated melt viscosity versus simulated melt temperature for Runs 5 to 8.

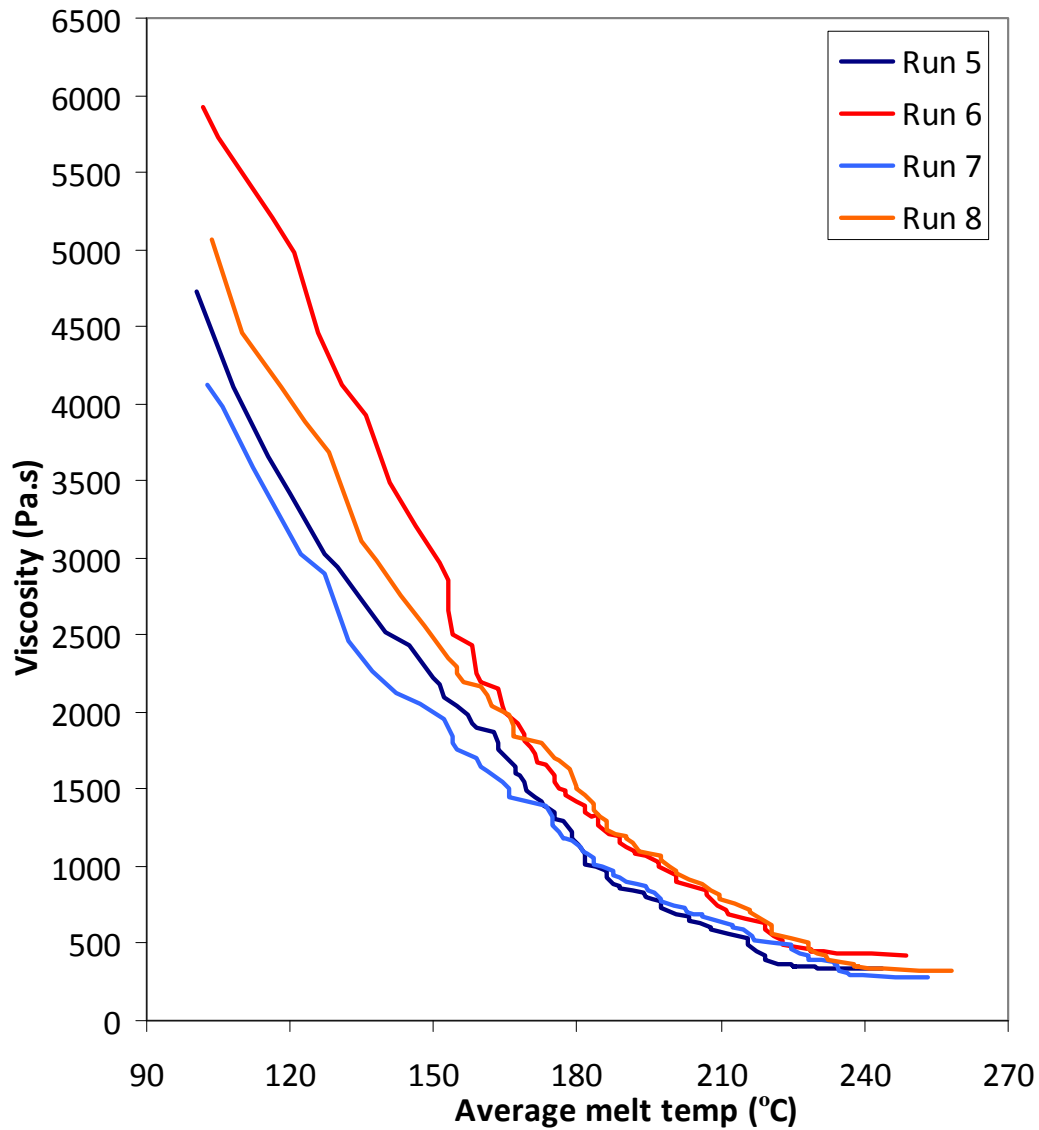


Figure 31: Simulated viscosity data versus melt temperature for HDPE (Runs 5-8)

As can be seen, the melt viscosity reduces with increasing the average temperature. Above about 240°C, increasing the melt temperature will impact the viscosity significantly.

Figure 32 depicts the change in the viscosity for Runs 9 and 10 with respect to L/D of the screw. In Run 9, the barrel heat set is at 285°C compared to 300°C in Run 10. All other processing conditions are unchanged.

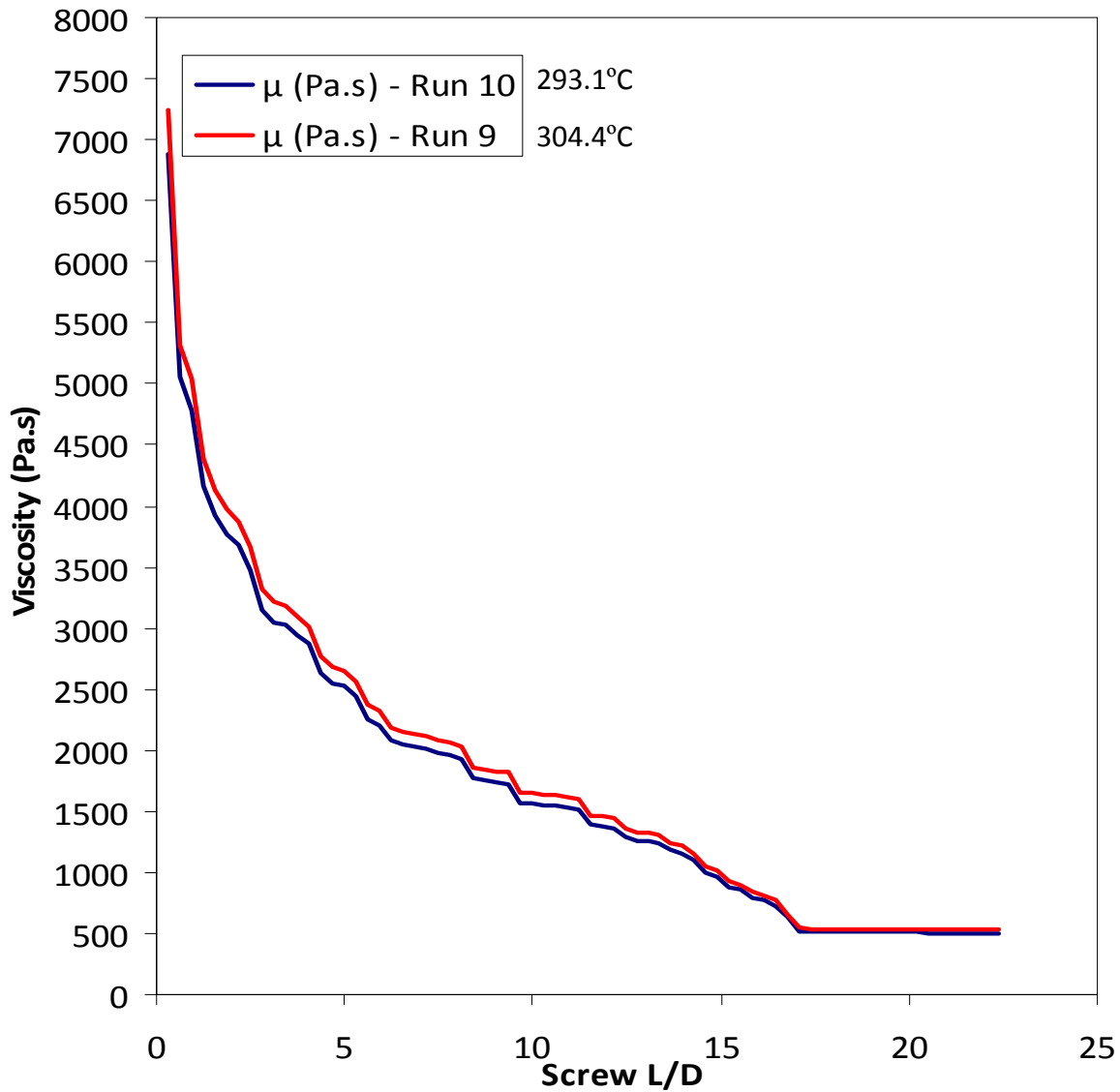


Figure 32: Simulated melt viscosity gradient during recovery along the length of the extruder for Runs 9-10

The simulated final viscosity in Runs 9 and 10 is 529.7 and 502.6 Pa.s, respectively. Higher viscosity in Run 9 is due to lower melt temperature (293.1°C compared to 304.4°C in Run 10). Figure 33 plots the change in the resin viscosity as the melt temperature rises along the screw length in Runs 9 and 10.

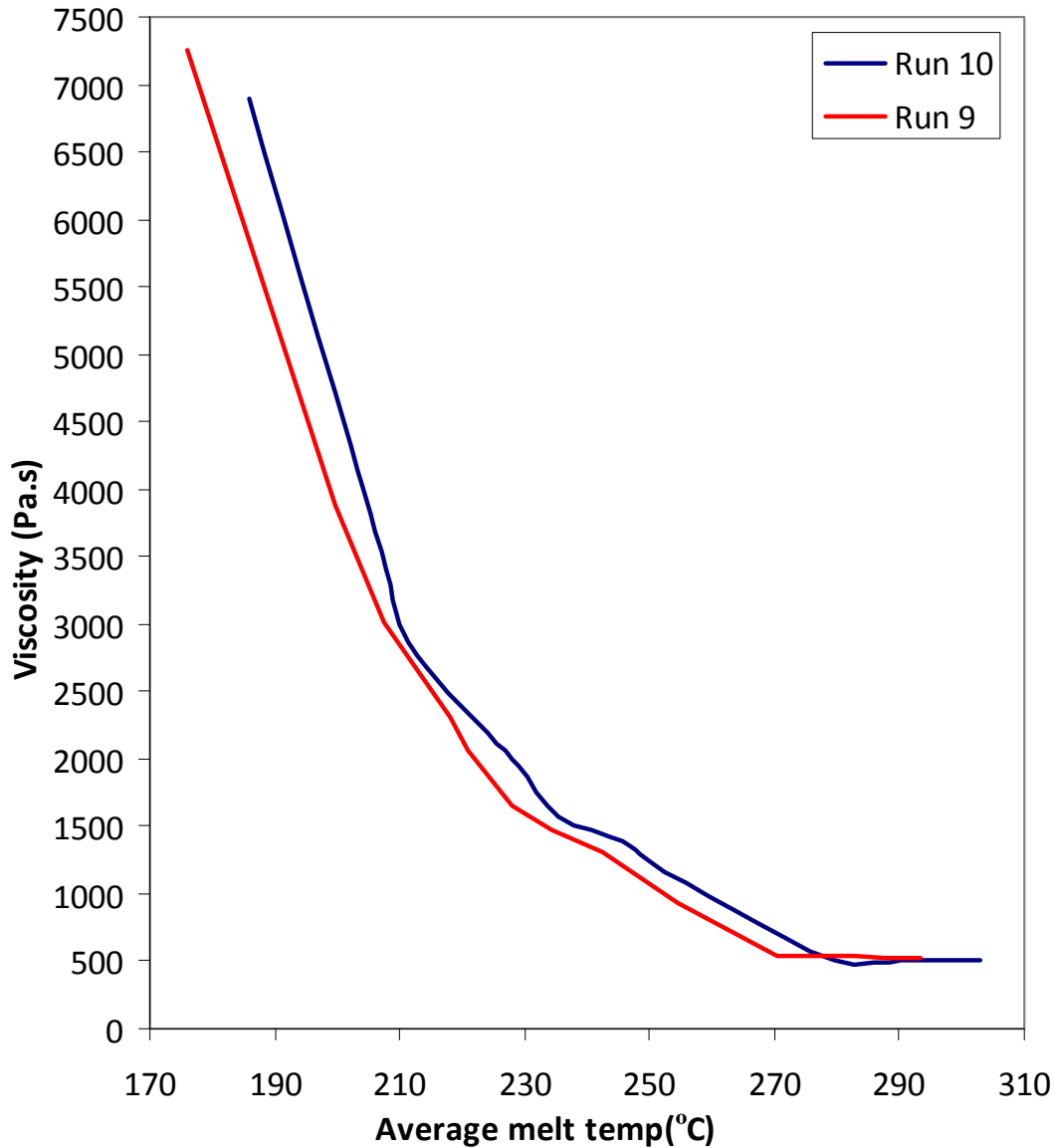


Figure 33: Simulated viscosity data versus melt temperature for Runs 9-10

As can be seen, at some point during the melt temperature rise, which is normally above the suggested melting point of the polymer, increasing melt temperature further will not impact the viscosity significantly. The reason is because all polymer chains are now melted and the polymer has reached its minimum achievable viscosity. Table 12 depicts the viscosity data provided by the PET resin manufacturer (INVISTA). At the shear rate and temperature corresponding to the processing conditions used for the simulation, (26.1 s^{-1} and 290°C respectively), the actual melt viscosity is $507.2 \text{ Pa}\cdot\text{s}$, which shows a 5% deviation from the simulated value ($529.7 \text{ Pa}\cdot\text{s}$).

	PET Nominal IV: 0.83					
	Viscosity data at 270°C		Viscosity data at 290°C		Viscosity data at 305°C	
	Shear rate (s ⁻¹)	Viscosity (Pa.s)	Shear rate (s ⁻¹)	Viscosity (Pa.s)	Shear rate (s ⁻¹)	Viscosity (Pa.s)
1	26.1	545.55	26.1	507.20	26.1	478.80
2	31.5	502.95	31.5	446.68	31.5	352.55

Table 12: Viscosity data for PET resin used in Runs 9 and 10. Shear rates are measured using Gottfert Rheograph 2003 Capillary Rheometer based on ASTM D3835

4.6 Torque

In this section a comparison between the screw torque measured in the experiments and predicated by the simulation tool is explained. Regardless of the details of the screw geometry, it is important that the screw has sufficient mechanical strength to withstand the stresses imposed by the conveying process in the extruder. The most critical area of the screw regarding the required torque is in the feed section, where the cross sectional area of the root of the screw is the smallest and, thus, the torsional strength the lowest [Rauwendaal 86].

The screw torque requirement is actually the power needed to rotate the screw. The amount of this power depends on the screw design, the type and viscosity of the resin, and also the amount of the melt needed for a specific process. The screw torque can be simulated by calculating the shearing force at the melt interface with the barrel. A common practice exists in the polymer industry for calculating torque values for a specific polymer. An approach based on experimental and practical experience is used to calculate plasticizing torque, which is based on scaling up from small size screws with known torque requirements. The scaled-up rules are aimed at subjecting the melt to a similar degree of shear thus keeping the same levels of melt temperatures [Darnell 56].

From empirical measurement and screw manufacture's point of view, the screw torque can be calculated from the following equation:

$$\text{Torque} = \frac{0.9 \times \text{Displacement}[\text{cc} / \text{rev}] \times \text{Extruder pressure} [\text{psi}]}{20 \times \pi} \quad (4.153)$$

Where 0.9 is the motor efficiency (assumed 90%), displacement is hydraulic motor piston oil displacement per revolution of motor, given by the motor nameplate referencing hydraulic specifications for the motor, and extruder pressure is the motor pressure measured with a gauge on a port on the motor itself or at the extruder manifold gauge port.

From the analytical point of view the screw torque is calculated by total shear stress in the shaft resulting from torque, which occurs at the circumference ($r=R$) by the following equation [Rauwendaal 86]:

$$\tau_{\max} = \frac{\pi \times R^3 \times \eta \times \sqrt{r \frac{d}{dr} \left(\frac{V_{\theta}}{r} \right)^2 + \left(\frac{dV_z}{dr} \right)^2 + \left(\frac{dV_r}{dr} \right)^2}}{2} \quad (4.154)$$

In order to avoid failure in the screw shaft, the resulting screw torque from the simulation must be less than the allowable torque of the metal of the screw (given by the screw manufacturer). Table 13 compares the simulated and measured plasticizing screw torque for Runs 1 to 10.

Run	Simulated torque (Nm)	Measured torque (Nm)
1	4488.40	4402
2	4923.10	4874
3	4265.06	4239
4	4661.78	4656
5	4443.9	4402
6	4880.93	4874
7	4236.10	4239
8	4625.48	4656
9	8930.12	8803
10	8120.41	8085

Table 13: Simulated versus measured screw torque for Runs 1 to 10

As can be seen in Table 13, the simulation results are within 2% of the actual test data. Also it can be concluded that the torque demand for the plasticizing screw increases as the screw speed increases. In Runs 1 and 2 the simulated screw torque for plasticizing increased from 4488.4 to 4923.1 Nm as the screw speed increased from 190 to 286 rpm. The same trend can be observed in other runs. The torque demand in Runs 3 and 4 increased from 4265.06 to 4661.78 Nm due to increase in screw speed from 190 to 286 rpm. The barrel temperature has the opposite effect compared to the screw speed. As the barrel heat increases the torque demand for plastication decreases. In Runs 3 and 4 the simulated screw torque for plasticizing are lower compared to Runs 1 and 2 due to higher barrel heat set (230°C). In Runs 5 and 6 with the Barrier screw, the simulated screw torque for plasticizing increased from 4443.9 to 4880.93 Nm as the screw speed increased from 190 to 286 rpm. The torque demand in Runs 7 and 8 increased from 4236.10 to 4625.48 Nm due to increase in screw speed from 190 to 286 rpm, respectively. In Runs 7 and 8 the simulated screw torque for plasticizing are lower compared to Runs 5 and 6 because of the higher heat set, which was mentioned earlier for Runs 1-4. In Runs 9 and 10 with the PET screw, higher barrel heat reduced the plasticizing torque demand. In Run 9 the simulated screw torque requirement is 8930.12, which is about 9% higher compared to simulated screw torque with increased barrel heat to 300°C.

4.7 Power

Plastic processing machines, especially for injection molding machines, comprises hydraulic pump, drives and machine control. To provide an economical injection molding machine, the machine consumes an optimized power needed for the different components mentioned. The classic approach to calculating the power, which is the starting point of this work, has been through a torque balance for the screw multiplied by screw speed. Table 14 illustrates the screw power consumption for Runs 1 to 10.

Run	Simulated Screw Power Consumption (kW)
1	89.30
2	147.45
3	84.86
4	139.62
5	88.42
6	146.18
7	84.28
8	138.53
9	280.55
10	255.11

Table 14: Simulated screw power consumption for Runs 1 to 10

For Runs 1 to 4, where a GP screw is used, the highest screw power usage belongs to Run 2 with higher screw speed and lower barrel heat set. The lower barrel heat generates higher screw torque, which in return consumes more power. In Run 1 with 210°C barrel heat and 190 rpm screw speed, the screw power consumption is 89.30 kW, which rises to 147.45 kW in Run 2 where the screw speed increased to 286 rpm. In Run 3 the screw speed is set back at 190 rpm but the barrel heat increased to 230°C. As a result the power consumption by the screw dropped to 84.86 kW, which is the lowest among Runs 1 to 4. In Run 4 the screw speed increased to 286 rpm with the barrel heat still at 230°C and subsequently the power consumption increased to 139.62 kW. The same trend can be observed in Runs 5 to 8 with the Barrier screw. In Run 5, the barrel heat and screw

speed are at 210°C and 190 rpm, respectively and the screw power consumption is 88.42 kW. In Run 6 the screw consumes 146.18 kW power, which is the highest among Runs 5-8 since it has the highest screw speed and lowest barrel heat set. In Run 7 the screw power consumption is only 84.28 kW due to highest barrel heat and lowest screw speed. In Run 8 the screw speed raised to 286 rpm while the barrel heat set remained unchanged at 230°C. As a result the screw power consumption increased to 138.53 kW. In Runs 9 and 10 the resin is changed to PET and proper screw is employed. Due to high screw speed (300 rpm) and high screw torque during recovery the power consumption is much higher than cases with polyolefin resin. In Run 9 the screw power consumption is 280.55 kW. In this test the barrel heat was at 285°C and the screw speed at 300 rpm. After increasing the barrel heat to 300°C the screw power consumption dropped to 255.11 kW due to decrease in amount of torque needed to turn the screw.

4.8 Sensitivity Analysis: Grid size change in the helical coordinate

Accuracy of the system behavior for any given process largely depends on the initial input values and process parameter changes inside the system. It is prudent to appreciate that the significant changes in the system behavior do not occur for all changing parameters. In general, some systems are actually insensitive or at least have very low sensitivity to many parameter changes [Barton 02, Breierova 01]. It is the structure of the system, and not the parameter values that has the most impact on the behavior of the system.

Overall, one strives to obtain information from the system with a minimum of physical or numerical experiments. That is why simulation tools are designed so instead of interacting with a real system, one creates a model which corresponds to the system in certain aspects. A common use of sensitivity analysis is to reveal the invalidity of a model by demonstrating that the results are fragile with respect to the initial model setting, assumptions, structure, etc. The same concept is expressed by Jerome Ravetz [Ravetz 07], for whom ineffective modeling is when uncertainties in inputs must be suppressed lest outputs become indeterminate. The understanding of how models behave in response to changes in its inputs is of fundamental importance to ensure a correct use of

the models. By showing how the model behavior responds to changes in parameter values, sensitivity analysis is a useful tool in model building as well as in model evaluation. In sensitivity analysis, by showing that the system does not react greatly to a change in a parameter value, it reduces the modeler's uncertainty in the behavior of the model.

In mathematical modeling and simulation, some of the influencing parameters are associated with the numerical algorithm [Cunha 94, Cunha 99] (e.g., the grid size in tangential, helix and normal directions), while others are coupled with the process variables including the polymer thermo-physical properties (e.g. polymer heat capacity and thermal conductivity). In sensitivity analysis, the effect of varying those influencing parameters of the mathematical model on the output of the model is observed.

In this section, we evaluate the sensitivity of the simulation results to changes in the number of the grid sizes for selected runs of the DOE (Runs 1, 5, and 9). We are determined to evaluate the impact of parameter changes on specific responses including final recovery rate, melt temperature, and screw torque.

Parameter sensitivity is usually performed as a series of tests in which the modeler sets different parameter values to see how a change in the parameter causes a change in the dynamic behavior of the results. Perhaps one of the most common areas of interest, while walking the path to simulate a mathematical model is to evaluate the impact of the grid sizes on the accuracy of the final simulation results and the system behavior. The use of a larger number of grid sizes will usually lead to higher accuracy in the final results. However, this is achieved at the expense of exponentially larger computation time, which in turn is not desirable. In order to obtain a reasonable accuracy along with practical computation time, careful balance between the two is required, which is achieved by a reasonable selection of the numerical grid sizes. Table 5 in Chapter 2 depicted the experimental design originally used for the purpose of validation of the simulation results. Two sets of polymer resins along with three sets of screw designs were used in the experiment while the processing conditions including barrel heat and screw speed varied for each run. Runs 1, 5, and 9 from Table 5 are selected for the purpose of the sensitivity analysis and establishing the impact of the number of the grid sizes on the final simulation results. As depicted

in Table 15, the sensitivity of the final simulation results with respect to ten different sets of grid points sizes, which are applied to all the axes, is evaluated.

Run number	Number of grid points		
	Normal (N_r)	Tangential (N_θ)	Helix (N_z)
1	2	2	2
2	3	3	3
3	4	4	4
4	5	5	5
5	6	6	6
6	7	7	7
7	8	8	8
8	9	9	9
9	15	15	15
10	20	20	20

Table 15: Number of grid points used in the sensitivity analysis

As mentioned earlier, the responses to the changes in the number of grid points are selected to be the final recovery rate, melt temperature at the screw tip, and screw torque. Figures 34 to 36 show the variation of the final melt temperature, recovery rate, and screw torque with respect to changes in the grid points in Run 1. The relative differences of the simulation responses to the experimental baseline values are also depicted on those figures.

In this work, it is assumed that if changes in the input parameters selected in the sensitivity study alter the experimentally validated simulation results for more than 5%, those results are undesirable. Figure 34 depicts that the final simulated melt temperatures with less than 4 grid points along θ and r directions are about 7 to 9% less than the experimentally validated simulation results. In Figure 35, the simulated recovery rate with 2 and 3 grid points in angular and radial directions is 8.5 and 15% less than the experimentally validated recovery rate. Finally in Figure 36, the screw torque has been overestimated for up to 15%, when the number of grid points have been less than 4 in radial and angular directions.

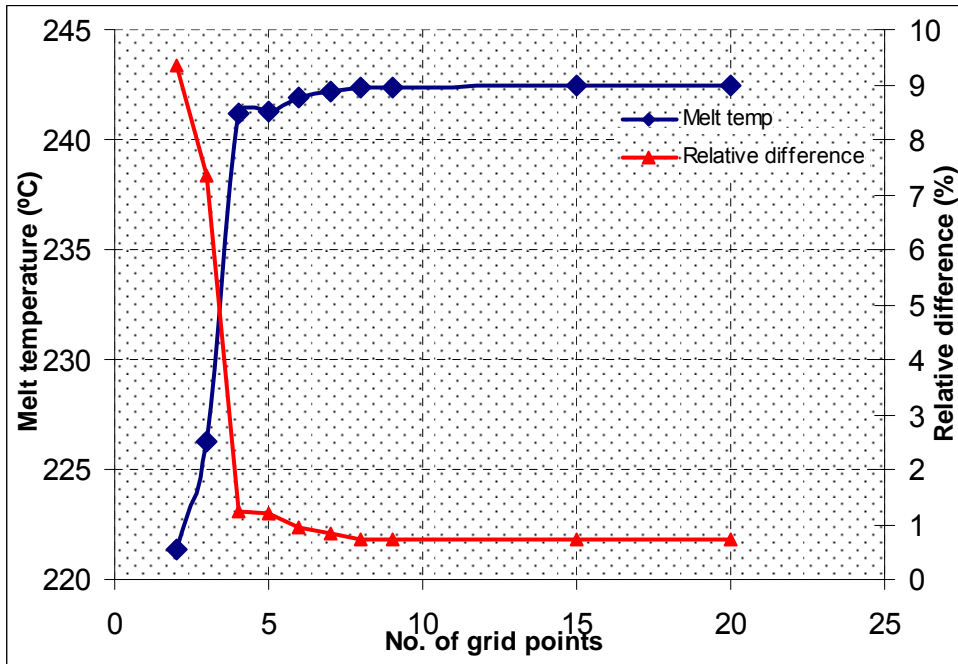


Figure34: Variation of melt temperature versus different number of grid points as well as their relative differences to the benchmark data (Run 1)

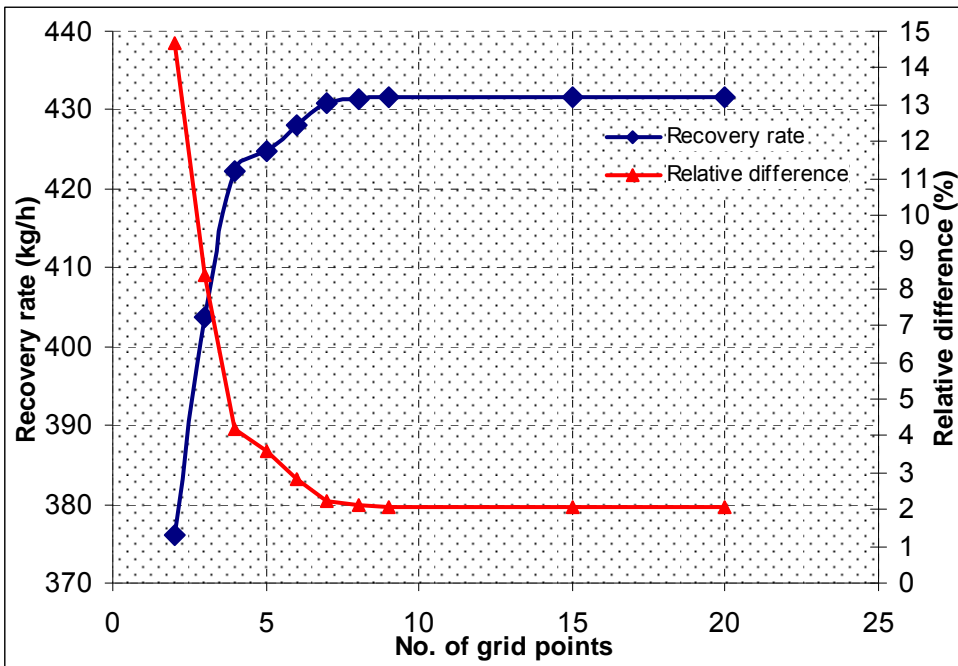


Figure 35: Variation of recovery rate versus different number of grid points as well as their relative differences to the benchmark data (Run 1)

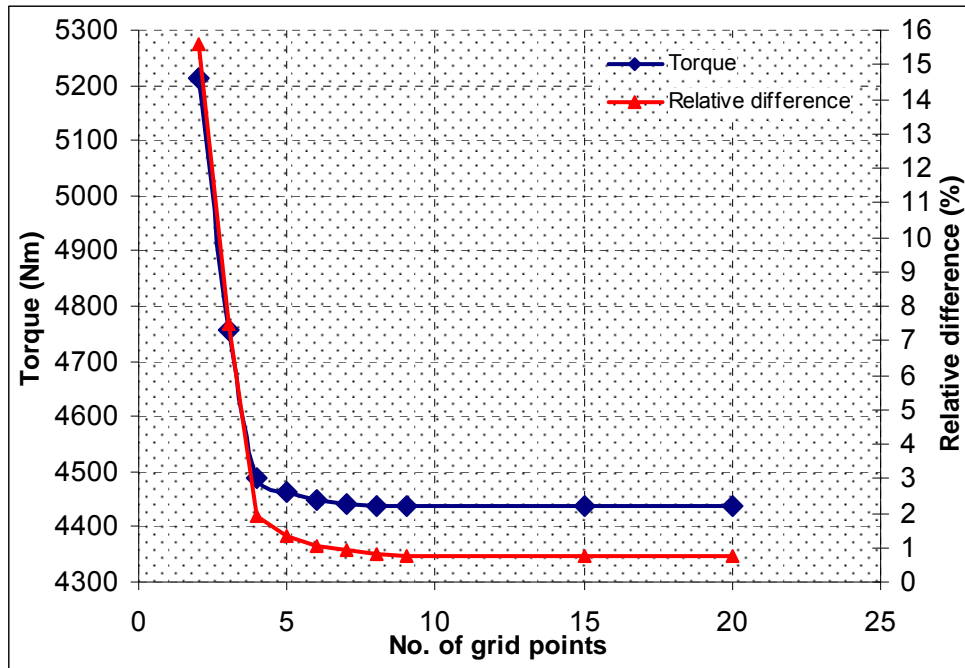


Figure 36: Variation of screw torque versus different number of grid points as well as their relative differences to the benchmark data (Run 1)

Overall in Figures 34 to 36, results obtained with less than 4 grid points for all three parameters show major variation between the simulation and baseline results (beyond 5%). Results obtained with 4 to 8 grid points show reasonable improvement as the number of grid points increase. Above 8 grid points the relative differences do not show any major improvement as the number of grid points increase and the actual value of the parameter remains unchanged. The computation time for grid point above 8 is significantly higher (more than 96hrs for 9 grid points, 192hrs for 15 grid points, and 2 weeks for 20 grid points comparing to average 18hrs for 4 to 8 grid points). The results also depicts the sensitivity of the simulation tool to changes in the number of grid points.

Figures 37 to 39 show the variation of the final melt temperature, recovery rate, and screw torque versus various grid points and the relative difference of the responses to the experimental values in Run 5.

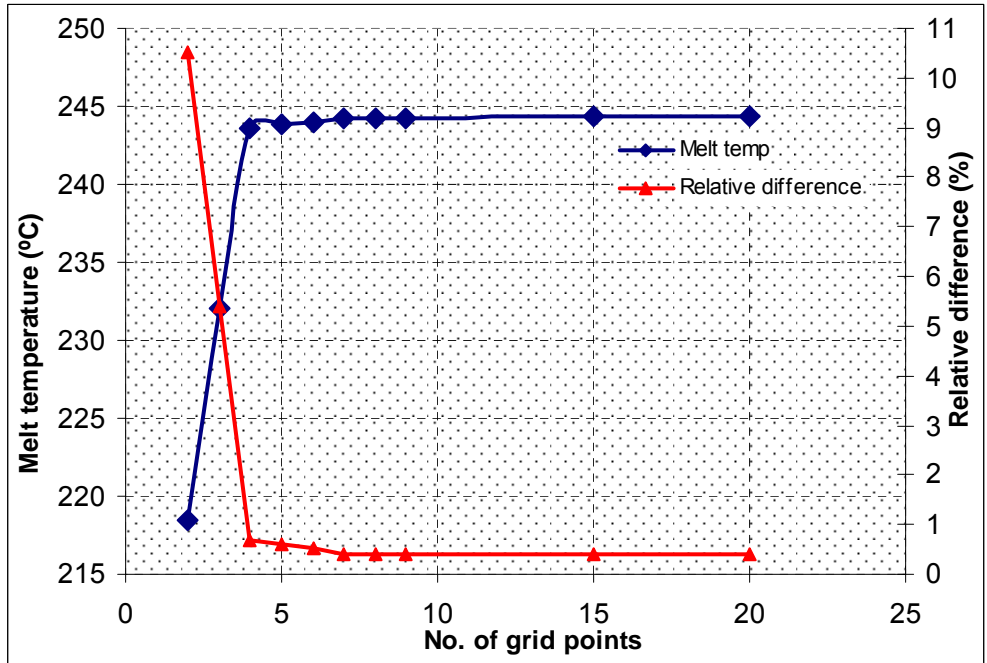


Figure 37: Variation of melt temperature at the screw tip versus different number of grid points as well as their relative differences to the benchmark data (Run 5)

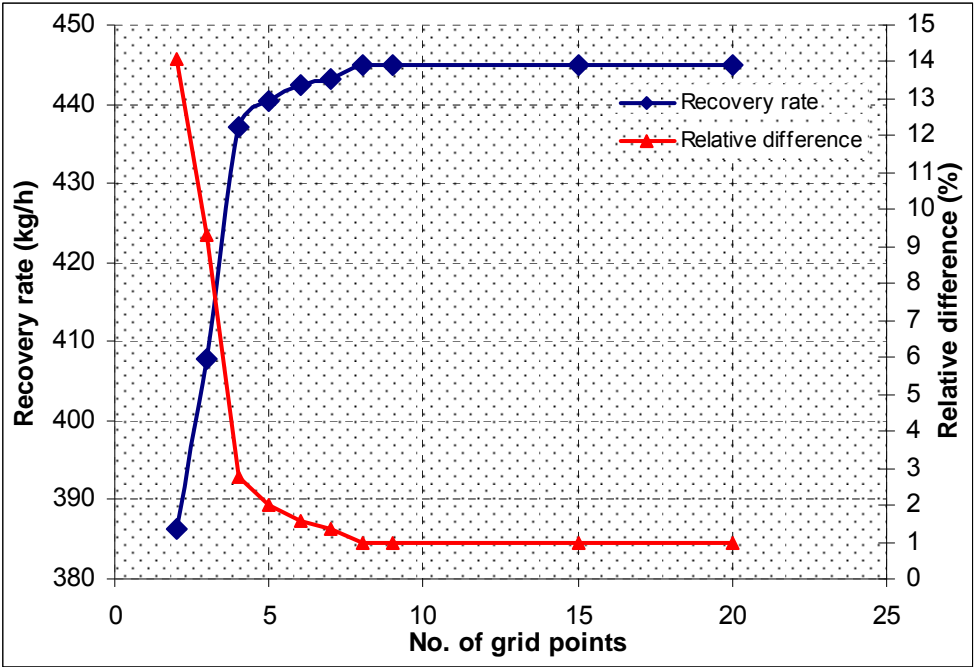


Figure 38: Variation of recovery rate versus different number of grid points as well as their relative differences to the benchmark data (Run 5)

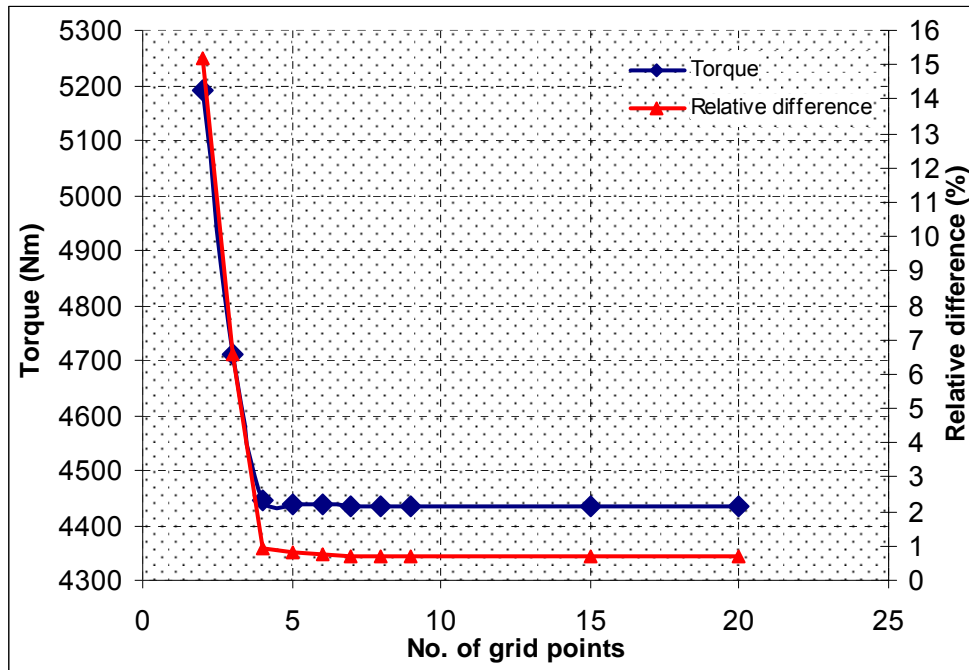


Figure 39: Variation of screw torque versus different number of grid points as well as their relative differences to the benchmark data (Run 5)

The same conclusion as Run 1 can be drawn for Run 5. As can be seen, simulation results obtained with less than 4 grid points are beyond the 5% limit selected in this work. Results obtained with 4 to 8 grid points are within the 5% limit from the experimental data with practical computation time, while above 8 grid points there is no further improvement in the simulation results while the computation time is greatly increased.

Figures 40 to 42 show the variation of the final melt temperature, recovery rate, and screw torque versus various grid points in Run 9, where a PET resin with specially designed PET screw was utilized. As mentioned previously, due to confidentiality agreements with Husky IMS, the details of the screws cannot be shown in this thesis. The relative difference of the responses to the experimental values with varying grid points show that the maximum allowable of 5% variation is not within the reach with less than 4 grid points in θ and r directions. Beyond the 4 grid points, the accuracy of the results seems to be practical only up to 8 grid points. Grid sizes larger than 8 not only do not improve the accuracy of the simulation, but also greatly impact the computation time, which is undesirable.

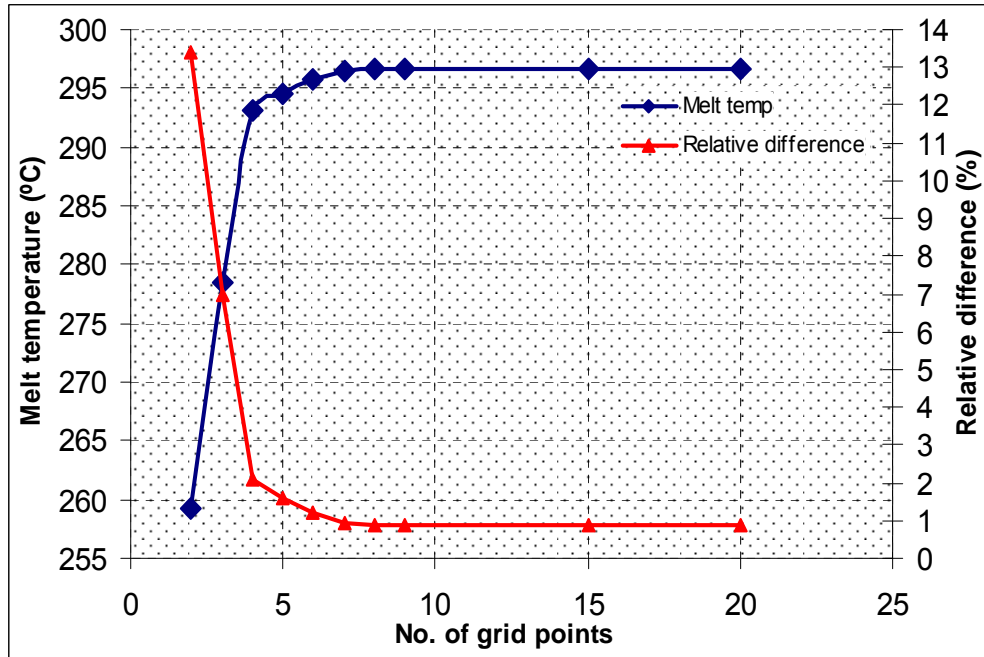


Figure 40: Variation of melt temperature at the screw tip versus different number of grid points as well as their relative differences to the benchmark data (Run 9)

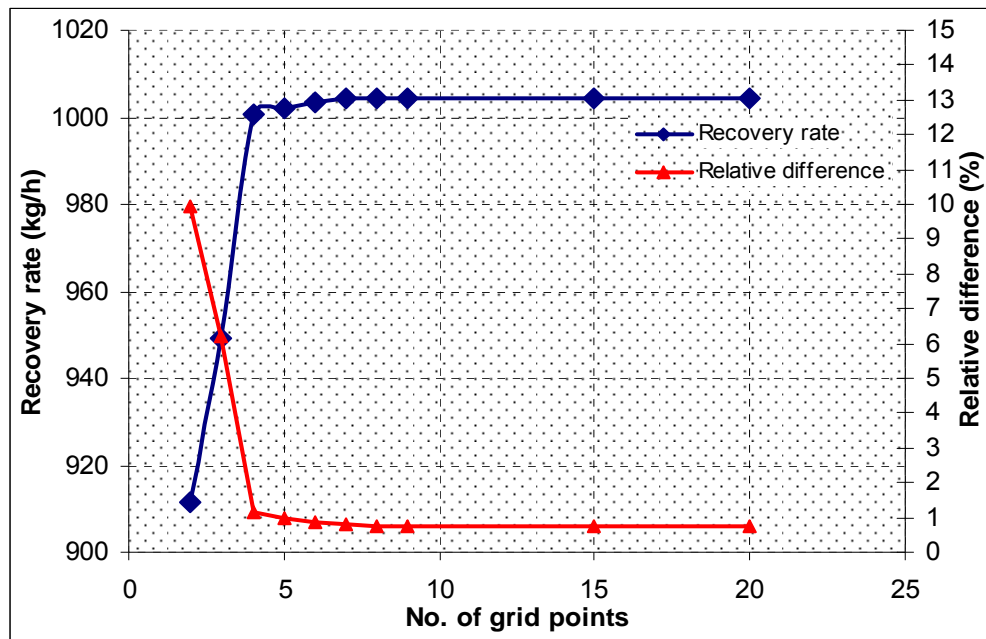


Figure 41: Variation of recovery rate versus different number of grid points as well as their relative differences to the benchmark data (Run 9)

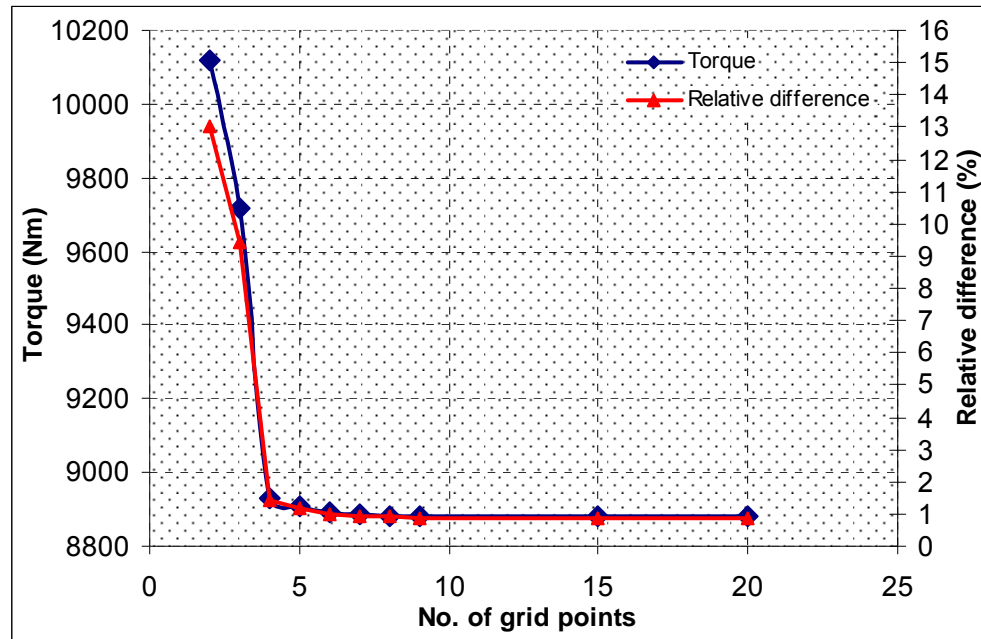


Figure 42: Variation of screw torque versus different number of grid points as well as their relative difference to the benchmark data (Run 9)

As seen so far, we studied the sensitivity analysis of the model developed in this work to the changes in the number of the grid points and the independent variables susceptible of influencing the experimental results (dependent or output variables) classified in several levels of intensity. Considering the time consuming and cost intensive characteristics of experimental works involved in fine tuning of the injection molding operations, it is desired to determine the influence of various input variables [Montgomery 91] on the final simulation results by other means than trial and error. The software developed from the mathematical model in this work has shown to be reliable in simulating the injection molding process and also being sensitive to changes in the number of the grid points.

Chapter 5

DISCUSSION

5.1 Sensitivity Analysis: Changes in thermo-physical properties

In this section the sensitivity of simulation results with respect to changes in polymer thermo-physical properties (i.e. thermal conductivity and specific heat capacity) for Runs 1, 5, and 9 is studied. In the injection molding process the parameters that could directly be influenced by changes in the thermo-physical properties are mainly melt temperature and screw torque. Due to poor thermal conductivity of polymeric materials, the impact of an underestimated or invalid thermal conductivity could potentially have more impact on the final melt temperature and screw torque compared to other thermo-physical properties (e.g. melt density).

5.1.1 Variations of Thermal Conductivity

Figures 43 and 44 depict the changes in the melt temperature and screw torque with respect to changes in the thermal conductivity in Run 1. In this analysis, the resin's thermal conductivity has been increased by 3, 5, 7, 9, 15, and 20% from its baseline value. At each variation the final simulated melt temperature and screw torque are compared with the data acquired with baseline thermal conductivity. The resulted relative differences with the experimental data for each variation are also depicted on the graphs.

As can be seen in Figure 43 for the final melt temperature, as the thermal conductivity increases, the final melt temperature decreases. It is also shown that the melt temperature obtained with max 12% of change in the thermal conductivity, is still within 5% of the melt temperature, which utilized the baseline thermal conductivity. Above 12% of changes in the thermal conductivity results in melt temperatures with more than 5% variation from the benchmark melt temperature with the baseline thermal conductivity.

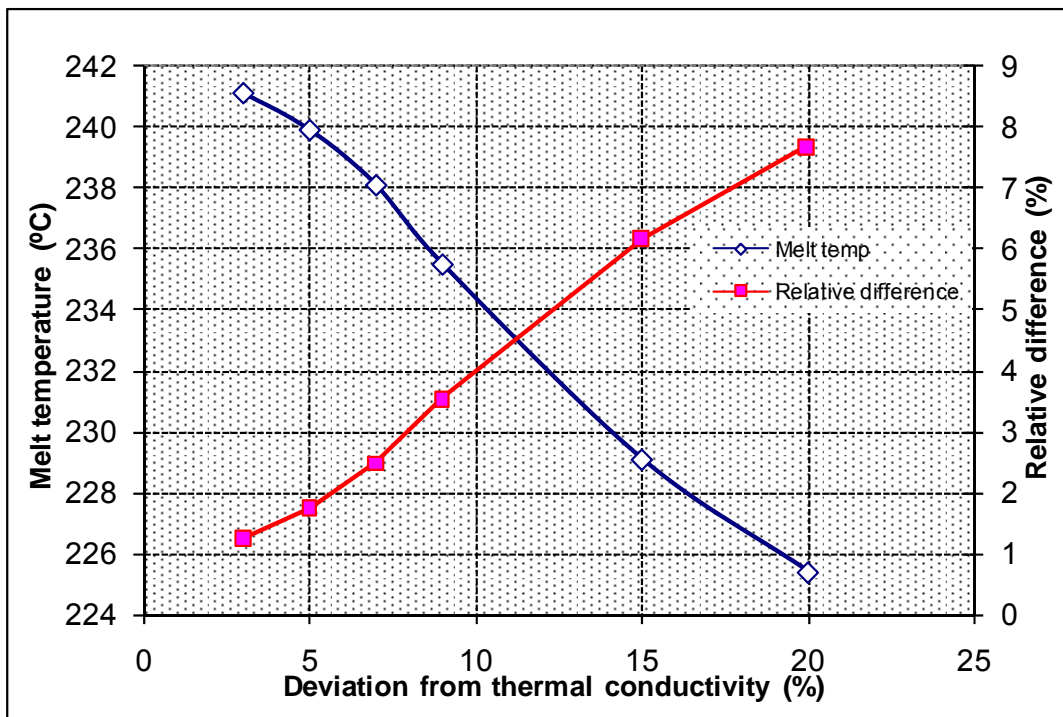


Figure 43: Variation of melt temperature versus variation of thermal conductivity as well as their relative differences to the benchmark data (Run 1)

In Figure 44 the impact of thermal conductivity variation on the final screw torque is depicted.

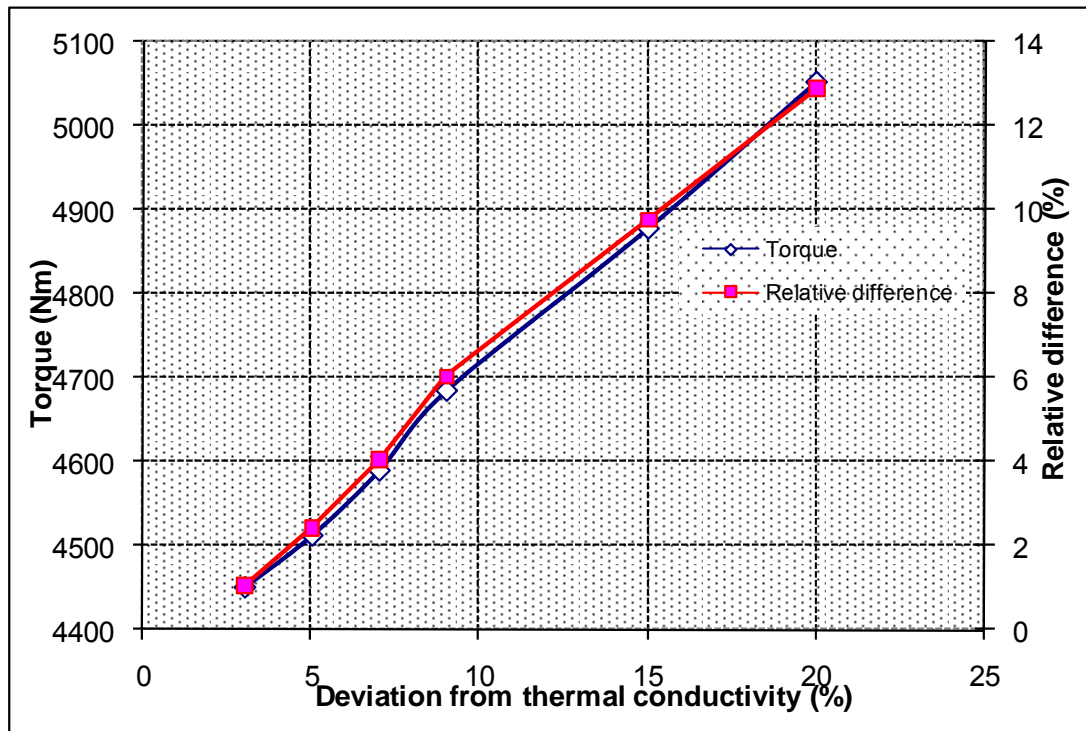


Figure 44: Variation of screw torque versus variation of thermal conductivity as well as their relative differences to the benchmark data (Run 1)

From Figure 44 it can be concluded that as the thermal conductivity of the polymer resin increases, the simulated required screw torque increases, which is in agreement with melt temperature results in Figure 43. Higher thermal conductivity will generate colder resin at the screw tip, which subsequently requires additional torque for keeping the screw at its set value. Figure 44 also shows that the screw torque obtained with maximum 9% increase in the thermal conductivity is still within 5% of the baseline screw torque. Above 9%, the relative differences of the screw torque with the test with benchmark thermal conductivity are more than 5%, which as mentioned in page 107, has been assumed undesirable in this work. From Figures 43 and 44 it can be concluded that for Run 1, up to 9% increase in the thermal conductivity will produce melt temperatures and screw torques, which are not more than 5% from the benchmark melt temperature and screw torque.

Figures 45 and 46 show the final melt temperature and screw torque variations with respect to changes in the thermal conductivity of the polymer and their relative differences for Run 5. Similar

to Run 1, the resin's thermal conductivity has changed for up to 20% from its original value and the simulated melt temperatures and screw torques are compared with their baseline values.

As can be seen in Figure 45, for Run 5 the final melt temperatures obtained with max 12% of increase in the thermal conductivity are still less than 5% of the benchmark melt temperature. Above 12%, the relative differences are more than 5% and the results are not desirable.

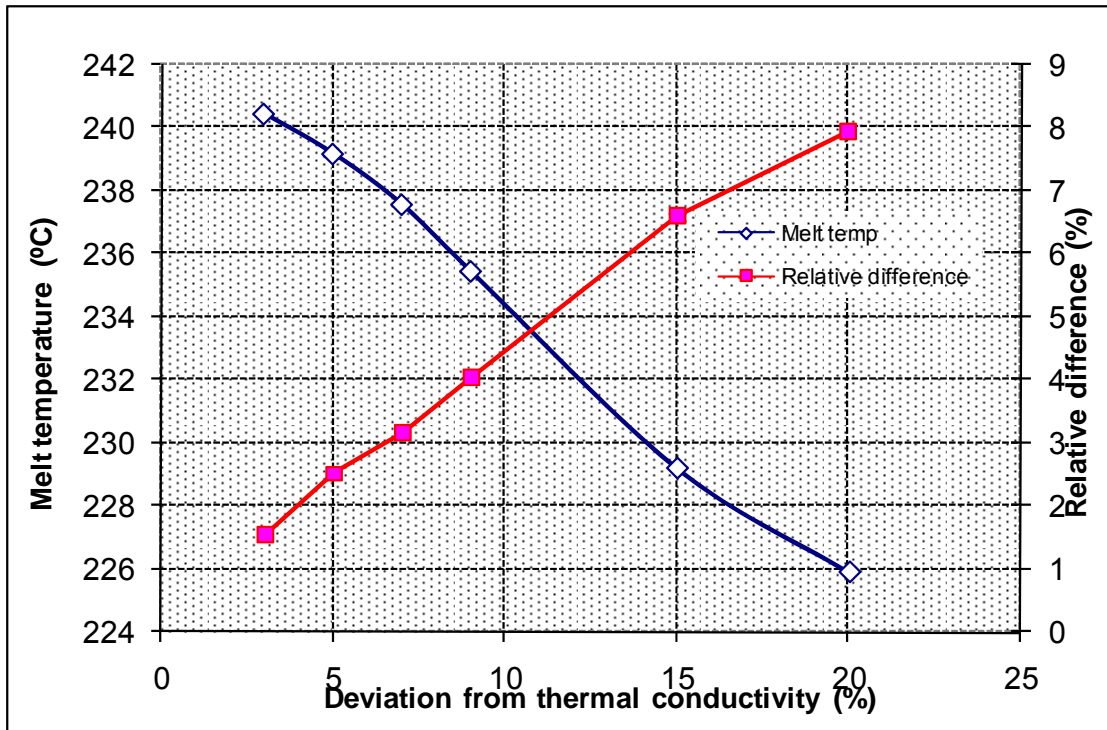


Figure 45: Variation of melt temperature versus variation of thermal conductivity as well as their relative differences to the benchmark data (Run 5)

In Figure 46, screw torque results obtained with maximum 9% increase in the thermal conductivity are still less than 5% from the benchmark value. Above 9%, the differences in the simulated screw torques have surpassed the 5% limit set in this study. One can draw a conclusion that in the case of screw torque in Run 5, more than 9% increase in the thermal conductivity is not desirable.

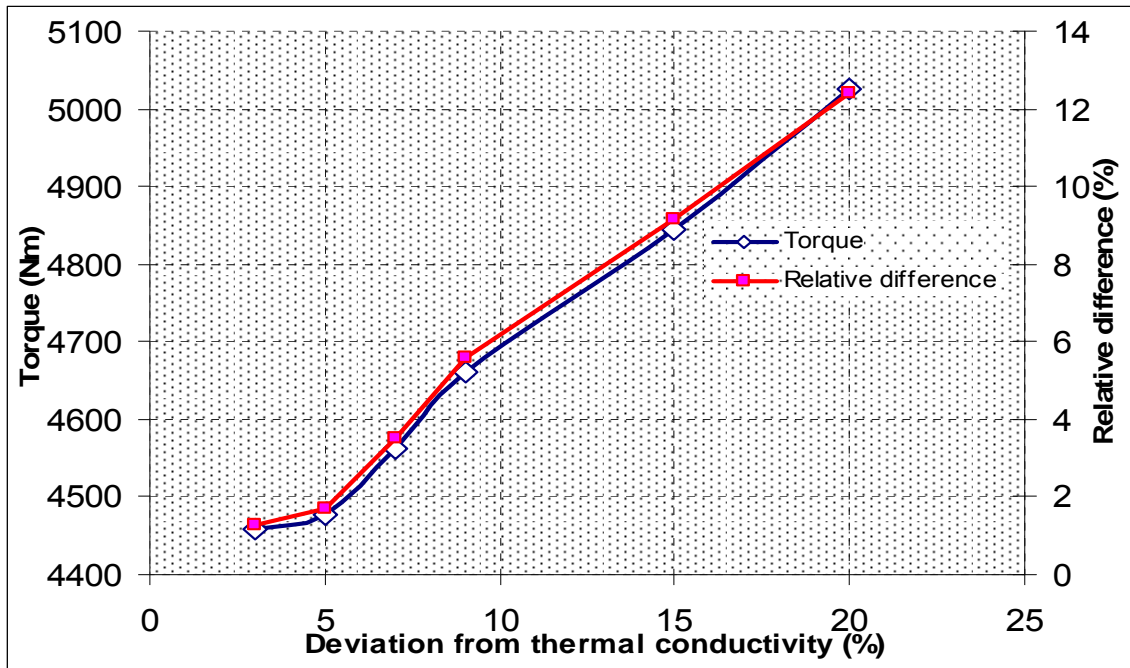


Figure 46: Variation of screw torque versus thermal conductivity changes and their relative differences to the benchmark data (Run 5)

Figures 47 and 48 show the final melt temperature and screw torque variations with respect to the changes in the thermal conductivity and their relative differences for Run 9. Like Runs 1 and 5, the resin's thermal conductivity is altered for up to 20% from its original value. Later, the final melt temperature and screw torque for each variation are simulated and compared with the baseline results. Since the thermal conductivity of PET is lower than the one of the high density polyethylene (0.24 and 0.50 W/m.K, respectively), the simulation results in PET case is expected to be less sensitive to deviation from the baseline compared to the same test with HDPE. This is explained more in Figures 47 and 48.

As can be seen in Figure 47 for the final melt temperature, results obtained with max 19% increase in the thermal conductivity are still within 5% of the baseline results. Above 19%, the relative differences of the simulated melt temperature results and baseline values are more than 5%. This shows a major difference compared to what was achieved with HDPE (more than 9% of increase in thermal conductivity produced undesirable simulation results).

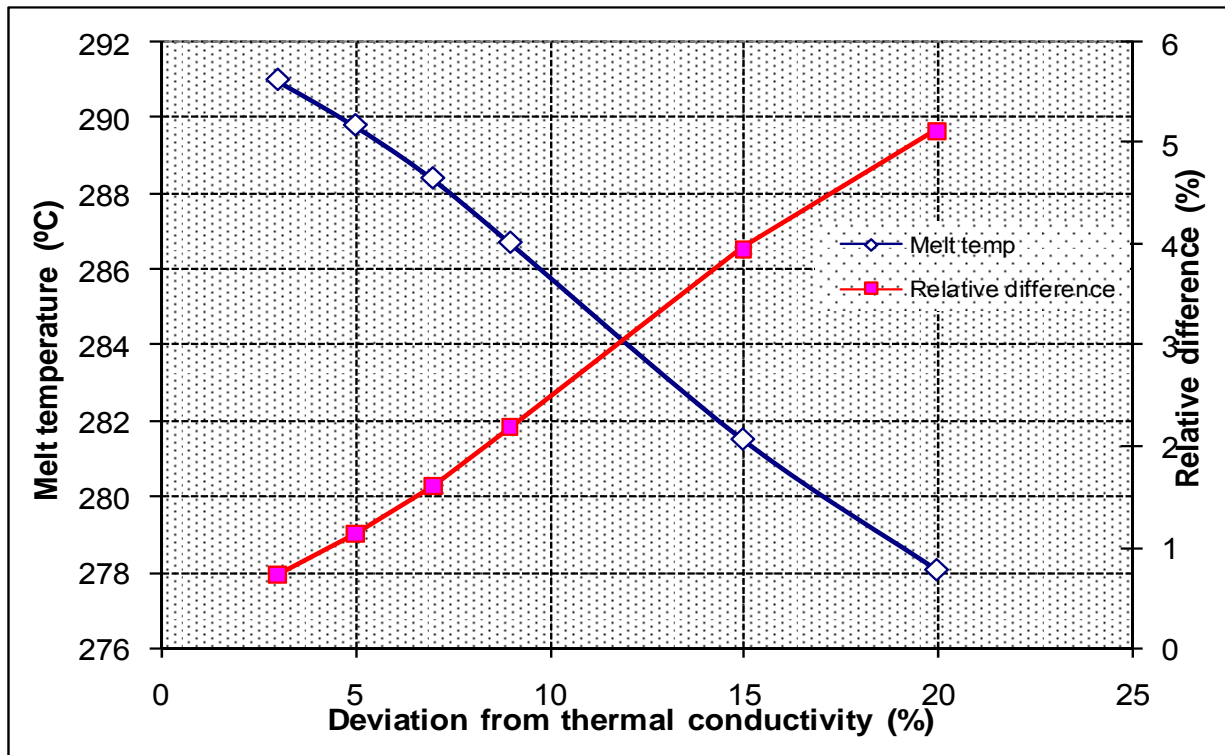


Figure 47: Variation of melt temperature versus variation of thermal conductivity as well as their relative differences to the benchmark data (Run 9)

In Figure 48, screw torque simulation results obtained with maximum 12% of increase in the thermal conductivity from the benchmark value are still within 5% from the baseline screw torque. The results produced so far show that the simulation tool is sensitive to changes in the thermal conductivity and generates different screw torques and melt temperatures as the thermal conductivity varies accordingly.

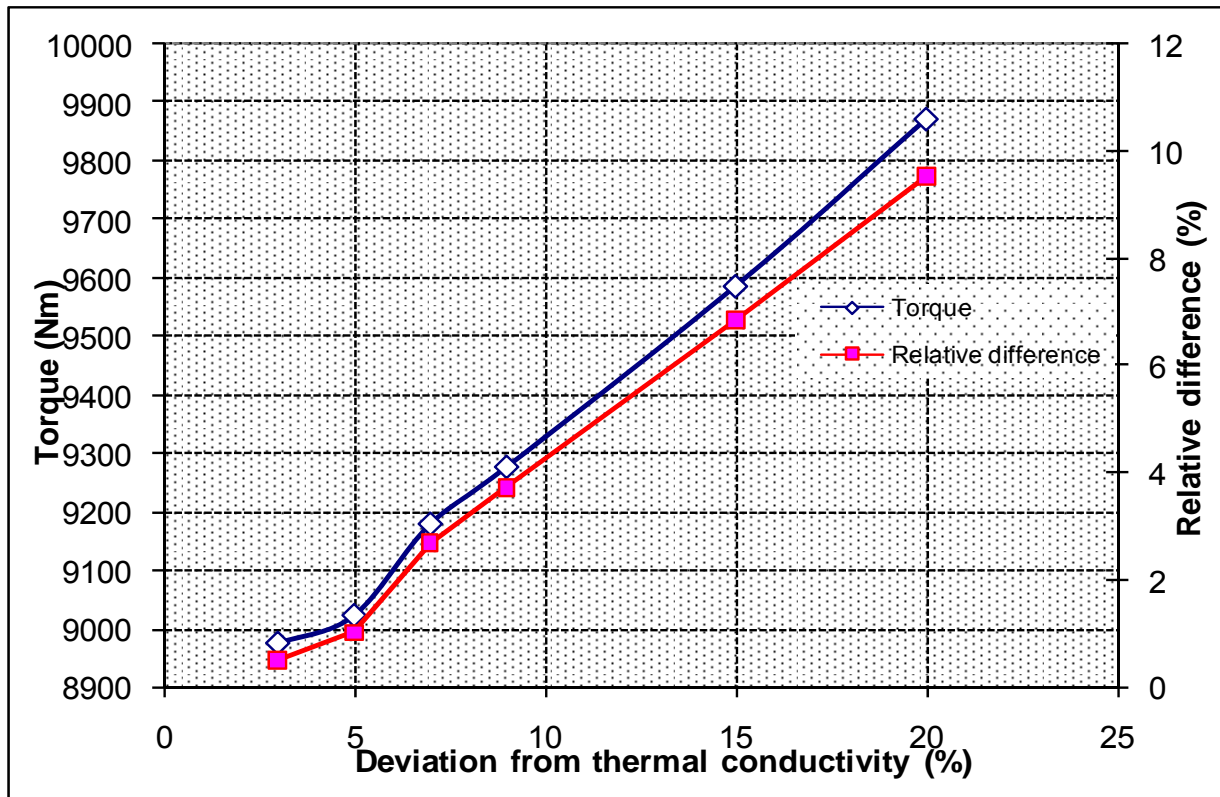


Figure 48: Variation of screw torque versus variation of thermal conductivity as well as their relative differences to the benchmark data (Run 9)

From Figures 47 and 48 it can be concluded that the maximum thermal conductivity increase for PET in Run 9 is 12% otherwise the simulation results will not be desirable. They also reveal that PET polymer is less sensitive to changes in the thermal conductivity compared to high density polyethylene. In Runs 1 and 5 the simulation results with more than 9% change in the thermal conductivity exceeded the 5% limit, set in this work. In Run 9, with up to 12% of increase in the thermal conductivity we still had screw torque and melt temperature that are within 5% of the baseline results.

5.1.2 Changes in the heat capacity

The heat capacity is the amount of heat required to raise the temperature of an object or substance by one degree. In this section, the sensitivity of the simulation package with respect to changes in the heat capacity of polymer resin in Runs 1, 5, and 9 is studied. In this section it will be shown

that the simulation responses and their relative differences to the baseline results are less sensitive to the changes in heat capacity compared to changes in the thermal conductivity.

Figures 49 and 50 depict the variation of final melt temperature and screw torque with respect to changes in the heat capacity and their relative differences for Run 1. At each variation, the final melt temperature and screw torque are simulated and the outcome are compared to the test results obtained with the baseline heat capacity.

As can be seen in Figure 49 for the final melt temperature, heat capacity changes of up to 19% from the baseline still produce simulation results within 5% of the baseline value. Above 19%, the difference between the simulated melt temperatures and the baseline melt temperature are more than 5% and are undesirable.

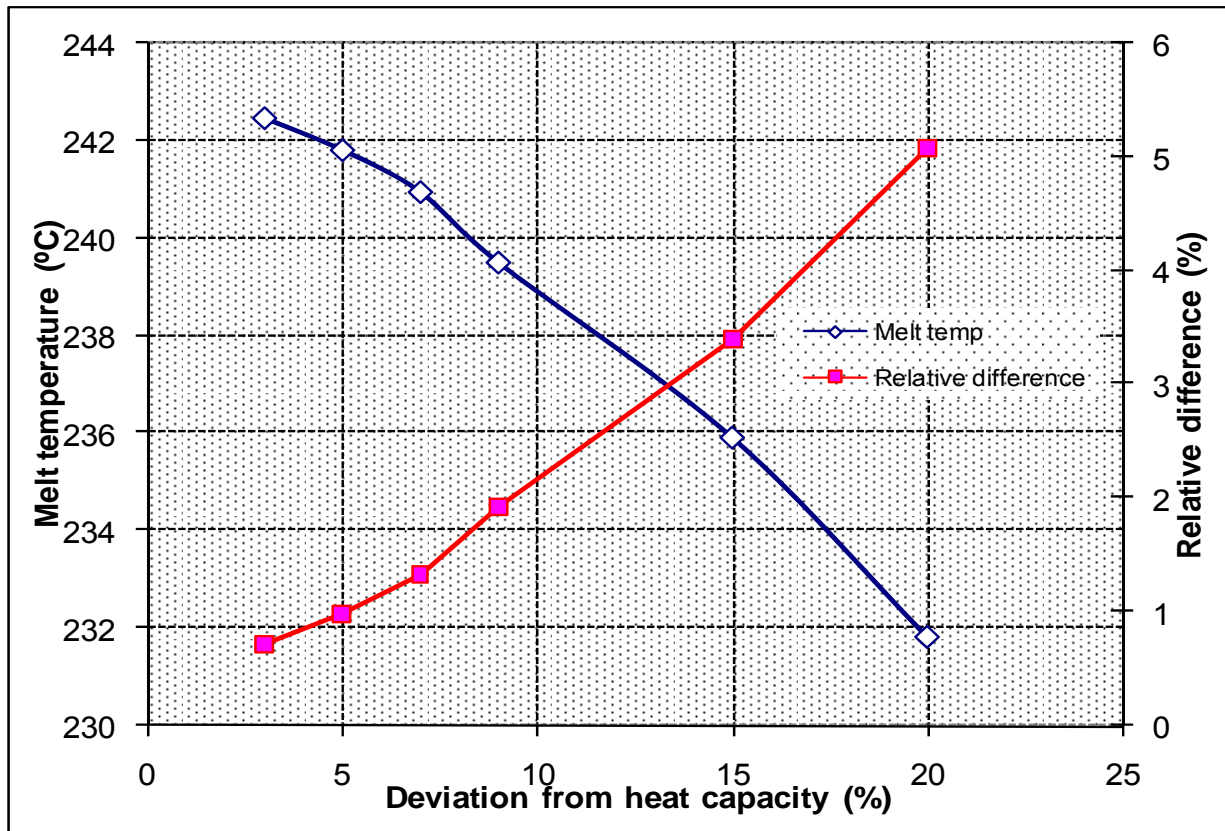


Figure 49: Variation of melt temperature versus variation of heat capacity as well as their relative differences to the benchmark data (Run 1)

In Figure 50, the simulated screw torques versus changes in the heat capacity is depicted. The results show that the simulated screw torque obtained with max 14% change in the heat capacity is still within the 5% of the baseline screw torque. It can be concluded from the above results that increasing of the heat capacity beyond 14%, will generate simulation outcome, which are undesirable.

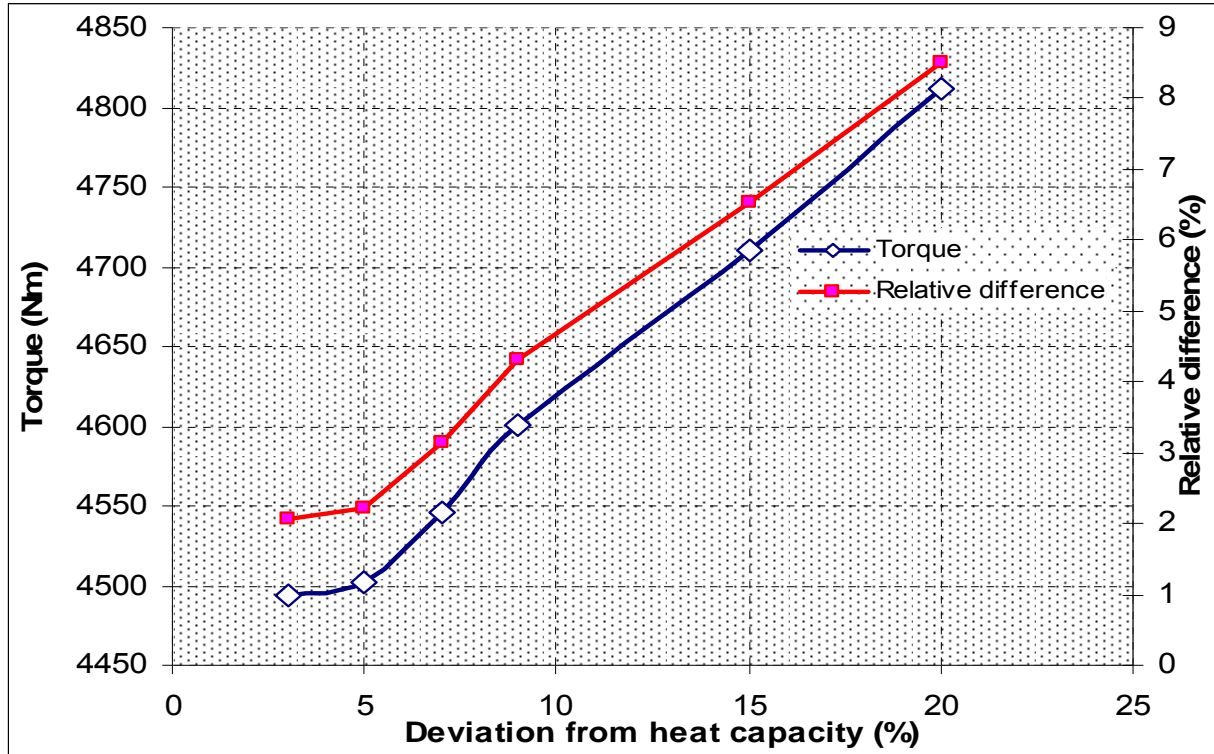


Figure 50: Variation of screw torque versus heat capacity variation and their relative differences to the benchmark data (Run 1)

Figures 51 and 52 show the final melt temperature and screw torque variations with respect to changes in the heat capacity in Run 5. Similar to Run 1, the resin's heat capacity increase from 3 to 20% from the baseline heat capacity and the final melt temperature and screw torque are compared with the baseline values. As can be seen in Figure 51 for the final melt temperature, results obtained with max 18% variation in the resin's heat capacity show compliance with the 5% acceptable limit in this work. Above 18%, the difference between the simulated melt temperatures and baseline melt temperature is more than 5%.

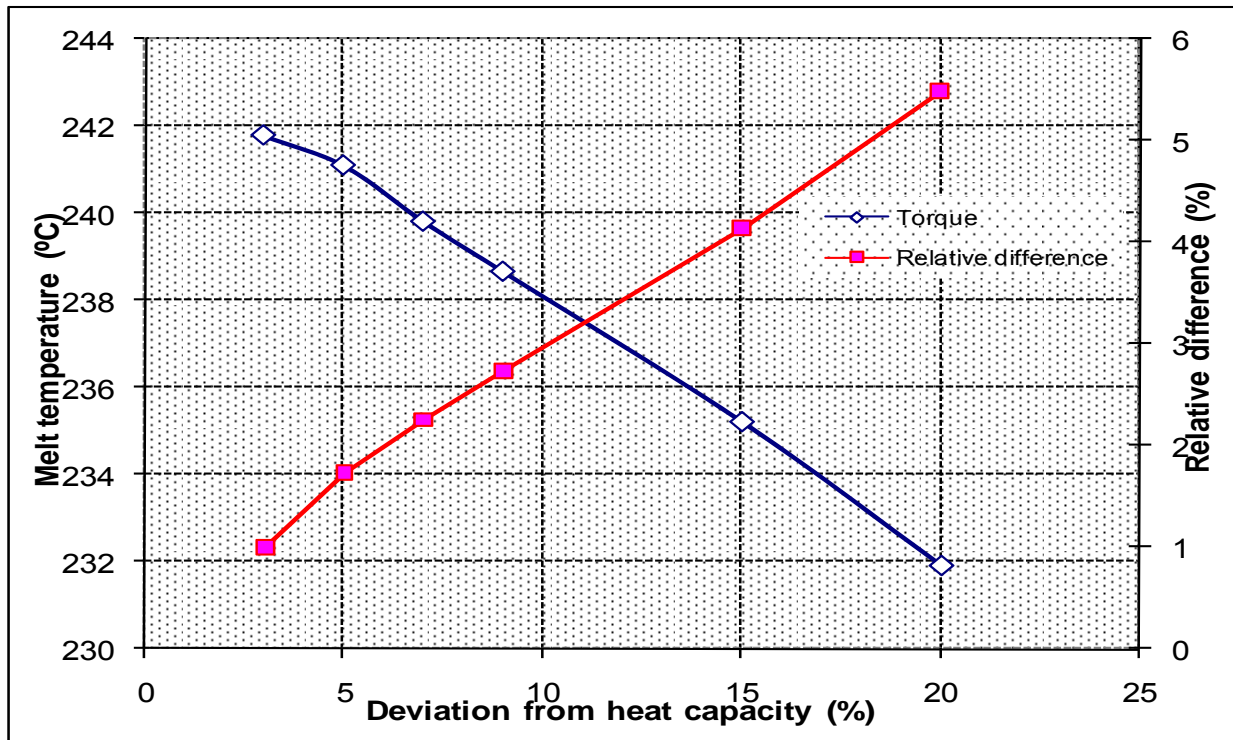


Figure 51: Variation of melt temperature versus variation of heat capacity as well as their relative differences to the benchmark data (Run 5)

In Figure 52, the changes in screw torque with respect to the changes in the heat capacity in Run 5 is shown. It can be seen that changes of up to 14% in the heat capacity will still produce screw torques that are within 5% of the baseline screw torque.

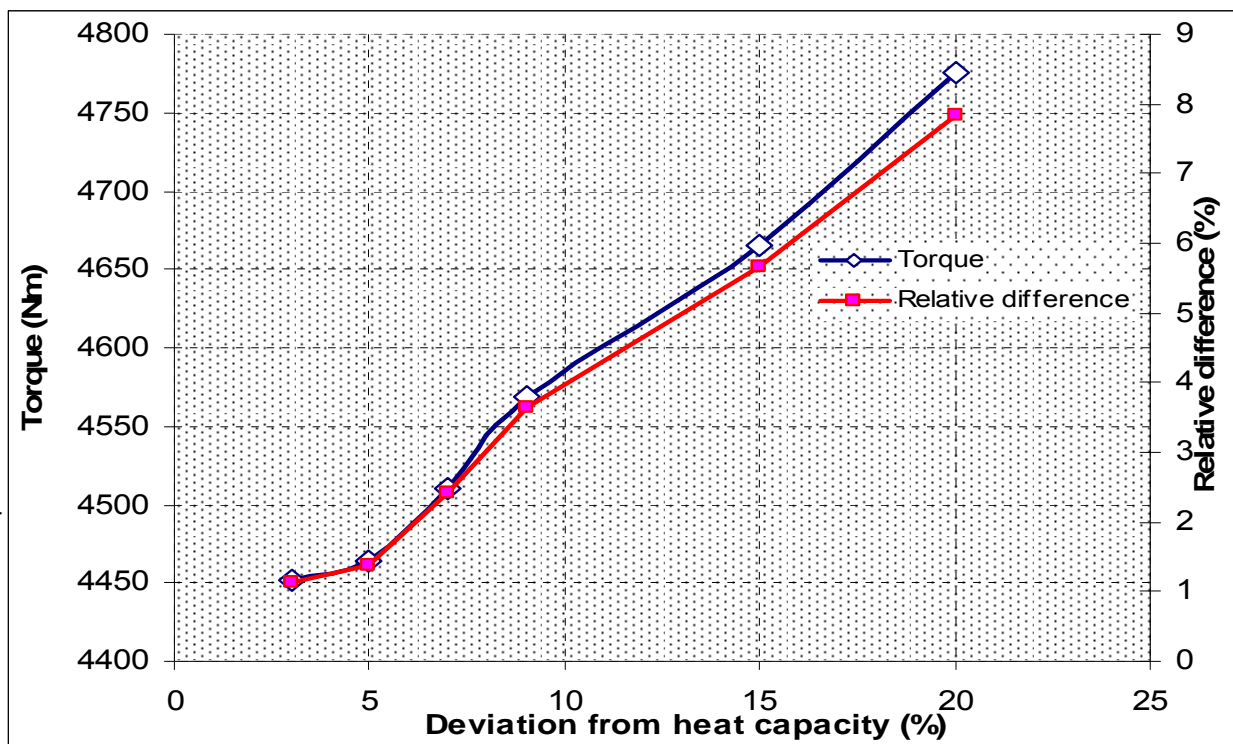


Figure 52: Variation of screw torque versus heat capacity variation as well as their relative differences to the benchmark data (Run 5)

Figures 53 and 54 depict the final melt temperature and screw torque variations with respect to changes in the heat capacity and their relative differences for Run 9.

As can be seen in Figure 53 for the final melt temperature, even 20% increase in the heat capacity from its baseline value will not deter the simulation results for more than 5% from the baseline result. In the case of 20% increase in the heat capacity in Run 9, the maximum difference with the benchmark will be still 3.04%. This is to confirm the low sensitivity of PET polymer to the variation in the heat capacity as well as thermal conductivity, which was mentioned earlier. The heat capacity of PET is considerably higher than the one for high density polyethylene (403 versus 58 J/mole.K, respectively at the melt state). As a result, PET will require much more energy to change its melt temperature by one degree. In HDPE with 58 J/mole.K heat capacity at melt state, smaller variation in the heat capacity will impact the final thermo-physical property responses more significantly (e.g. final melt temperature).

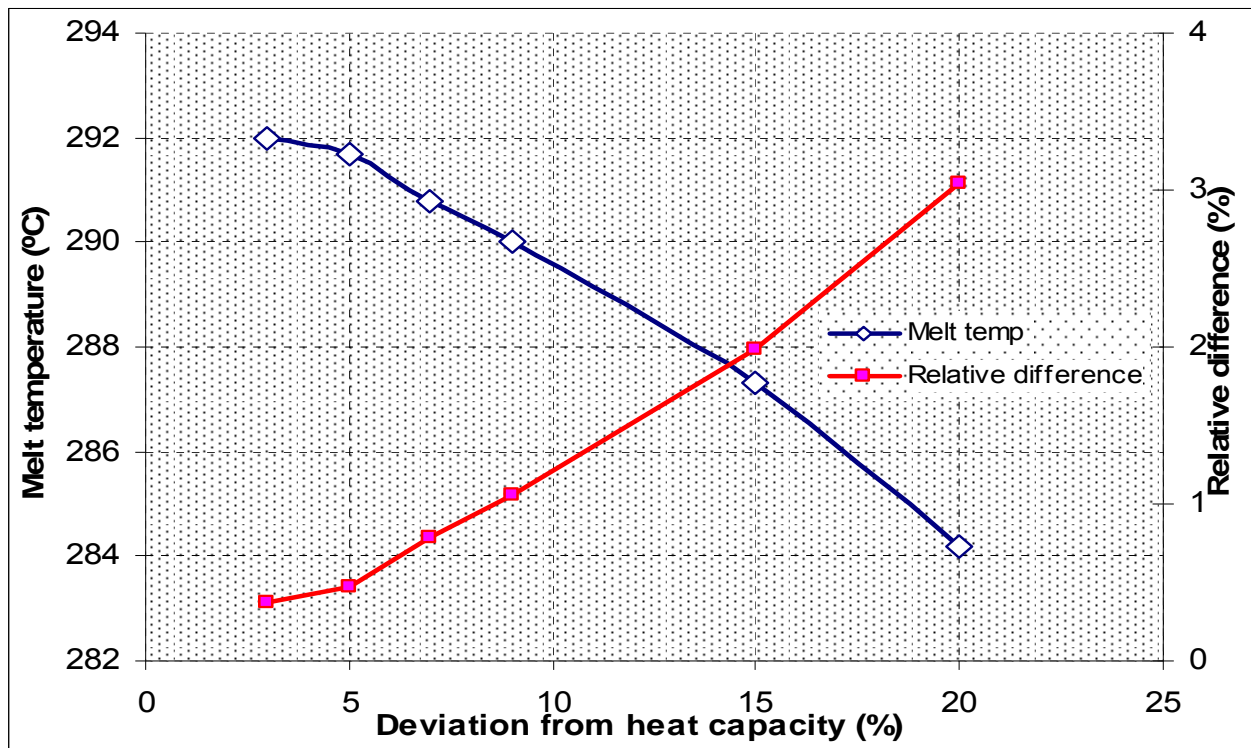


Figure 53: Variation of melt temperature versus heat capacity as well as their relative differences to the benchmark data (Run 9)

In Figure 54, the changes in the screw torque with respect to changes in the heat capacity of PET in Run 9 is depicted. The screw torque simulated with 19% increase in the heat capacity from the baseline value is still within 5% of the benchmark screw torque value.

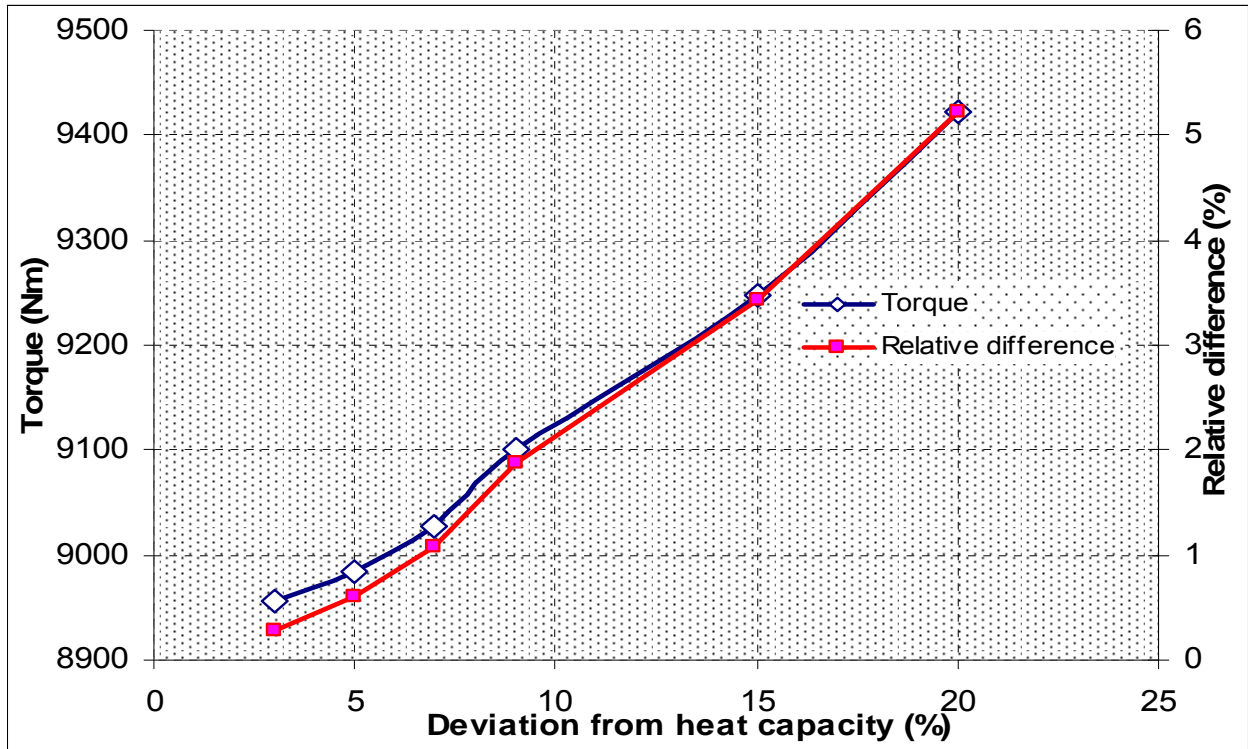


Figure 54: Variation of screw torque versus different heat capacity values as well as their relative differences to the benchmark data (Run 9)

Overall, it can be concluded that the simulation tool designed in this work is responsive in a positive way to changes in the thermo-physical properties of the PET and HDPE polymers, and produces results accordingly. The program has been used to identify the sensitivity of screw torque and melt temperature results with respect to invalid or excessive thermal properties of each resin.

5.2 A Case Study for Validation of Torque and Power

An experimental test conducted to further validate the simulation results for the screw torque and power. Table 16 depicts the machine settings and screw dimensions. During the run, all the processing conditions remained untouched and only the cycle time changed. This would provide the screw torque requirement under different throughput conditions. The reason for changing the

throughput is to find the relationship between the screw torque and cycle time, which is not believed to be linear.

Barrel ID	120	mm
Screw OD	111.86	mm
Inlet resin temperature to the barrel	163	°C
Initial pressure	0.1	Mpa
Barrel temperature setting	285	°C
Screw back pressure	300	psi

Table 16: Processing parameters for the screw torque and power experimental tests

Table 17 illustrates the test results. As can be seen, the barrel heat and screw speed remained unchanged and only the cycle time is varied along the experiment.

Run	Resin	Barrel heat (°C)	Screw speed (rpm)	Cycle time (s)	Torque (Nm)	Screw power (kW)	Throughput (kg/h)
1	PET IV: 0.83 PET Screw	285	93	8.64	12843.83	125.07	955.4
2				10.16	12143.56	118.26	810.2
3				11.84	11893.88	113.57	697
4				15.69	11546.92	110.01	526.7

Table 17: Design of Experiment for validation of screw torque and power results

As can be seen in Table 17, as the cycle time increases the screw torque and consequently the screw power usage reduces. The explanation is that the longer time with the same screw speed creates longer residence time of melt in the melt channel, causing the melt temperature to be warmer comparing to shorter cycle times. This is at the expense of lower throughput, which needs to be taken into account while designing the system characterizations. This longer residence time leads to lower viscosity and plasticizing torque demand. The point from the analysis of these cases

reveals that the relation between cycle time and plasticizing torque is not linear. This is explained more after comparing the simulation and experimental results. Table 18 illustrates the simulation versus experimental results for Runs 1 to 4.

Run	Cycle time (s)	Measured Power (kW)	Simulated Power (kW)	Measured Torque (Nm)	Simulated Torque (Nm)	Measured Throughput (kg/h)	Simulated Throughput (kg/h)
1	8.64	125.07	128.65	12843.83	13472.54	955.4	969.2
2	10.16	118.26	121.45	12143.56	12718.83	810.2	826.9
3	11.84	113.57	118.98	11893.88	12459.75	697.0	712.5
4	15.69	110.01	114.71	11546.92	12012.23	526.7	546.7

Table 18: Screw torque and power simulation versus experimental results

As can be seen, the simulation results are in agreement with the experimental data for different cycle times. Simulation results predict slightly higher torque, screw power consumption, and throughput than the experimental data. One of the reasons maybe the fact that the set screw speed is not always achieved by the system while the simulation tool considers 100% of the value in the calculations. The simulation tool also confirms the non-linear relationship between the cycle time, throughput, and screw torque demand. Figure 55 depicts the simulated screw torque demand for different cycle times.

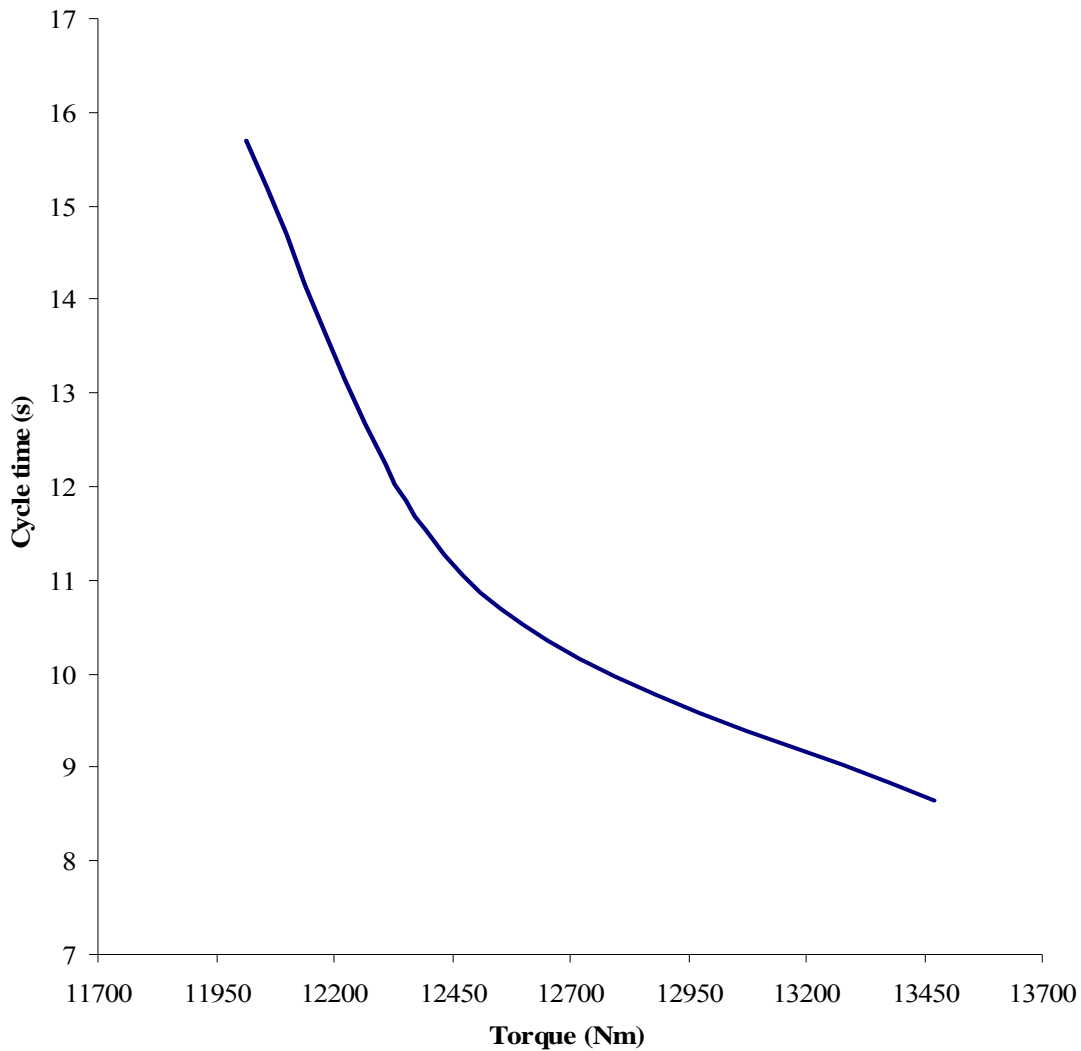


Figure 55: Cycle time versus screw torque for screw torque validation experiment

At cycle time of 8.64s, the simulated screw torque demand is 13472.54 Nm, which is the highest among other runs. At 10.16s and 11.84s cycle times the screw torque is simulated at 12718.83 and 12459.75 Nm, respectively. At 15.69s cycle time the screw torque is at its lowest value among Runs 1 to 4. At colder melt temperature, which is the case with 8.64s cycle time, the screw requires to consume more torque to turn at the preset screw speed of 93 rpm, while at hotter melt less effort is expected for the screw to retain its 93 rpm speed. This explains the non-linearity behavior between the cycle time and screw torque demand.

Figure 56 depicts the throughput behavior of the system versus required screw torque. This chart might be very desirable for injection molding industry for selection of required motor to turn the screw for a specific application since over prediction of the motor size is costly while under prediction of the motor will not provide enough melt and subsequently enough throughput, which is also costly for the manufacturers due to not meeting the production deadlines. This figure also confirms the non-linear relation between the throughput and screw torque requirements.

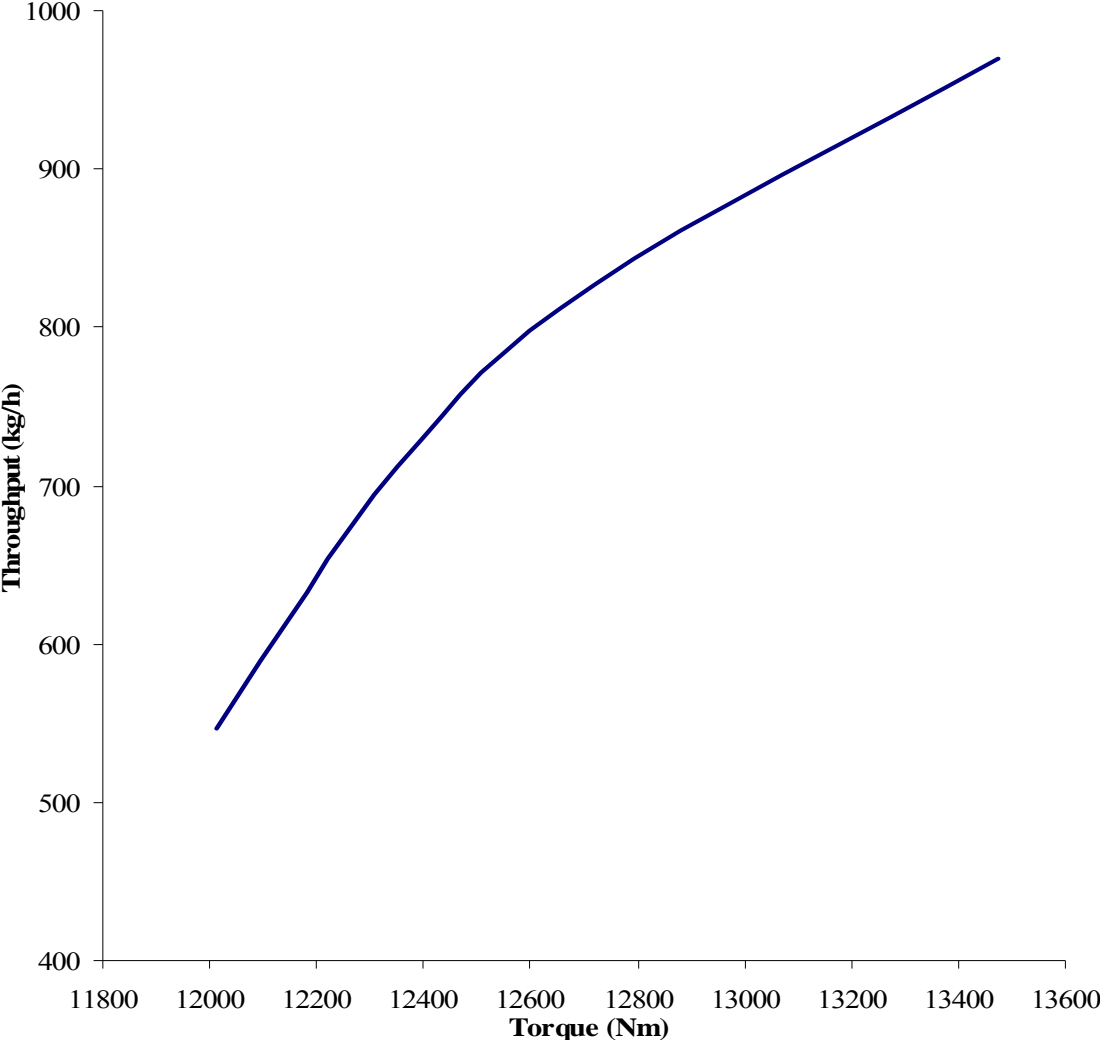


Figure 56: Throughput versus screw torque for screw torque validation experiment

As can be seen in Figure 56, below about 800 kg/h throughput, the rate in which the screw torque increases is slower compared to throughputs above 800 kg/h. As mentioned previously, at lower throughput the melt has more residence time and is at elevated temperatures so less torque is

required to turn the screw. At higher throughputs on the other hand, the melt is colder due to lower residence time and the viscosity increasing excessively as the temperature drops, leading to more torque demand to maintain the speed of the screw.

5.3 Simulation Results

Melt Temperature: The simulation results for HDPE shows that regardless of the screw design and barrel temperature setting, the melt temperature at the screw tip increases with increasing screw speed. The temperature of melt at the screw tip for Run 1, where the screw speed was at 190 rpm and barrel heat setting at 210°C is simulated at 241.2°C. Increasing the screw speed to 286 rpm (Run 2) with the same barrel heat causes the melt temperature to rise to 246.5°C. For Runs 3 and 4 with the barrel heat setting at 230°C, the simulation tool predicted that the melt temperature would be at 250.4°C with screw speed at 190 rpm, but it would rise to 256.4°C when the screw speed increased to 286 rpm. The final simulation results are within 2% of the experimental results.

The simulation results for HDPE with Barrier screw, (Runs 5-8), shows that similar to Runs 1 to 4, the melt temperature increases with rising screw speed and barrel initial heat. For Runs 5 and 6 with the barrel heat set at 210°C, as the screw speed increased from 190 to 286 rpm, the melt temperature at the screw tip increased from 243.6 to 248.4°C, respectively. In Runs 7 and 8, the barrel heat setting was fixed at 230°C. The simulation tool predicted a melt temperature of 253.2°C for Run 7 for screw speed at 190 rpm and 258.4°C for the same setting but increased screw speed (286 rpm). The simulation results for Runs 5-8 are also in agreement with the experimental data and are within 2% of measured melt temperature at the tip.

In Runs 9 and 10, the machine heat setting included two levels of 285 and 300°C, respectively. At 285°C barrel heat set, the melt temperature at the screw tip was simulated at 293.1°C. The temperature measured at this location by a thermocouple was 299.3°C, which compared to the experimental result shows a difference of within 2%. As mentioned in the theory, the majority of heat required for melting is supplied by the heat of dissipation due to friction between the barrel and polymer resin. In Run 10 the melt temperature measured at the screw tip is 306.4°C, which is

increased by about 2.1% from the set point. In Run 9 and with colder melt, due to additional shear heating, the melt temperature at the screw tip is about 4.7% more than the set point barrel heat.

Melt Pressure: Melt pressure can be studied from different aspects:

1. **At the screw tip**

The melt is under some pressure at all places in the extruder, as that is what pushes it forward, but when we refer to melt pressure in Table 8 in page 85, it is the melt pressure at the screw tip during recovery, which is particularly important, as it relates to safety (too much pressure can blow the nozzle head off), mixing (more pressure is good for mixing, especially in the metering zone), melt temperature (more pressure is equal to more work from motor and subsequently more frictional heat), and pumping rate (more pressure reduces pumping capacity).

2. **Inside the extruder barrel**

Figures 24 to 26 (pages 86-90) show the pressure profile across the extruder length for Runs 1-10. Usually a pressure peak in the profile may or may not be present. If the feeding zone carries in more than what the metering zone is capable of pumping out (poor screw design), there is a peak (typically at the entrance to the metering zone) and the pressure decreases from there to the screw tip. Otherwise, the pressure profile continually increases from feed to screw tip (which are the cases in Figures 24-26). The presence of a pressure peak is signaled by an overriding of temperature control in the zone that controls the metering entry, an output equal or even greater than drag flow of the last screw flight, and a blue discoloration of the screw (the blue-screw syndrome, which is usually observed during quality inspection of screws).

Runs 1 to 8 show that under similar processing conditions, the melt pressure during recovery with Barrier screw is higher than the general purpose (GP) screw. Within one screw design, the melt pressure during recovery is impacted by the screw speed and the barrel. When the screw speed in Run 2 increased to 286 from 190 rpm in Run 1 under constant barrel heat, the melt pressure at the screw tip during the recovery increased to 2263.4 psi from 1844.8, respectively. In Runs 6 when the screw speed increased to 286 from 190 rpm in Run 5, (constant barrel heat), the melt pressure during recovery increased to 2405.9 from 1961.0 psi, respectively. The same conclusion can be observed when the barrel heat is increased under constant screw speed. Additional barrel heat

reduces the final melt pressure during recovery. The simulation results in all the experiments are within 2% of the experimental data.

Screw Torque:

1. Effect of screw speed

The screw torque (i.e. the power needed to rotate the screw) was also a part of the mathematical model and an outcome of the simulation results. From the simulation results it can be concluded that the torque demand for the plasticizing screw increases as the screw speed increases in all screw designs in this work. In Runs 1 and 2 the simulated screw torque for plasticizing increased from 4488.4 to 4923.1 Nm as the screw speed increased from 190 to 286 rpm, respectively. The torque demand in Runs 3 and 4 increased from 4265.06 to 4661.78 Nm due to increase in screw speed from 190 to 286 rpm. In Runs 5 and 6 with the Barrier screw, the simulated screw torque for plasticizing increased from 4443.9 to 4880.93 Nm as the screw speed increased from 190 to 286 rpm and finally the torque demand in Runs 7 and 8 increased from 4236.10 to 4625.48 Nm due to increase in screw speed from 190 to 286 rpm, respectively.

2. Effect of barrel heat

The barrel heat set has the opposite effect on the screw torque compared to the screw speed. As the barrel heat increases, the torque demand for plastication decreases. In Runs 3 and 4 the simulated screw torque for plasticizing the resin are lower compared to Runs 1 and 2 due to higher barrel heat set (230°C versus 210°C, respectively). In Runs 7 and 8 the simulated screw torque are also lower compared to Runs 5 and 6 due to the same reason as Runs 3 and 4. In Runs 9 and 10 with the PET screw, higher barrel heat reduced the plasticizing torque demand by about 9% (8120.41 from original value of 8930.12 Nm, respectively).

Recovery Rate:

When the axial pressure gradient is increasing, the maximum axial melt velocity will be reduced. This effect will be more pronounced with large values of channel depth and helix angle and with a lower polymer viscosity. A positive pressure gradient in the metering zone of the screws in Runs 1-10 indicates that the metering zone has to develop pressure, resulting in reduced recovery rate. The actual velocity in axial direction (recovery speed), is directly related to the recovery rate down

the screw channel because this recovery rate equals the axial velocity of the melt multiplied the cross sectional areas of all the channels in the metering zone.

The simulation results for the recovery rate measurement shows that Barrier screws are slightly higher in recovery rate for a given processing condition than GP screws due to generation of more heat. Also it is shown that within one specific screw design, increasing the barrel heat set has an insignificant effect on the recovery rate, while increasing the screw speed increases the recovery rate more significantly. In Run 1 with barrel heat set at 210°C and screw speed at 190 rpm the recovery rate is simulated at 422.2 kg/h. When the screw speed increased to 286 rpm in Run 2 the recovery rate increased to 635.6 kg/h. Increasing the barrel heat set to 230°C in Runs 3 and 4 did not improve the recovery rate significantly. In Runs 3 and 4 with 230°C barrel heat set, the recovery rate increased to 422.7 and 636.3 kg/h as the screw speed increased from 190 to 286 rpm respectively. A similar trend can be observed in Runs 5-10, respectively.

Screw L/D:

The screw L/D requirement is directly influenced by the melt temperature. For the GP screw (in Runs 1 to 4), the lowest L/D belongs to the run with higher screw speed and barrel heat set (Run 4). Higher shear heating generation plus more conduction through barrel contributes to the lower L/D requirement. The highest L/D belongs to Run 1 where the barrel heat and the screw speed are at their lower level. This means that it takes more of the screw length for melting the resin. In Run 1 with 190 rpm screw speed and 210°C barrel heat, the L/D needed to melt the polymer is 24.54. As the screw speed increased to 286 rpm in Run 2, the L/D dropped to 20.94 due to higher shear heat generation. In Run 3 and 4 the barrel heat set increased to 230°C. In Run 3 the L/D requirements is 23.05, which compared to Run 1 with lower barrel heat shows lower L/D demand. As the screw speed increased to 286 rpm in Run 4, the L/D requirement dropped to 20.17, which is its lowest value among Runs 1-4.

For the Barrier screw in Runs 5 to 8 the same trend was observed. Barrier screw has a better melting capability and requires less L/D for melting compared to the GP screw. In Run 5 the L/D is simulated at 23.56, which is ~4% less than Run 1 with the same processing conditions but with the GP screw design. In Runs 6 to 8, the L/D demand for melting the polymer resin with the

Barrier screw dropped to 19.97, 22.95, and 19.04 from values of 20.94, 23.05, and 20.17 in Runs 2-4, respectively. For the PET screw, the L/D requirements for melting reduced from 22.44 to 21.29 as the barrel heat increased from 285 to 300°C, respectively.

Polymer Resin Viscosity:

Cross-WLF model is developed in the simulation tool to predict the gradient of viscosity along the extruder length as the temperature of the plastic resin rises. In Runs 1 and 2 the barrel heat set is at 210°C but the screw speed is higher in Run 2 than Run 1. In Runs 1 and 2 the simulated viscosity at the point of the screw tip is 431.7 and 338.6 Pa.s respectively.

In Runs 3 and 4 the barrel heat set is at 230°C with a difference in the screw speed (286 rpm in Run 4 versus 190 rpm in Run 3). As a result of higher barrel heat and subsequently higher melt temperature in Runs 3 and 4, the final viscosity is lower compared to Runs 1 and 2. In Runs 3 and 4 the viscosity at the screw tip is 427.2 and 333.9 Pa.s, respectively.

In Runs 5 and 6 the barrel heat is again set back at 210°C with the higher screw speed in Run 6 (286 versus 190 rpm in Run 5, respectively). The simulated melt viscosity at the screw tip in Runs 5 and 6 is 427.42 and 335.7 Pa.s, respectively.

In Runs 7 and 8 the barrel heat set is at 230°C but the screw speed is 190 rpm for Run 7 and 286 rpm for Run 8. As a result, the final viscosity is lower for Runs 7 and 8 compared to Runs 5 and 6 (424.3 and 331.3 Pa.s, respectively).

In Runs 5 to 8 with the Barrier screw, the final melt temperature is higher than Runs 1 to 4 so as the simulated melt viscosity at the screw tip.

In Run 9, the barrel heat set is at 285°C compared to 300°C in Run 10. All other processing conditions are the same. The simulated melt viscosity in Runs 9 and 10 is 529.7 and 502.6 Pa.s, respectively. Higher viscosity in Run 9 is due to its lower melt temperature (293.1°C compared to 304.4°C in Run 10). At the shear rate and temperature corresponding to the processing conditions used for the simulation, (26.1 s^{-1} and 290°C respectively), the actual melt viscosity is 507.2 Pa.s,

which shows a 5% deviation from the simulated value (529.7 Pa.s). In Run 10, the actual viscosity is 478.8 Pa.s, which is within 5% from the simulation results (502.6 Pa.s).

Screw Power:

The classic approach to calculating the screw power has been through a torque balance for the screw multiplied by screw rpm. In Run 1 with 210°C barrel heat and 190 rpm screw speed, the screw power consumption is 89.30 kW, which rises to 147.45 kW in Run 2 where the screw speed increased to 286 rpm. In Run 3 the screw speed is set back at 190 rpm but the barrel heat increased to 230°C. As a result the power consumption by the screw dropped to 84.86 kW, which is the lowest among Runs 1 to 4. In Run 4 the screw speed increased to 286 rpm with the barrel heat still at 230°C and subsequently the power consumption increased to 139.62 kW.

The same trend can be observed in Runs 5 to 8 with the Barrier screw. In Run 5, the barrel heat and screw speed are at 210°C and 190 rpm respectively and the screw power consumption is 88.42 kW. In Run 6 the screw consumes 146.18 kW power, which is the highest among Runs 5-8 since it has the highest screw speed and lowest barrel heat set. In Run 7 the screw power consumption is only 84.28 kW due to highest barrel heat and lowest screw speed. In Run 8 the screw speed rose to 286 rpm while the barrel heat set remained unchanged at 230°C. As a result the screw power consumption increased to 138.53 kW.

In Runs 9 and 10 the resin is changed to PET with a PET screw design. Due to high screw speed (300 rpm) and high screw torque during recovery, the power consumption is much higher than cases with polyolefin resin. In Run 9 the screw power consumption is 280.55 kW. In this test the barrel heat was at 285°C and the screw speed at 300 rpm. After increasing the barrel heat to 300°C the screw power consumption dropped to 255.11 kW due to decrease in amount of torque needed to turn the screw.

Overall Sensitivity Analysis:

For all three runs selected for the sensitivity analysis, simulation results obtained with less than 4 grid points have very poor accuracy compared to the experimental data (beyond 5% variation from the experimental results). Results obtained within 4 to 8 grid points are within 5% from the

experimental data plus the program converges within a reasonable computation time. Above 8 grid points, the simulation results do not show major improvement from the 5% limit set in this work while the computation time is significantly increased (more than 96 h for 9 grid points, 192 h for 15 grid points, and 2 weeks for 20 grid points comparing to average 18 h for 4 to 8 grid points).

For HDPE (Runs 1 and 5), it can be concluded that up to 9% change in the thermal conductivity compared to the baseline value produces simulation results that are still less than 5% from the experimental data. Above 9% of increase in the thermal conductivity results in simulated melt temperature and screw torque values that are beyond the 5% set limit. In the case of PET resin (Run 9), up to 12% increase in the thermal conductivity still results in melt temperatures and screw torques that are within 5% from the values obtained by benchmark thermal conductivity. The results also indicate that PET polymer is less sensitive to change in its thermal conductivity compared to HDPE.

Changes in the heat capacity appear to have less impact on the final simulated melt temperature and screw torque compared to the changes in the thermal conductivity for both PET and HDPE resins. For HDPE, up to 14% increase in the heat capacity from the baseline value still produces melt temperatures within 5% of the baseline values. In the case of PET resin (Run 9), heat capacity increase of up to 19% from the baseline has less than 5% impact on the simulation results compared to baseline data.

5.4 Viscosity Models

Power law and Cross-WLF models are well-known viscosity models to reliably predict the viscosity of various polymer fluids. Power law model predicts excellent estimate of the viscosity at higher shear rates, but overestimates the viscosity at lower shear rates (which is the case in the injection unit of an injection molding system). On the other word, Power law model will provide more accurate estimates than the Newtonian model, yet overestimates the pressure drop compared to the Cross-WLF model since it overestimates the viscosity at lower shear rates. As mentioned earlier, Cross-WLF model is employed in this study for estimation of final melt viscosity.

5.5 Dependency of Viscosity on Zero Shear Rate

In the shear stress versus shear rate graph, it is expected that the shear stress increases with increasing shear rate but that the ratio of these two quantities depends only on the polymer fluid under study. This ratio (shear stress over shear rate) is used to define the shear viscosity, which may depend on temperature, pressure, and shear rate.

In essence, the zero-shear viscosity is the viscosity that a product will ultimately attain when at rest and undisturbed. It can also be described as the viscosity at the limit of low shear rate. A Newtonian fluid has a constant viscosity independent of shear rate so the shear stress is a linear function of shear rate and the stress is zero at zero-shear rate. In polymeric materials (shear thinning), the viscosity decreases with increasing shear rate and the curve of shear stress versus shear rate bends toward the shear rate axis. So at low shear rates, the viscosity of the polymer fluid will change very slowly. In this case, there is almost a plateau viscosity (minor changes due to low shear) as the shear rate increases in shear thinning polymers. Figure 57 depicts the zero-shear viscosity effect while the shear rate is still low. At low shear rates, the heat generated by friction is low and will not cause significant drop in the viscosity of the polymer.

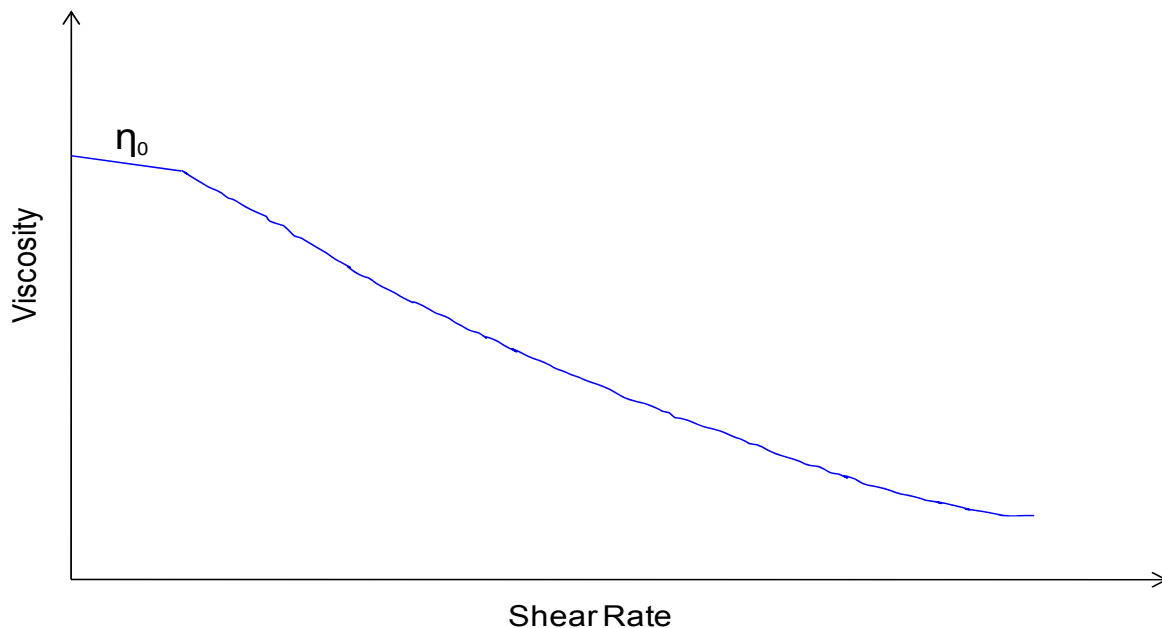


Figure 57: Zero-shear rate viscosity: The viscosity change in the shear thinning polymers is minimal at lower shear rate values.

As shown in the figure, for sufficiently low shear rate values, viscosity becomes independent of shear rate, i.e., the material exhibits Newtonian behavior. So η_0 is the low shear rate limiting value of viscosity and the WLF model considers this change over Power-Law model.

5.6 Total Shear Rate

The total shear rate is being used for the calculation of the following terms:

1. Final viscosity in the Cross WLF viscosity model
2. Maximum screw torque
3. Heat of dissipation

A successful screw design is one in which the amount of shear heat generated is sufficient to ensure that the entire polymer is converted to a suitable molten state before the end of the screw. At the same time excessive shear heat will lead to undesirable conditions including degradation and more than desired melt temperatures. That is why it is important to accurately calculate the total amount of shear heat, which is generated during the melting process. The magnitude of the total shear rate is obtained by vectorial addition of shear rates at different axes. The total shear rate is an important variable in the description of the mixing process and melt quality.

A polymeric flow that melts early will be exposed to a significant mixing history by the time it reaches the end of the melting zone. Polymer fluid in the center of the flow channel is exposed to a very low shear rate and their residence time is shorter because the velocities are the highest in the center.

Chapter 6

CONCLUSIONS

A set of three-dimensional mathematical model in helical coordinates as a set of partial differential equations for describing the flow behavior of incompressible polymer melts inside the injection unit of an injection molding machine was developed. Based on the literature survey we see that the application of natural flow geometry of the injection process along with varying plastic thermo-physical properties to model the polymer melt flow has not been introduced before by which we intent to furnish this gap in this study.

The comparison between experimental and computational results clarifies the importance of the mathematical model. It is shown in this study that the numerical model developed in this initiative results in close approximation with the experimental ones, regardless of the processing conditions and/or material used. An experimental test was designed to validate the simulation results. Two

different resins (HDPE and PET) with different processing conditions and properties plus three different screw designs were selected to conduct experimental tests. The average melt temperature and melt pressure at the screw tip during recovery, the screw L/D required for proper resin bulk temperature, screw torque, viscosity, and screw power consumption during recovery were simulated and compared with the experimental data. The observation showed that the simulation results were in close range with the experimental data.

In this initiative, we studied how the variation in the input of certain parameters in the developed mathematical model can qualitatively or quantitatively influence the variation in the responses of the model.

The sensitivity of the simulation results with respect to different grid sizes and process parameters for selected Runs (1, 5, and 9) was analyzed and their impact on certain responses including final recovery rate, melt temperature, and screw torque investigated. The results showed that sensitivity of the mathematical model for some input parameters is directly influenced by the type of the polymer resin while for others varies regardless of the resin type.

Chapter 7

FUTURE WORK

Several challenging and interesting studies can be carried out for the purpose of extending the present work including:

1. Development of an optimization methodology for the mathematical model of the single screw extruder developed in this initiative:

Since the solution to a mathematical model is not usually unique, a strategy can be developed, where the equations available to solve the direct problem are used iteratively, until the solution converges to an optimum. Genetic Algorithms (GAs) can be chosen as the optimization algorithm [Upreti 03], given their capacity for dealing with combinatorial-type problems and the fact that they do not require neither derivative information nor other additional knowledge. The performance of such optimization scheme depends, mainly, on

the validity of the predictions and also, on the sensitivity of the modeling package to changes in the input variables. Therefore, a numerical modeling package able to take these aspects into consideration and, simultaneously, produce results with lower computation time, is also implemented and validated

2. Further development of the optimization methodology in previously mentioned future work for screw design including modeling of Barrier screws
3. To Apply the methodology developed in this work to the study on the modeling, simulation and optimal control of the operating conditions and screw design of a co-rotating or counter-rotating twin-screw extruder
4. Further development of the mathematical model to include the evaluation of colorants, comonomers, additives, and coating agents applications in the process of injection molding

NOMENCLATURE

Symbols	Definition, Units
a	initial value of r (radius variable for helical coordinates)
b	tapered parameter of the screw along its length, m
$C_p(T)$	temperature dependent heat capacity, J/kg.K
D	screw diameter, m
e	non-orthogonal velocity
H	flight depth, m
k_4	pitch of the screw, dimensionless
$K(T)$	temperature dependent thermal conductivity, W/m.K
L	screw length in [Wang 04], m
M	$\sqrt{k_4^2 + r^2}$
N	screw speed, m/s
$P_{i,j,k}$	pressure build up across the screw dimensions, Pa
Q	flow rate, kg/h
q_{Diss}	heat of dissipation, Pa/s
r, θ, z	variables for the helical coordinates
$\bar{r}, \bar{\theta}, \bar{z}$	variables for the cylindrical coordinates in [Laurence 75] and [Wang 04]
R, θ, Z	variables for the helical coordinates in [Laurence 75] and [Nebrensky 73]
R_b	barrel radius, m
R_s	screw radius, m
R	inner radius of the barrel ($R_s + \delta$), m
s	dimensionless helical coordinate
T	temperature, °C

T_b	set temperature of the barrel, °C
u_1, u_2, u_3	velocity profiles in cylindrical coordinates, m/s
u_r, u_θ, u_z	velocity profiles in helical coordinates, m/s
V_θ	melt velocity in theta direction, m/s
V_z	melt velocity in screw axial direction, m/s
W	flight width, m
x_1, x_2, x_3	cylindrical coordinates
x, y, z	coordinate variables for the rectangular coordinates ([Wang 04], [Yu 97a and b])

Greek Symbols Definition, Units

α	velocity gradient in theta direction with respect to z direction
β	temperature gradient with respect to z direction
δ	screw flight, m
η	viscosity, Pa.s
$\dot{\gamma}_{i,j,k}$	shear rate, 1/s
$\tau_{i,j,k}$	shear stress, Pa
$\rho(T)$	temperature dependent density, kg/m ³
ϕ	combined momentum flux tensor
$\varphi(l)$	function which identifies helicity, $\varphi(l) = \frac{2\pi}{L}l$
ω	melt velocity, rpm
ψ	solid conveying angle, radian

REFERENCES

- [Agassant 96] Agassant, J.F, Avenas, P, Sergent, J, La Mise en Forme des Matières Plastiques, Lavoisier, 3rd édition, Paris (1996)
- [Aris 90] Rutherford Aris, Vectors, Tensors, and the Basic Equations of Fluid Mechanics, pp. 134-160, Dover Publications, (1990)
- [Barton 02] Barton P.; Modeling, Simulation and Sensitivity Analysis of Hybrid Systems, PORTAL: ACM Digital Library, 12, pp.256-289, (2002)
- [Bigg 73] Bigg, D. M., Mixing in a Single Screw Extruder, Ph.D. Thesis, University of Massachusetts (1973)
- [Bigg 74] Bigg, D.M., Middleman, S., Mixing in a Screw Extruder, A Model for Residence Time Distribution and Strain, Ind. Eng. Chem. Fundam., 13, pp.66-71 (1974)
- [Booy 04] Booy, M. L., Influence of Channel Curvature on Flow, Pressure Distribution and Power Requirements of Screw Pumps and Melt Extruders, 3, pp.176-185, (2004)
- [Breierova 01] Breierova, L., M. Choudhari, M., An Introduction to the Concepts and Methods of Sensitivity Analysis of System Dynamics Models, MIT System Dynamics in Education Project, 2001
- [Broszeit 97] Broszeit, J., Finite Element Simulation of Circulating Steady Flow for Fluids of the Memory-Integral Type: Flow in a Single-Screw Extruder, J. Non-Newt. Fluid Mech., 70, pp.35-58 (1997)
- [Carley 53] Carley, J. F., Mallouk, R. S., McKelvey, J. M., Simplified Flow Theory for Screw Extruders, The Symposium on the Theory of Plastic Extrusion, Ind. Eng. Chem., 45(5), pp.974-982 (1953)
- [Chang 95] Chang, R.Y., Lin, K. J., The Hybrid FEM/FD Computer Model for Analysis of the Metering Section of a Single Screw Extruder, Polym. Eng. Sci., 35, pp. 1748-1757 (1995)
- [Chapra 05] Chapra, S.C., Canale, R. P., Numerical Methods for Engineers, 5th Edition, McGraw-Hill Science/Engineering/Math Chapter 23 (2005)
- [Chiruvella 95] Chiruvella, R. V., Jaluria, Y., Abib, A. H., Numerical Simulation of Fluid Flow and Heat Transfer in a Single Screw Extruder with Different Dies, Poly. Eng. Sci., 11, pp. 93-98 (1971)

- [Choi 87] Choi, Y., Okos, M. R., Effect of Temperature and Composition on the Thermal Properties of Foods, Food Engineering and Process Applications: Transportation Phenomena 1, pp. 93-101, (1987)
- [Choo 80] Choo, K. P., Neelakantan, N. R., Pittman, J. F. T., Experimental Deep-Channel Velocity Profiles and Operating Characteristics for a Single Screw Extruder, Polymer Engineering and Science, 20 (5), pp.349-356 (1980)
- [Choo 81] Choo, K. P., Hami, M. L., Pittman, J. F. T., Deep Channel Operating Characteristics of a Single Screw Extruder: Finite Element Predictions and Experimental Results for Iso-Thermal Non-Newtonian Flow, Polymer Engineering and Science, No. 21(2), pp.100-104 (1981)
- [Chung 71] Chung, C. I., Plasticating Single Screw Extrusion Theory, Polym., Eng. Sci., 15, pp.261-273 (1971)
- [Chung 75] Chung, C. I., Maximum Pressure Developed by Solid Conveying Force in Screw Extruders, Polym. Eng. Sci., 35, pp.29-34 (1975)
- [Chung 00] Chung, C. I., Extrusion of Polymers: Theory and Practice, pp. 89-92, 142-145, 169-172, Hanser Publishers, Munich (2000)
- [Colwell 59] Colwell R. E., Nicholas K. R., The Screw Extruder, Ind. Eng. Chem., 51: pp.841-843, (1959)
- [Covas 99] Covas, J.A., A.G. Cunha, P. Oliveira, An Optimization Approach to Practical Problems in Plasticating Single Screw Extrusion, Poly. Eng. Sci., 39, pp. 443-456 (1999)
- [Creamer 76] Creamer, L. K., Casein Proteolysis in Mozzarella-type Cheese, New Zealand Journal of Dairy Science and Technology, 11, 130-135 (1976)
- [Cunha 94] Cunha, A.G., Simulation of Extrusion Process, Master Thesis, University do Minho, Braga (1994)
- [Cunha 94] Cunha, A.G., Oliveira, P., Covas, J. A., Genetic Algorithms in Multi-objective Optimization Problems – An Application to Polymer Extrusion", GECCO-99, Workshop on Multi-criterion optimization using evolutionary methods, Orlando, USA, (1999)
- [Dan-Nieh 85] Dan-Nieh, F., Zhong, X., Tensorial Fluid Mechanics, The Water Resources & Electric Power Press, Beijing (1985)
- [Darnell 56] Darnell, W. H., Mol, E.A.J., Solids Conveying in Extruders, SPE J., 12, pp.20-29 (1956)

- [Elbirli 84] Elbirli, B., Lindth, J. T., Gottgetreu, S. R., Baba, S. M., Mathematical Modeling of Melting of Polymers in a Single Screw Extruder, Polym., Eng., Sci., 24, pp. 988-999 (1984)
- [Fenner 77] Fenner, R. T., Development in the Analysis of Steady Screw Extrusion of Polymers, Polymer, 18, pp.617-635 (1977)
- [Fenner 80] Fenner, R. T., Principles of Polymer Processing, New York, NY: Chemical Publishing Ltd., pp.231-233 (1980)
- [Fleming 04] Fleming, D., J., Presentation on Rheological Testing for Measuring Melt Viscosity, Polymer Testing, Brussels Marriott Hotel, Belgium (2004)
- [Fischer 97] Fischer, P., Wortberg, J., VDI-Verlag Düsseldorf, VDI conference on The Single Screw Extruder – Basics and System Optimization., (1997)
- [Fogel 66] Fogel, L.J., Owens, A.J., Walsh, M.J., Artificial Intelligence Through Simulated Evolution, Wiley Publishing, New York (1966)
- [Fridge 72] Fridge, W., Tensor Analysis & Continuum Mechanics, Springer Verlag, Berlin, New York (1972)
- [Gaspar 99] Gaspar-Cunha, P. Oliveira, and J.A. Covas, Genetic Algorithms in Multi-objective Optimization Problems – An Application to Polymer Extrusion, GECCO-99, Workshop on Multi-criterion optimization using evolutionary methods, Orlando, USA, (1999)
- [Griffith 62] Griffith R. M., Fully Developed Flow in Screw Extruders, Ind. Eng. Chem. Fundamentals, 3, pp181-187, (1962)
- [Hami 80] Hami, M. L., Pittman, J. F. T., Finite Element Solutions for Flow in a Single Screw Extruder, Polymer Eng. & Sci., 20, pp.339-345 (1980)
- [Holland 75] Holland, J.H., Adaptation in Natural and Artificial Systems, University of Michigan Press (1975)
- [Hyun 97] Hyun, K. S., Spalding, A New Model for Solid Conveying in Single Screw Plasticating Extruders, SPE-ANTEC Tech. Papers, (Electronic Version) (1997)
- [Kamal 89] M. R. Kamal, V. Tan, and F. Kashani. Adv. Polymer Technology, 3, 89 (1989)
- [Laurence 75] Laurence, R. L., Tung, T. T., A Coordinate Frame for Helical Flows, Poly. Eng. & Science, Vol. 15(6): pp.401-405 (1975)
- [Li 94] Li, Y., Hsieh, F., New Melt Conveying Models for a Single Screw

- Extruder, *Journal of Food Process Engineering*, 17, pp.299-324 (1994)
- [Li 96] Li, Y., Hsieh, F., Modeling of Flow in a Single Screw Extruder, *Journal of Food Engineering*, 27, pp.353-375 (1996)
- [Lin 98] Lin, P., Jaluria, Y., Conjugate Thermal Transport in the Channel of an Extruder for non-Newtonian Fluids, *International Journal of Heat and Mass Transfer*, 41: 3239-3253 (1998)
- [Luyten 91] Luyten, H. T., van Vliet, Walstra, P., Characterization of the Consistency of Gouda Cheese: Rheological Properties, *Netherlands Milk and Dairy Journal*, 45, 33-42 (1991)
- [Maddock 59] Maddock, B.H., A Visual Analysis of Flow and Mixing in Extruder, *Soc. Plast. Eng. J.*, 15, pp. 383-394 (1959)
- [McKelvey 59] McKelvey, J. M., *Polymer processing*, pp. 228-247, John Wiley & Sons, NYC (1959)
- [Montgomery 91] Montgomery, D.C., *Design and Analysis of Experiments*, 3rd ed., John Wiley and Sons, New York (1991)
- [Nebrensky 73] Nebrensky, J., Pittman, J. F. T., Smith, J. M., Flow and Heat Transfer In Screw Extruders: A Variational Analysis Applied in Helical Coordinate, *Poly. Eng. & Science*, 13, No. 3, pp.209-215, (1973)
- [O'Brian 92] K. O'Brian, *Computer Modeling for Extrusion and Other Continuous Polymer Processes*, Carl Hanser Verlag, Munich (1992)
- [Patankar 72] Patankar, S. V., Spalding, D. B., A Calculation Procedure for Heat, Mass, and Momentum Transfer in Three-Dimensional Parabolic Flows, *Int. J. Heat Mass Transfer*, 5, pp.1787-1791 (1972)
- [Pearson 85] Pearson, J., R., A., *Mechanics of Polymer Processing*, London: Elsevier Applied Science, London, (1985)
- [Rautenbach 82] Rautenbach, R., Peiffer, H., Throughput and Torque Characteristics of Grooved Feed Sections in Single Screw Extruders, *Kunststoffe Germany, Plast.*, 72, pp.262-266 (1982)
- [Rauwendaal 86] Rauwendaal, C. *Polymer Extrusion*, New York: Hanser Publishers, pp. 311-364 (1986)
- [Rauwendaal 98] Rauwendaal, C, Osswald, T. A., Tellez, G., Gramann, P. J., Flow Analysis in Screw Extruders-Effect of Kinematic Conditions, *Int. Poly. Pro. XIII*, Hanser Publishers, Munich (1998)

- [Ravetz 07] Ravetz, J.R., "No-Nonsense Guide to Science", New Internationalist Publications Ltd., (2007)
- [Rechenberg 73] Rechenberg, I., *Evolutionsstrategie: Optimierung Technischer Systeme nach Prinzipien der Biologischen Evolution*, Frommann-Holzboog, Stuttgart (1973)
- [Sbarski 97] Sbarski, I., Kosior, E., Bhattacharya, S.N., Temperature Rise in the Extrusion of Highly Viscous Composite Material, *Int. Polym. Process*, 12, pp. 341-345, (1997)
- [Street 61] Street, L.F., *Plastifying Extrusion*, International Plastics Engineering, vol.1, pp. 289-296 (1961)
- [Sastrohartono 95] Sastrohartono, T., Jaluria, Y., Esseghir, M., Sernas, V., A Numerical and Experimental Study of Three-Dimensional Transport in the Channel of an Extruder for Polymeric Materials, *Int. Heat Mass Transfer* 38: pp. 1957-1973 (1995)
- [Sokolinkoff 64] Sokolinkoff, I. S., *Tensor analysis: Theory and Applications to Geometry and Mechanics of Continua*, Wiley, New York (1964)
- [Spears 93] Spears, W.M., De-Jong, K.A., Bäck, T., Fogel, D.B., Garis, H., An Overview of Evolutionary Computation, *European Conf. On Machine Learning*, pp. 442-459 (1993)
- [Squires 58] Squires, P. H., Screw extruder pumping efficiency, *SPE Journal*, 14, 24, pp. 24-30 (1958)
- [Tadmor 67] Tadmor, Z., Duvdevani, H., Klein, I., Melting in Plasticating Extruders-Theory and Experiment, *Polymer Eng. & Sci.*, pp.198-217, (1967)
- [Tadmor 70] Tadmor, Z., Klein, I., *Engineering principles of Plasticating Extrusion*, Van Nostrand Reinhold, New York (1970)
- [Tadmor 72] Tadmor, Z., Broyer, E., Solids Conveying in Screw Extruders-Part II: Non Isothermal Model, *Polym. Eng. Sci.*, 12, pp. 378-386 (1972)
- [Umesh 83] Umesh G., Suk-fai L., Brent B. W., Bernhard W., Heat Capacity and Other Thermodynamic Properties of Linear Macromolecules. VIII. Polyesters and Polyamides, *Journal of Physical and Chemical Reference Data*, 12(1), pp. 65-89 (1983)
- [Upreti 03] Upreti, S. R. A New Robust Technique for Optimal Control of

Chemical Engineering Processes, Computer and Chemical Engineering, 28(8), pp.1325-1336, (2004)

- [Versteeg 07] Versteeg, H. K., Malalasekera, W., An Introduction to Computational Fluid Dynamics: The Finite Volume Method, 2nd edition, Pearson Education Limited, pp179-180, (2007)
- [Viriyayuth 84] Viriyayuthakorn, H., Kassahun, B., A Three Dimensional Model for Plasticating Extrusion Screw Design, SPE-ANTEC Tech. Papers, pp. 81-84 (1985)
- [Wang 04] Wang, J. W., Andrews, J. R. G., Numerical Simulation of Flow in Helical Ducts, AIChE Journal, 41, pp.1071-1080 (2004)
- [Whelan 81] Whelan, A., Craft, J. Letitia, Development in Injection Molding, pp. 59-62, Springer, (1981)
- [Wrede 72] Wrede, R. C., Introduction to vector and tensor analysis, Dover, New York, pp. 121-136 (1972)
- [Yamamuro 98] Yamamuro, J. A., Penumadu D., Campbell, G. A., Modeling Solids Conveying in Polymer Extruders, Int. Polym. Process., 13, pp.26-30 (1994)
- [Yu 97a] Yu, Q., Hu, G. H., Development of a Helical Coordinate System and its Application to Analysis of Polymer Flow in Screw Extruders, Part I: The Balance Equations in a Helical Coordinate System, Journal of Non-Newtonian Fluid Mechanics, 69, pp.155-167 (1997)
- [Yu 97b] Yu, Q., Hu, G. H., Development of a Helical Coordinate System and Its Application to Analysis of Polymer Flow in Screw Extruders, Part II: A Helical Channel Model for Single Screw Extruder, Journal of Polymer Engineering and Science, 38(5), pp.819-830 (1997)
- [Zamodits 64] Zamodits, H. J., Ph.D. thesis, Chemical Engineering, University of Cambridge (1964)
- [Zamodits 69] Zamodits, H. J., Pearson, J. R. A., Flow of Polymer Melts in Extruders: Part 1: The Effect of Transverse Flow and of a Superposed Steady Temperature Profile, Trans. Soc., Rheology, 13: pp.357-385, (1969)
- [Zicheng 98] Zicheng, W., Qingyou, C., Shi, W. H., A Study on Helical Coordinate System and Helical Slow Wave Structure, IEEE, 0-7803-4308-5/98, (1998)

Appendix A

The fourth and fifth-order algorithm for Runge-Kutta method with Cash-Carp development:

The fourth-order Runge-Kutta method:

$$y_{i+1} = y_i + ah$$

$$h = \text{Stepsize}$$

$$a = \frac{1}{6}(k_1 + 2k_2 + 2k_3 + k_4)$$

and:

$$k_1 = f(x_i, y_i)$$

$$k_2 = f\left(x_i + \frac{1}{2}h, y_i + \frac{1}{2}k_1h\right)$$

$$k_3 = f\left(x_i + \frac{1}{2}h, y_i + \frac{1}{2}k_2h\right)$$

$$k_4 = f(x_i, y_i + k_3h)$$

The fifth-order Runge-Kutta method:

$$y_{i+1} = y_i + ah$$

$$h = \text{Stepsize}$$

where:

$$a = \frac{1}{90}(7k_1 + 32k_3 + 12k_4 + 32k_5 + 7k_6)$$

and:

$$k_1 = f(x_i, y_i)$$

$$k_2 = f\left(x_i + \frac{1}{4}h, y_i + \frac{1}{4}k_1h\right)$$

$$k_3 = f\left(x_i + \frac{1}{4}h, y_i + \frac{1}{8}k_1h + \frac{1}{8}k_2h\right)$$

$$k_4 = f\left(x_i + \frac{1}{2}h, y_i - \frac{1}{2}k_2h + k_3h\right)$$

$$k_5 = f\left(x_i + \frac{3}{4}h, y_i + \frac{3}{16}k_1h + \frac{9}{16}k_4h\right)$$

$$k_6 = f\left(x_i + h, y_i - \frac{3}{7}k_1h + \frac{2}{7}k_2h + \frac{12}{7}k_3h - \frac{12}{7}k_4h + \frac{8}{7}k_5h\right)$$

The Cash-Carp Runge-Kutta method:

$$y_{i+1} = y_i + ah$$

$$h = \text{Stepsize}$$

$$a = \left(\frac{37}{378} k_1 + \frac{250}{621} k_3 + \frac{125}{594} k_4 + \frac{512}{1771} k_6 \right)$$

for the 4th order algorithm

where:

$$h = \text{Stepsize}$$

$$a = \left(\frac{2825}{27648} k_1 + \frac{18575}{48384} k_3 + \frac{13525}{55296} k_4 + \frac{277}{14336} k_5 + \frac{1}{4} k_6 \right)$$

for the 5th order algorithm

and:

$$k_1 = f(x_i, y_i)$$

$$k_2 = f\left(x_i + \frac{1}{5}h, y_i + \frac{1}{5}k_1h\right)$$

$$k_3 = f\left(x_i + \frac{3}{10}h, y_i + \frac{3}{40}k_1h + \frac{9}{40}k_2h\right)$$

$$k_4 = f\left(x_i + \frac{3}{5}h, y_i + \frac{3}{10}k_1h - \frac{9}{10}k_2h + \frac{6}{5}k_3h\right)$$

$$k_5 = f\left(x_i + \frac{3}{4}h, y_i - \frac{11}{54}k_1h + \frac{5}{2}k_2h - \frac{70}{27}k_3h\right)$$

$$k_6 = f\left(x_i + \frac{7}{8}h, y_i + \frac{1631}{55296}k_1h + \frac{175}{512}k_2h + \frac{575}{13824}k_3h\right. \\ \left. + \frac{44275}{110592}k_4h + \frac{253}{4096}k_5h\right)$$

Appendix B

Melting behavior and thermal properties of HDPE and PET

In recent years, a substantial amount of effort has been devoted to mathematical simulation of processes such as extrusion and injection molding. Most of these treatments have involved solving the standard transport equations with appropriate boundary and initial conditions. In most cases, much work was done with the assumption of constant transport properties, such as thermal conductivity, heat capacity and density of the plastic resins under investigation.

Thermal properties of polymers change with temperature, especially during a phase change. Some data have been reported describing the effects of temperature, molecular weight, orientation, crystallinity, and pressure on the thermal conductivity and thermal diffusivity of polymers [Kamal 89].

The thermal transport parameter changes with respect to temperature in polymers should be considered in the mathematical modeling specially when the polymer state changes from solid to liquid state. In this work all the thermal properties (i.e. thermal conductivity, heat capacity, and density) of both HDPE and PET resins are considered varying as the temperature of the resins undergoes gradual changes. In the following, the differential equations related to the thermal properties of both PET and HDPE, which are integrated with the appropriate differential equations in the mathematical model, are explained [Kamal 89], [Umesh 83]:

1. HDPE

○ Density Change of HDPE:

$$\frac{1}{\rho_{\text{HDPE}}} = 1.05 \exp(0.00136 \cdot T) \quad T \leq 135^\circ \text{C}$$

$$\frac{1}{\rho_{\text{HDPE}}} = 1.14 + 0.0009 \cdot T \quad T > 135^\circ \text{C}$$

Where T is in °C and ρ is in g/cm³

○ Heat Capacity Change of HDPE:

$$C_p = 2.25 \left[1.0 + 5.5 \exp(-a[T - 135])^2 \right]$$

where C_p is in J/g°C, T is in °C, and:

$$a=0.005 \quad \text{for } T \leq 135^\circ\text{C}$$

$$a=0.05 \quad \text{for } T > 135^\circ\text{C}$$

○ Thermal Conductivity Change of HDPE:

$$k = 0.17 \times 10^{-2} + 5 \times 10^{-2} (\rho_{\text{HDPE}} - 0.9) - 1 \times 10^{-5} T \quad T \leq 135^\circ\text{C}$$

$$k = 0.25 \times 10^{-2} + 3.254 \times 10^{-2} (\rho_{\text{HDPE}} - 0.9) - 0.58 \times 10^{-5} T \quad T > 135^\circ\text{C}$$

where k is in W/cm°C, T is in °C, and ρ is in g/cm³

2. PET

○ Density Change of PET:

$$\rho = -0.759 \times T + 1385$$

where T is in °C and ρ is in kg/m³

- Heat Capacity Change of PET:

$$C_p = 0.003 \times T^3 - 0.598 \times T^2 + 251.5 \times T - 34182$$

Where C_p is in J/kgK and T is in °C.

- Thermal Conductivity Change of PET:

$$k = 0.09 \times T + 212.2$$

Where k is in W/mK and T is in °C.